Fall 2021

Shedding Light on the Coupling Dynamics in Hybrid Nanostructures

Saba Arash

SHEDDING LIGHT ON THE COUPLING DYNAMICS IN HYBRID NANOSTRUCTURES

by

Saba Arash

Bachelor of Science
Azad University 2012

Submitted in Partial Fulfillment of the Requirements

for the Degree of Doctor of Philosophy in

Physics

College of Arts and Sciences

University of South Carolina

2021

Accepted by:

Yanwen Wu, Major Professor

Thomas M. Crawford, Committee Member

Richard J. Creswick, Committee Member

Andrew B. Greytak, Committee Member

Tracey L. Weldon, Interim Vice Provost and Dean of the Graduate School

Acknowledgments

First and foremost, I would like to give my sincere gratitude to my advisor, Dr. Yanwen Wu, for her invaluable guidance, advice, and motivation along the way. I am very thankful for her constant support and encouragement not only in my research work but also in my life.

I would also like to thank my advisement committee and other faculty members, Dr. Thomas Crawford, Dr. Richard Creswick, Dr. Andrew Greytak, Dr. Ralf Gothe, and Dr. Matthias Schindler for their time, support, and valuable suggestions. I would like to express my gratitude to the staff of the UofSC Department of Physics and Astronomy for always being kind and helpful. Thank you specifically to Sam Beals for generously offering assistance and support at any moment throughout this journey.

I am deeply grateful for the love and support from Frances Cashman, Sara FitzGerald, and Alyssa Loos. I would also like to thank Rahman Mohtasebzadeh and Bryan Chavez for their encouragement and friendship. Additionally, I would like to thank the present and former students in our group for their helpful suggestions and assistance during my research work.

Last but not least, I want to express my deepest gratitude to my family. Thank you to my mother (Ashraf), father (Habib), sister (Sadaf), and brother (Aram) for their limitless and unconditional love. I am the luckiest to have you in my life. And Paul Langmeyer, this work is only possible because of your great support and love.

Abstract

Here we present all-optical investigations of two hybrid nanostructures. In the first hybrid system, we study Janus-type nanofibers consisting of two hemi-cylinders of ferroelectric barium titanate and ferrimagnetic cobalt ferrite. Using the magnetic field-dependent polarization-resolved second harmonic generation technique, we observe a strong magnetoelectric coupling between the two ferroic constituents at room temperature. Corroborating these results by X-ray diffraction, we can also extract repeatable memory-dependent behaviors in these biphasic nanofibers. In the second hybrid system, we study the interaction between the semiconductor indium/gallium arsenide quantum dots and surface plasmon supporting silver structures in the weak coupling regime. When quantum dots are excited above the gallium arsenide band gap energy, we observe polarization- and bias-dependent transitions between different exciton charge states. We also observe a polarization-dependent effect in the photoluminescence signal when exciting below this band gap energy. Both these behaviors are absent in dots away from plasmonic structures.

Table of Contents

Acknowledgments iii

Abstract iv

List of Tables viii

List of Figures ix

Chapter 1 Introduction 1

Chapter 2 Theory and characterization of multiferroic BTO/CFO Janus nanofibers 6

2.1 Theory of multiferroic materials 6

2.2 Characterization of composite BTO/CFO nanofibers 11

2.3 Fabrication of biphasic Janus Nanofibers by electrospinning 15

2.4 Chapter summary 17

Chapter 3 Background theory of second harmonic generation . 19

3.1 Introduction to linear and nonlinear optics 19

3.2 Second harmonic generation in noncentrosymmetric materials 22

3.3 Experimental SHG setup 25

3.4 Chapter summary 32

Chapter 4 Magnetoelectric coupling in nanofiber ensembles . . 34

4.1 Power-dependent SHG measurements 34

4.2 Magnetic field modulation of polarization in Janus nanofibers 39

4.3 Discussion of polarization-resolved SHG measurements 51

4.4 Probing the magnetically-induced strain with X-ray diffraction 57

4.5 Chapter summary 61

Chapter 5 Theory and characterization of InAs/GaAs self-assembled quantum dots 65

5.1 Theory of semiconductor quantum dots 65

5.2 Characterization of MBE grown quantum dots 67

5.3 Hybrid plasmonic/QD device 71

5.4 Background theory of surface plasmon polaritons 76

5.5 Chapter summary 87

Chapter 6 Photoluminescence characterization of InAs/GaAs quantum dots 89

6.1 Photoluminescence optical setup 89

6.2 Above GaAs band gap excitation measurements 94

6.3 Below GaAs band gap excitation measurements 100

6.4 Chapter summary 105

Chapter 7 Summary and future directions 107

Bibliography 110

Appendix A Fabrication procedure using NanoFrazor 119

Appendix B Fabrication procedure using E-beam lithography . . 126

Appendix C Fabrication procedure using photolithography . . . 128

List of Tables

Table 5.1 Some of the advantages and disadvantages of the wet and dry etching. 72

List of Figures

Figure 2.1 Magnetic hysteresis loop along a) easy axis, b) hard axis. The loop along the easy axis has a narrower shape with a smaller coercive field (H_c), whereas the loop along the hard axis has a wider shape with a larger coercive field. The saturation and remnant magnetizations are indicated by M_s and M_r, respectively. 8

Figure 2.2 Schematic representation of barium titanate unit cell with a perovskite structure in the a) cubic phase above Curie temperature, and b) tetragonal phase below Curie temperature, and their corresponding responses to an external electric field. Ti^{4+} ion (black) is located at the center in the cubic phase, whereas it is shifted slightly from the center in the tetragonal phase. Ba^{2+} cations and O^{2-} anions are shown in blue and red, respectively. . 12

Figure 2.3 Schematic representation of cobalt ferrite unit cell with an inverse spinel crystal structure in the tetrahedral (p) or octahedral (q) sites. 14

Figure 2.4 Schematic showing a basic electrospinning setup used to produce Janus nanofibers consisting of a dual-channel syringe with a metal tip, a high voltage power source, and a grounded collector. The dual-channel syringe is loaded with sol-gel precursor solutions of BTO and CFO. When voltage is applied, a biphasic Taylor cone forms at the metal tip. At higher voltages, the electrospinning begins, and the charged fibers can be collected on the grounded plate. 16

Figure 2.5 An optical image of the magnetically aligned electrospun Janus nanofiber ensembles distributed on a glass substrate. 18

Figure 3.1 Schematic showing the SHG process. Two photons with the same frequency (ω) are emitted from an intense light. When an electron interacts with these two photons, it gets excited to a virtual energy level from its ground state. After a short period of time, typically on the order of femtosecond, the electron decays to its ground state and emits a new photon with twice the frequency (2ω). The original and the generated photons are shown in red and blue, respectively. Solid and dashed lines also indicate the real and virtual energy levels, respectively. 23

Figure 3.2 Top view of the experimental SHG setup with reflection geometry. H.W.P. and M1-M3 are the half-wave plate and mirrors, respectively. PMT is the photomultiplier tube detector. The Glan-Taylor (G-T) polarizer is mounted on a rotating stage to resolve the SHG signal. 28

Figure 3.3 Chart showing how to interpret the polarization-resolved SHG signal from BTO dipoles for two different excitation polarization orientations. The polarization of the incident laser is either parallel (p-in) or perpendicular (s-in) to the plane of incidence. All BTO dipoles, laser polarizations, and the SHG patterns are shown on the detection y-z plane. 30

Figure 3.4 Illustration of the BTO constituent of the Janus fiber ensemble acting as two dipoles perpendicular to each other with their projection, excitation, and detection planes. The red (blue) arrow shows the contribution to signals observed along the major (minor) axis. E1, E2, E3 are excitation planes and perpendicular to the propagation direction of the incident light. D1, D2, D3 are detection planes and perpendicular to the propagation direction of the SHG signal. The E3 and D3 planes show the projections of the dipoles onto the respective planes. 33

Figure 4.1 Plot of the SHG intensity as a function of the incident power from a BBO crystal. Red circles and solid lines represent the measured SHG signal and the best fit, respectively. 36

Figure 4.2 Plot of the SHG intensity as a function of the average power from a permalloy film. Green solid lines represent the best fit with $R^2 = 0.9946$. 36

Figure 4.3 Plot of the SHG intensity as a function of the average power on the sample from a Janus nanofiber ensemble after subtracting background noise (blue), the background noise itself (red), and pure CFO nanofibers (green). 38

Figure 4.4 Plot of the SHG intensity as a function of the average power from pure BTO nanofibers (blue) and PVA solution (red). 40

Figure 4.5 The polarization-resolved SHG signal from pure BTO nanofibers (a) at zero and, (b) in the presence of a magnetic field. 42

Figure 4.6 The polarization-resolved SHG signal from pure BTO nanofibers that are randomly aligned on the glass substrate. The circular pattern indicates perfectly random dipole orientations. 43

Figure 4.7 The polarization-resolved SHG signals from a Janus nanofiber ensemble as the magnet is moving closer to the sample. The distance between the magnet and the sample is about (a) 10 mm, (b) 8 mm, (c) 6 mm, and (d) 5 mm. 45

Figure 4.8 Magnetic field-dependent polarization-resolved SHG signals from the first Janus nanofiber ensemble: (a) at zero magnetic field (b-e) under four different magnetic field directions and (f) after removing the field. The directions of the applied magnetic field are indicated on top in purple. Dots represent the measured SHG signal at the rotated polarization, and the solid lines represent the best fit. Numbers are the maximum SHG signal intensity in arbitrary units (a.u.) and are measured by the radial distance from the origin. All blue plots have a maximum radial distance of 0.0015 (a.u.). All red plots are on the same scale with a maximum radial distance of 0.0075 (a.u.). Plots in (d) are only plotted on the red scale, which are rescaled by a factor of 5 for this ensemble. 47

Figure 4.9 Magnetic field-dependent polarization-resolved SHG signals from the second Janus nanofiber ensemble: (a) at zero magnetic field (b-e) under four different magnetic field directions and (f) after removing the field. All blue plots have a maximum radial distance of 0.0015 (a.u.). All red plots are on the same scale with a maximum radial distance of 0.015 (a.u.). Plots in (d) are only plotted on the red scale, which are rescaled by a factor of 10 for this ensemble. 49

Figure 4.10 Schematic illustration of the first Janus nanofiber ensemble: (a) at zero magnetic field (b-e) under four different magnetic field directions and (f) after removing the field (corresponding to the magnetic field orientations shown in Figures 4.8(a-f)). Green and blue arrows show the expansion and compression directions, respectively. 53

Figure 4.11 Schematic illustration of the second Janus nanofiber ensemble (corresponding to the magnetic field orientations shown in Figures 4.9(a-f)). 53

Figure 4.12 Schematic illustration of H-M hysteresis loop traces of the two Janus nanofiber ensembles 1(i) and 2(ii): (a) at zero magnetic field (b-e) under four different magnetic field directions and (f) after removing the field (corresponding to magnetic field orientations in Figures 4.8(a-f) and 4.9(a-f)). The hard and easy axis loops are shown in green and purple, respectively. . . . 56

Figure 4.13 XRD patterns recorded for a BTO/CFO Janus nanofiber ensemble at room temperature. The spectra are indexed to BTO (blue circles) and CFO (red square). We begin with no magnetic field (H=0). Then, the H(+z) and H(+x) fields are applied. The 2θ scan is varied between 15° and 50°. 58

Figure 4.14 XRD patterns recorded for a BTO/CFO Janus nanofiber ensemble. The spectra are indexed to BTO (blue circles) and CFO (red square). We begin with no magnetic field (H=0). Then, the fields are applied in the order of (+z), (-z), (+z), (+x), and (-x) directions. The zoom-in view of the CFO (111) and substrate peaks in the insets indicate that the substrate peaks do not shift. 60

Figure 4.15 Schematic illustration of H-M hysteresis loop traces for the field sequence used in the second XRD measurements. The hard and easy axis loops are shown in green and purple, respectively. . . . 63

Figure 4.16 2D XRD patterns recorded from the Janus nanofiber ensemble used in the second magnetic field-dependent XRD measurements (Figure 4.14). 64

Figure 5.1 Schematic representation of a conventional unit cell of GaAs with the cubic zinc-blende crystal structure. As and Ga atoms are shown in red and blue, respectively. Each As atom is bonded to four Ga atoms, and each Ga atom is bonded to four As atoms. 68

Figure 5.2 Structure of the QD sample grown by MBE. 70

Figure 5.3 AFM images and corresponding line scans of three etched grooves after depositing 60 nm of Ag and 5 nm of Cr. The illustrated depth profiles confirm that the capping layer is etched down to $\sim$ 110 nm with sharp sidewalls. 73

Figure 5.4 Schematic diagram of the fabrication process. 74

Figure 5.5 Post-fabrication structure of the hybrid plasmonic/QD device. The corresponding energy band diagram is shown on the right. CB, VB, and E_f stand for conduction band, valence band, and Fermi energy, respectively. 75

Figure 5.6 A simple schematic of an SPP wave propagating along a conductor–dielectric interface. The associated exponential decay of field along the x direction with maximum amplitude at $z = 0$ is shown on the right. 77

Figure 5.7 (a) Geometry for a surface wave propagation along a flat plane in the x direction. (b) Geometry for a surface wave propagation along a single interface at z = 0 that separates medium 1 with permittivity ε_1 at z < 0 region and medium 2 with ε_2 at z > 0 region. 82

Figure 5.8 An example of the dispersion curve of SPP confined at the silver/silica and silver/air interface and their corresponding light lines are shown in red and blue, respectively. Source: [93]. 88

Figure 6.1 The experimental setup with a reflection geometry used for the PL characterization of InAs/GaAs QDs. The incident laser light is first passed through a short-pass filter. Then a combination of two polarizers and a half-wave plate (H.W.P.) is used to control the intensity and polarization of the laser beam. Afterward, an NIR microscope objective (Mitutoyo infinity corrected) with magnification 50× and focal length 200 mm is used to focus the light onto the sample. The sample is mounted inside the specimen chamber of a Cryostatation and stabilized at 4 K. The generated signal is collected using the same lens, and then transmitted through a non-polarizing beamsplitter (B.S.) and a long-pass filter. The sample can also be monitored using a charge-coupled device camera (CCD) by placing a flip-mirror in the path. Afterward, the light is focused into a spectrometer to resolve the signal. 91

Figure 6.2 Effects of the incident TE and TM polarizations on silver structures and QDs. 93

Figure 6.3 Measured PL data as a function of the emission energy when dots are excited (a) away, and (b) over the silver structures. The measurements are performed for both TE and TM polarizations which are shown in blue and red, respectively. No significant difference is observed in the PL signal collected away from silver. The polarization-dependent shifts in the PL energy of some of the emission peaks in the presence of silver are shown by green arrows. 96

Figure 6.4 Bias-dependent PL maps on the silver at (a) 30 μW, and (b) 35 μW. The area indicated by yellow ovals illustrates a specific transition between two exciton species within a single QD. This transition is observed at a lower voltage for the higher power. In addition, it is occurred at a higher voltage for the TE mode compared to the TM mode, at a fixed power. 98

Figure 6.5 Two examples of the bias-dependent PL maps (a) away from silver, where the emission lines are perfectly aligned with the vertical-axis, (b) on the silver, where some of the lines are drifted. 101

Figure 6.6 880 nm PL data as a function of the emission energy when QDs are excited (a) away, and (b) on the silver structures. The measurements are performed for both TE and TM polarizations which are shown in blue and red, respectively. A polarization-dependent effect can be seen in the PL energy of the emission peaks in the presence of silver. 102

Figure 6.7 An example of the 880 nm PL data as a function of the emission energy from a different QD sample with a thicker capping layer. 104

Figure 6.8 An example of the 880 nm PL data taken on the silver. The zoom-in peak in the inset indicates a slight shift in the emission energy. This behavior is observed in several peaks. 106

Figure A.1 An example of a pattern layout designed in KLayout to write into a 3 $\times$ 4 mm QD sample using NanoFrazor. 123

Chapter 1

Introduction

Hybrid systems offer powerful platforms to design and create novel structures with unique properties. In these systems, different material classes can be combined and assembled in various ways to achieve new properties or improve the versatility and efficacy of the existing features in each component. In recent decades, special attention has been given to hybrid nanostructured systems, which exhibit distinct properties compared to their bulk counterparts. Understanding how the interplay of different nanoscale components affects their macroscopic behavior makes significant contributions to research in various rapidly evolving fields, including nanophotonics, biomedical optics, optoelectronics, and quantum optics. In this work, two hybrid nanostructured systems are characterized using two different all-optical approaches.

The first hybrid structure we are studying in this thesis is a composite multiferroic material. Unlike single phase multiferroics which are relatively rare with weak coupling at room temperature [1, 2, 3], composite multiferroics that share an interface contact area between the ferroic phases have shown a strong coupling at room temperature [4, 5]. Having a large contact area is essential to maximize the strength of coupling in composite multiferroics. Consequently, micro- and nanostructures are the best candidates because of their high interface-to-volume ratio. Specifically, theoretical and experimental studies have demonstrated that multiferroic 1-dimensional fibers exhibit magnetoelectric coupling that is orders of magnitude higher than the same volume of material in thin films and bulk [6, 7, 8, 9]. Moreover, the substrate-free synthesis process of nanofibers circumvents the clamping effect that is associated

with the substrate-dependent growth process of thin films. This effect has been observed to significantly reduce the magnetoelectric coupling [6, 10, 11]. In addition, multiferroic nanofibers can be used as building blocks to create more complex hierarchical structures, exhibiting promising potential to make novel multiferroic devices with nanometer resolution. Despite all these advantages of nanofibers, most of the modeling efforts on magnetoelectric coupling are focused on thin films [12, 13, 14, 15, 16, 17, 18] mainly because of their relatively straightforward structure and predictable behaviors. Therefore, studying 1-dimensional multiferroics can stimulate further significant contributions in experimental and theoretical ongoing research in the field of multiferroicity and magnetoelectric effects.

The particular composite multiferroics we are studying in this work are electrospun biphasic nanofibers with a Janus geometry consisting of two hemi-cylinders. Unlike other geometries such as core-shell and randomly dispersed, which suffer from lack of access to the internal constituent and localized regions, respectively, the Janus-type arrangement allows us to access both constituents simultaneously. The studied Janus nanofibers consist of ferroelectric barium titanate ($BaTiO_3$ or BTO) and ferrimagnetic cobalt ferrite ($CoFe_2O_4$ or CFO). To date, there are only limited reports on the coupling mechanism in the BTO/CFO composite Janus nanofibers [9, 19]. Thus, a systematic investigation with a reliable method is crucial to achieve the fundamental understanding of the magnetoelectric coupling effect in these composites for the extent of possible applications. We demonstrate here an experimental measurement designed to unambiguously isolate and elucidate the coupling mechanism in composite fiber structures. For this purpose, we use the second harmonic generation (SHG) technique, which offers the possibility of a non-destructive optical sample characterization. Specifically, we monitor changes in the SHG signal, which predominantly arises from the tetragonal phase of the ferroelectric BTO constituent of the Janus nanofibers [20, 21], while modifying the applied magnetic field, which only affects

the ferrimagnetic CFO constituent. Because the manipulation and the measurement methods are exclusive only to the CFO and the BTO constituents, respectively, we can definitively conclude that any modification in the SHG signal detected is attributed to the magnetoelectric coupling. This method can be generalized to any magnetoelectric coupled multiferroic system.

The second hybrid system we are studying in this thesis consists of plasmonic nanostructures, which are embedded in a dielectric substrate containing self-assembled quantum dots (QDs). The QDs we are studying in this research are indium arsenide (InAs) fully encapsulated by Gallium arsenide (GaAs). GaAs is a III-V compound semiconductor material with numerous advantages over other commonly used semiconductor materials such as silicon. Specifically, GaAs-based devices can operate at higher frequencies due to their extremely high electron mobility. Another advantage of GaAs is its direct band gap structure, so it can absorb and emit light much more efficiently than silicon with an indirect band gap. In addition, GaAs has a wider energy band gap, meaning it is less sensitive to overheating compared to silicon. All these functional properties of GaAs make it a promising material for a wide variety of applications, including manufacturing of solar cells, infrared light-emitting diodes, satellite communications, energy-harvesting devices, and optical windows [22, 23, 24, 25, 26, 27, 28, 29].

The goal of this work is to gain a better understanding of the interaction between the InAs/GaAs QDs and silver plasmonic nanostructures. Specifically, we study how the behavior of the photoluminescence (PL) of QDs can be affected in the presence and absence of plasmonic modes. To achieve this goal, we lithographically fabricate a sample to embed silver nanostructures into a dielectric substrate containing QDs. Afterward, the surface plasmon polaritons (SPPs) can be propagated at the dielectric/metal interface excited by light with energies above and below the band gap of the encapsulating GaAs. This method offers the possibility of tuning the QD emis-

sion with nearby SPP supporting structures entirely optically without altering the intrinsic optical properties of the dots. This property can be employed to open a new era in applications involving ultrafast optical switching mechanisms.

The outline of this thesis is as follows. I will describe the first hybrid system in chapters 2-4. Chapter 2 will first give a general overview of the multiferroic materials with a brief introduction to ferromagnetics, ferroelectrics, and magnetoelectric composites, which exhibit both ferroelectricity and ferromagnetism simultaneously in a single system. Continuing, I will discuss the particular structures used in this experiment, biphasic multiferroic BTO/CFO Janus nanofibers. This chapter will also explain the electrospinning process, the technique used to fabricate these fibers. In chapter 3, I will begin with a brief review of the linear and nonlinear optics and explain how the SHG process can be utilized as a powerful technique to study the properties of the noncentrosymmetric media due to its unique dependence on the material's symmetry. We note that the subject of nonlinear optics is a vast field, and therefore only the basic principles and concepts necessary to understand this work will be discussed here. Then, I will detail the experimental apparatus used to perform the magnetic field-dependent polarization-resolved SHG measurements. In chapter 4, I will provide all experiments performed on the Janus nanofibers with discussions of the observed magnetoelectric coupling in this system.

I will describe the second hybrid system in chapters 5-6 of this thesis. Specifically, chapter 5 will focus on the general theory of semiconductor QDs and the concepts of some fundamental subjects, such as the band gap energy, the conduction and valence bands, and the electron transition. Afterward, we will describe the structure of the particular QD system used in this work as well as the sample fabrication process. This process, which is used to embed the plasmonic structures into our quantum dot substrate, is the main focus of the second system of interest. Then, I will give an overview of the theoretical background of the surface waves with an emphasis on the

surface plasmon polariton (SPP) waves. Similar to SHG, this is a vast subject, and only the related topics will be studied in this chapter. These discussed subjects will be sufficient to understand the results of the optical interaction between the QDs and SPPs, presented in chapter 6. The first section of chapter 6 will provide the experimental apparatus used in this work. The second and third sections of this chapter will give the experimental results when the incident energies of photons are above and below the encapsulating GaAs band gap, respectively. Specifically, we will discuss the effects of the plasmonic structures on the measured PL signal excited from QDs as a function of the incident polarization, power, and applied bias.

Lastly, I will summarize the results of all experiments done in our hybrid structures in chapter 7 and highlight a few future directions for each system.

Chapter 2

Theory and characterization of multiferroic BTO/CFO Janus nanofibers

2.1 Theory of multiferroic materials

Multiferroics have recently attracted widespread attention as a novel class of materials due to their broad range of applications, from tunable microelectronics, transducers, and energy harvesters to biomedical wearable devices [30, 31, 32, 33, 34, 35]. Magnetoelectric multiferroics that combine ferroelectricity with ferromagnetism are the focus of this work.

2.1.1 Ferromagnetic materials

A ferromagnetic material consists of small regions with a uniform magnetization. These regions are called domains, wherein the magnetic moments are all aligned in the same direction. The domains are separated from each other by domain walls. In general, there are two types of domain walls depending on the angle of the magnetization direction between two neighboring domains: 180° walls and non-180° walls. When an external field is applied, the domains align themselves with the field in order to reduce the overall energy of the material system. If a large enough field is applied, the magnetization increases until it reaches a saturation value, known as saturation magnetization (M_s). Now, if the magnetic field is reduced to zero, the magnetization decreases from the saturation point to a remnant value (M_r). If the magnetic field is then applied in the opposite direction, the magnetization decreases to zero at H_c,

which is known as the coercive field. After that, the magnetization increases again and reaches its negative saturation value. This hysteretic behavior of ferromagnetic materials is shown in Figure 2.1.

Magnetic anisotropy can affect the shape of a hysteresis loop. Two main types of magnetic anisotropy are shape anisotropy and magnetocrystalline anisotropy. Shape anisotropy, as the name suggests, considers the effect of the macroscopic shape of a material on its magnetic properties, whereas magnetocrystalline anisotropy describes how the inherent crystal structure of a material affects its properties. The crystallographic direction along which a larger field is required to reach the saturation point is referred to as the hard axis. Conversely, the energetically favorable direction along which it is easier to reach saturation is referred to as the easy axis. These two directions can be characterized by the shape of the hysteresis loop. The loop along the easy axis is narrower with sharp transitions from the positive to the negative saturation value (Figure 2.1(a)), whereas the loop along the hard axis has a broader square shape (Figure 2.1(b)).

Rotating the saturation magnetization from one crystallographic direction to another can change the physical dimensions of the magnetic material. This phenomenon is called magnetostriction and was first discovered by James Joule in 1842. Magnetostriction constant, which is associated with the induced strain in the material, can be defined as $\lambda = \Delta L \ / \ L$, where L is the initial length of the material and ΔL is the change in length after the application of an external field. Magnetostriction can be attributed to both domain rotations and domain wall motions. In particular, only the domain rotation and non-180° wall motion mechanisms result in an increase in magnetostriction, while the movement of the 180° walls does not affect the strain in the material. The response of the magnetically induced strain, λ, to the field can be positive or negative or zero in some cases.

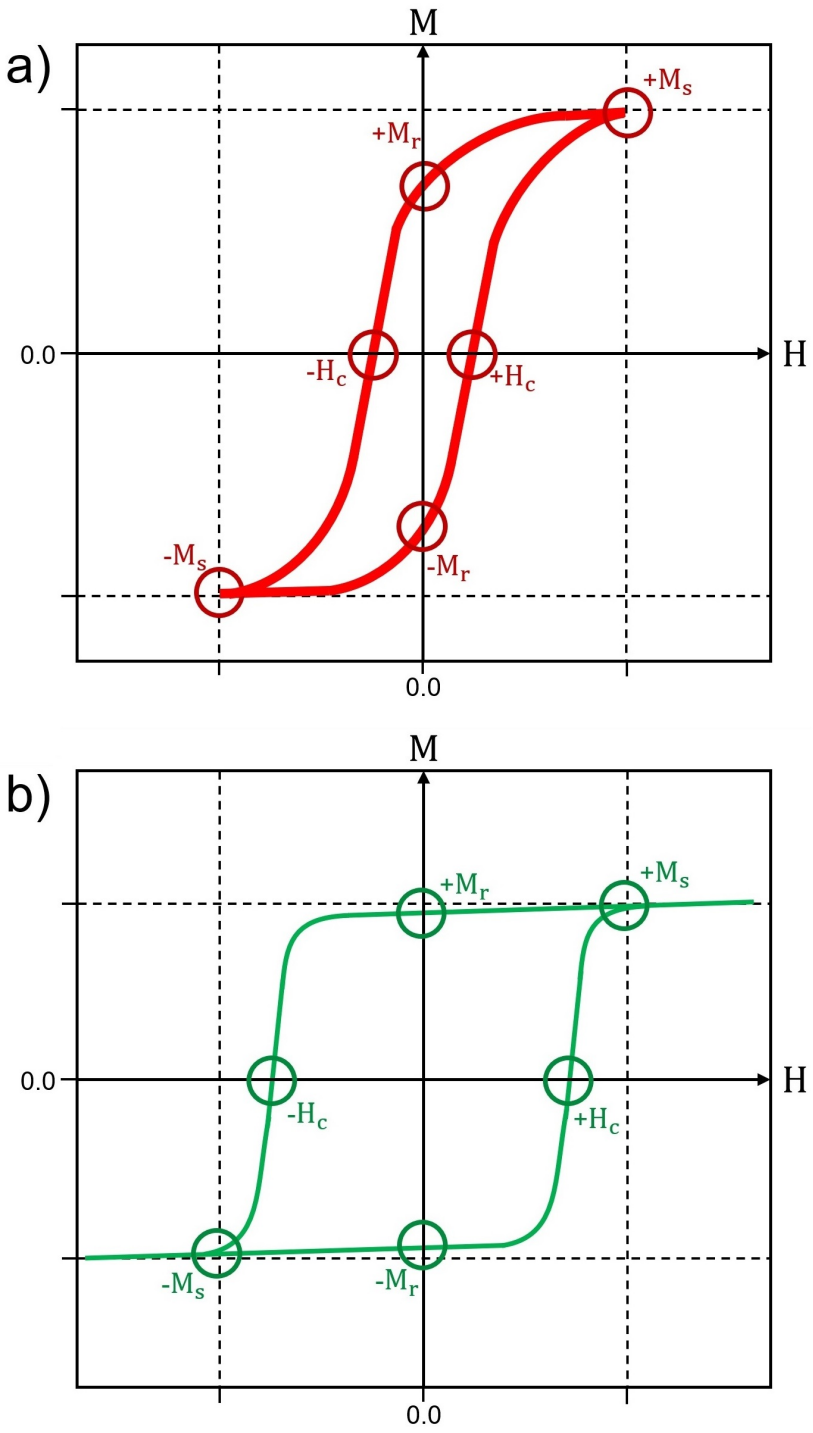

Figure 2.1 Magnetic hysteresis loop along a) easy axis, b) hard axis. The loop along the easy axis has a narrower shape with a smaller coercive field (H_c), whereas the loop along the hard axis has a wider shape with a larger coercive field. The saturation and remnant magnetizations are indicated by M_s and M_r, respectively.

By definition, a magnetic material with a positive magnetostriction constant expands in the direction of the external field, whereas a material with a negative magnetostriction contracts along the field. We note that these dimensional changes are extremely small, usually on the order of 10^{-5}, even in materials with large magnetostriction such as CFO [36].

2.1.2 Ferroelectric materials

Analogous to ferromagnetics, ferroelectric materials possess a spontaneous polarization even in the absence of an electric field. In the presence of an external field, they exhibit a similar hysteresis loop where the saturation polarization (P_s) can be reached at large fields. As the external field is removed, the polarization decreases to a remnant value (P_r). The required electric field to reduce the polarization back to zero is also called the coercive field (E_c).

The ferroelectric materials also consist of domains that are separated by 180° and non-180° domain walls. Both 180° and non-180° walls can be affected by an applied electric field, whereas a mechanical stress field affects only the non-180° walls [37]. In addition, there are different types of non-180° domain walls in ferroelectrics depending on the crystal structure of the material. For example, 90°, 90°/60°, and 71°/109° domain walls can be seen in the tetragonal, orthorhombic, and rhombohedral phases, respectively. Moreover, similar to the magnetostriction effect, the relationship between the polarization and the strain can be described by the piezoelectric effect in these materials.

2.1.3 Magnetoelectric multiferroic materials

After a brief review of the ferromagnetic and ferroelectric material characteristics, we can now discuss the magnetoelectric coupling effect, a product property that is not inherent to either of the individual ferroic orders. Being able to control the

magnetic order with an electric field and the electric order with a magnetic field in multiferroic materials unlocks the potential for a new generation of devices in magnetic sensing, energy harvesting, and low-energy memory storage [4, 38, 39]. The magnetoelectric effect has been observed in both single phase materials [40, 41] and multi phase composites [9, 42, 43]. In general, composites exhibit a stronger coupling at room temperature when compared to single phase materials. However, recent studies have reported single phase multiferroics with high magnetoelectric coupling at room temperature [44, 45]. Nevertheless, composites still offer greater engineering freedoms, e.g., choice of host materials for the different ferroic orders and the physical interface to maximize this effect. In addition, the magnetoelectric coupling is an extrinsic product property in composites, which typically results from strain mediated via the interface between the two ferroic orders. For example, if a ferromagnetic material is subjected to a magnetic field, it deforms and strains due to the magnetostriction effect. Now, suppose the ferromagnetic and ferroelectric constituents are in direct contact. In that case, the resulting strain can be transferred to the electric constituent through the interface and causes a change in the electrical polarization [46]. This effect can be described by the following equation:

$$\alpha_{DME} = \frac{\Delta P}{\Delta H} = \frac{\Delta P}{\Delta S} \times \frac{\Delta S}{\Delta H}, \tag{2.1}$$

where the magnetoelectric coefficient, α_{DME}, can be calculated by measuring the changes in the polarization (ΔP) induced by a magnetic field through the changes in the strain (ΔS). By definition, this effect is called the "direct magnetoelectric effect" and is usually measured in volts per centimeter per Oersted ($\mathrm{V\,cm^{-1}\,Oe^{-1}}$). On the other hand, α_{CME} in the "converse magnetoelectric effect" can be used to describe the changes in the magnetization (ΔM) due to the application of an external electric field (ΔE), as follows:

$$\alpha_{CME} = \frac{\Delta M}{\Delta E} = \frac{\Delta M}{\Delta S} \times \frac{\Delta S}{\Delta E}. \tag{2.2}$$

2.2 Characterization of composite BTO/CFO nanofibers

The sample used in this study is a multiferroic composite system consisting of two exclusive materials with different crystal structures: barium titanate and cobalt ferrite. Both these materials are inexpensive, nontoxic, and have robust properties at room temperature [47, 48, 49, 50, 51]

2.2.1 Barium titanate

Barium titanate ($BaTiO_3$ or BTO) is a well-known lead-free material with numerous practical applications [52, 53, 54, 55, 56, 57]. BTO has four different phases depending on the temperature. The temperature at which the phase transitions occur is known as the Curie temperature, T_c. Above $T_c = 393$ K, BTO is stabilized in a centrosymmetric cubic phase. Below this temperature, it undergoes a sequence of phase transitions: from cubic to tetragonal at $T_c = 393$ K, from tetragonal to orthorhombic at $T_c = 278$ K, and from orthorhombic to rhombohedral at $T_c = 183$ K [20].

In the unit cell of the centrosymmetric phase, Ba^{2+} cations (~ 158 pm) are located in the corners of the cube, O^{2-} anions are at the center of each face of the cube, and a small Ti^{4+} ion (~ 60 pm) is at the center of the cube [58]. When this cubic phase is polarized by an applied electric field, its polarization goes back to zero after removing the field, meaning there is no spontaneous polarization in this phase. However, in the tetragonal phase, Ti^{4+} is displaced slightly from the center, causing a small permanent dipole moment along one of the cube faces. The unit cell of BTO in the cubic and the tetragonal phases, as well as their responses to an external electric field, are shown in Figure 2.2. The room-temperature tetragonal BTO with perovskite structure (space group P4mm) is the most widely used ferroelectric ceramic material and is particularly desirable for nonlinear studies, as will be discussed in chapter 3.

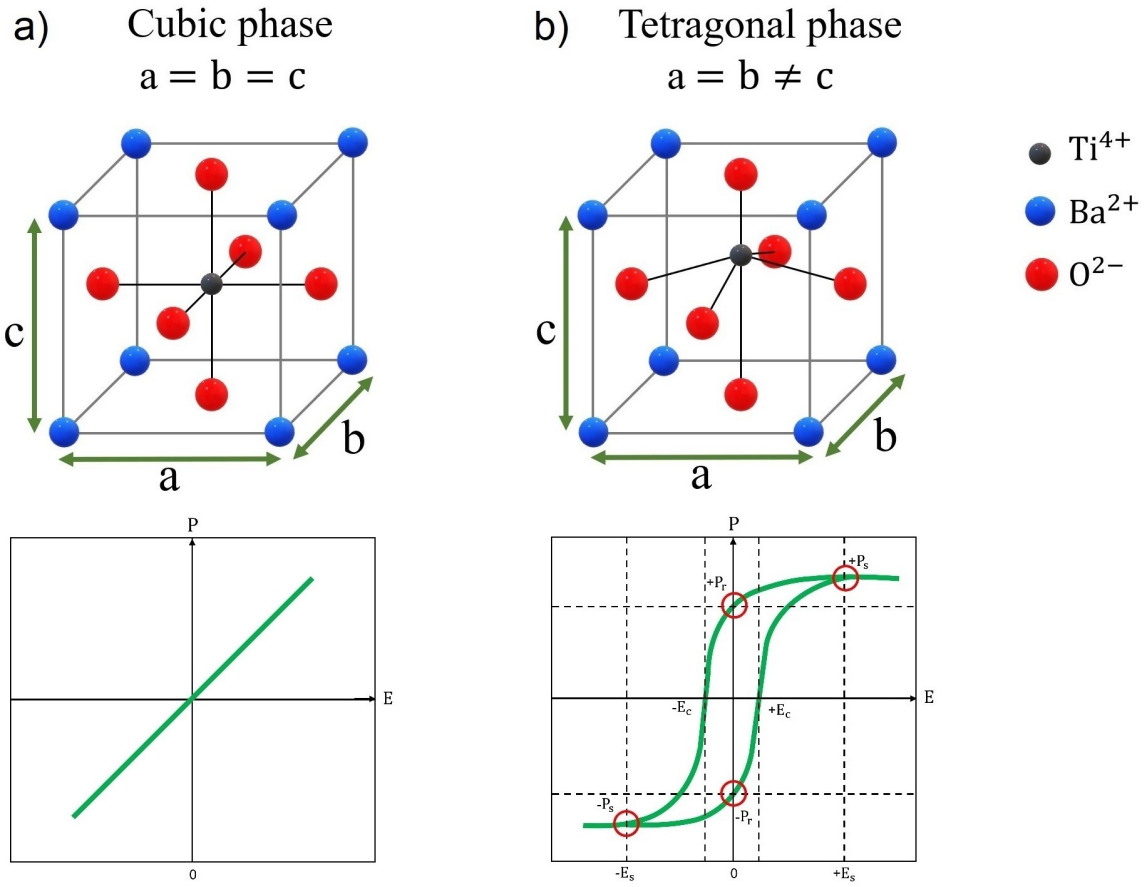

Figure 2.2 Schematic representation of barium titanate unit cell with a perovskite structure in the a) cubic phase above Curie temperature, and b) tetragonal phase below Curie temperature, and their corresponding responses to an external electric field. Ti^{4+} ion (black) is located at the center in the cubic phase, whereas it is shifted slightly from the center in the tetragonal phase. Ba^{2+} cations and O^{2-} anions are shown in blue and red, respectively.

2.2.2 Cobalt ferrite

Cobalt ferrite ($CoFe_2O_4$ or CFO) is a well-known semi-hard ferrimagnetic material with good thermal and chemical stability as well as a relatively high magnetostriction coefficient [50, 59, 60, 61]. Ferrimagnetic materials exhibit magnetic behaviors similar to ferromagnetics, including their response to an applied magnetic field which can also be described by a hysteresis loop. The main difference between the ferromagnetic and ferrimagnetic materials is in their magnetic domains. In a ferromagnetic material, all magnetic moments within each domain point in the same direction. On the other hand, some magnetic moments point in the same direction and some in the opposite direction in a ferrimagnetic material. However, these magnetic moments are unequal in magnitude, and therefore the opposing moments do not cancel each other. As a result, there is still a spontaneous magnetization in ferrimagnetic materials. CFO is also a prototypical magnetostrictive material with two coefficients: one small and positive along the hard axis, and one large (an order of magnitude larger) and negative along the easy axis [62, 63].

The polycrystalline CFO belongs to the inverse spinel family with a cubic structure (space group Fd3m). A spinel structure consists of oxygen anions and cations that are distributed on two coordinated sites: tetrahedral (p-site) or octahedral (q-site). Depending on the distribution of the metal cations on the p- and q-sites, the spinel structure is called normal or inverse. For CFO, one half of the Fe^{3+} cations sit on the tetrahedral sites (p-site), and the other half shares the octahedral sites (q-site) with Co^{2+} cations. The CFO inverse spinel structure is shown in Figure 2.3.

2.2.3 BTO/CFO Janus nanofibers

This work focuses on multiferroic BTO/CFO nanofibers. This hybrid system is known to exhibit the highest magnetoelectric effect without using rare-earth ions [51], and is therefore particularly desirable for practical applications. Our nanofibers contain

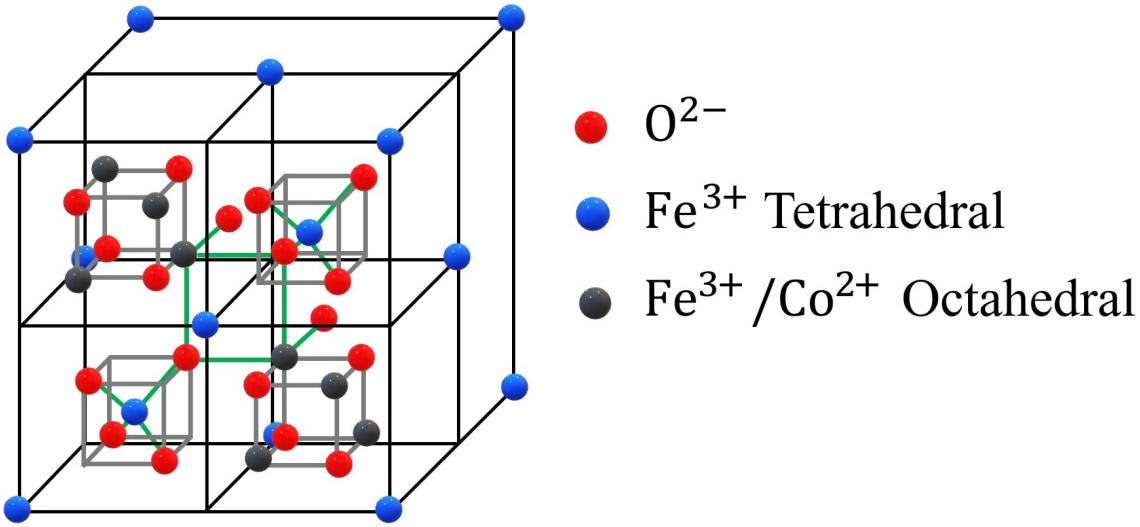

Figure 2.3 Schematic representation of cobalt ferrite unit cell with an inverse spinel crystal structure in the tetrahedral (p) or octahedral (q) sites.

two hemi-cylinders attached to each other longitudinally in a Janus configuration. These two-faced nanofibers have various lengths with an average diameter of < 1 μm. In the next section, I will talk about the synthesis process used to produce these biphasic nanofibers.

2.3 Fabrication of biphasic Janus Nanofibers by electrospinning

The nanofibers studied in this work are produced using the electrospinning method at the University of Florida [64, 65, 66]. Electrospinning has been extensively used to create composite multiferroic micro- and nanofibers [67, 68]. This inexpensive technique can be utilized to synthesize biphasic fibers with different geometries such as Janus, core-shell, or randomly dispersed. These geometries with different interfacial areas exhibit different magnetoelectric properties.

The most basic electrospinning setup consists of a syringe with a metal tip, a pump, a high voltage power supply, and a collector. When the solution is prepared and loaded into the syringe, it can be dispensed using a pump. As the solution emerges from the syringe tip, a high voltage is applied to create an electric field between the metal tip and the collector. This high voltage makes the droplet distort into a conically shaped structure, known as the Taylor cone. Once the Taylor cone is formed and the electrostatic repulsion overcomes the surface tension of the solution, the droplet begins to stretch and form a charged liquid jet. When a higher voltage is applied, the charged fibers accelerate toward the grounded collector. As the solution is collected, the solvent evaporates, leaving a mat of fibers. The final size and geometry of the fibers can be affected by several factors, including the viscosity and flow rate of the solution, applied voltage, the conductivity of the solution, temperature, and humidity [68].

To make our biphasic Janus nanofibers, a similar apparatus is used but with the application of a dual-channel syringe, as shown in Figure 2.4. These nanofibers

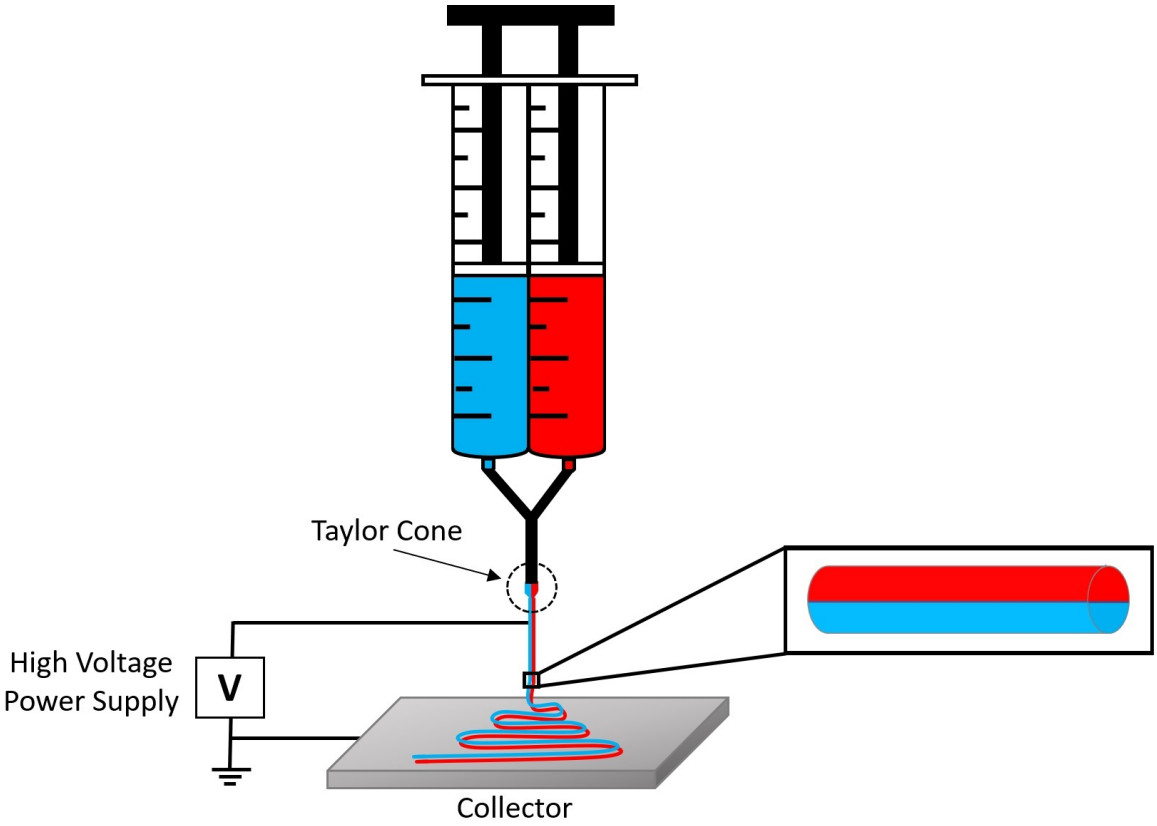

Figure 2.4 Schematic showing a basic electrospinning setup used to produce Janus nanofibers consisting of a dual-channel syringe with a metal tip, a high voltage power source, and a grounded collector. The dual-channel syringe is loaded with sol-gel precursor solutions of BTO and CFO. When voltage is applied, a biphasic Taylor cone forms at the metal tip. At higher voltages, the electrospinning begins, and the charged fibers can be collected on the grounded plate.

consist of two hemi-cylinders of BTO (62 wt %) and CFO (38 wt %) attached to each other. The electrospun Janus nanofibers are mounted onto a glass substrate using transparent polyvinyl alcohol (PVA) or water. To do this, a glass wafer (VWR VistaVision^{TM} Cover Glasses) is first cleaned with acetone and then rinsed with methanol. Afterward, the fiber/PVA or fiber/water solution is sonicated using a tip sonicator and then spin-coated onto the clean wafer. Finally, the sample is placed on top of three bar magnets in order to magnetically align the nanofibers. Figure 2.5 shows an optical image of the ensembles of the magnetically aligned electrospun Janus nanofibers distributed on a glass substrate.

2.4 Chapter summary

The first section of this chapter provided a brief overview of ferroelectric and ferromagnetic materials, which coexist in magnetoelectric multiferroics. We also demonstrated the H-M and E-P hysteresis loops of these two ferroic orders in the presence of an external field. Then, we discussed the composite multiferroic systems, which, in general, exhibit a strong magnetoelectric response at room temperature. In the second section of this chapter, we talked about the properties and structures of materials used in this work, BTO and CFO. In our studied sample, these two constituents are coupled in a Janus nanofiber system having a shared interface. In the last section, we then demonstrated the electrospinning method, which is the fabrication process used to synthesize our biphasic nanofiber ensembles. In the next two chapters, we will discuss the background theory of the optical SHG technique, the experimental setup used for the SHG measurements as well as the results obtained from the BTO/CFO Janus nanofibers.

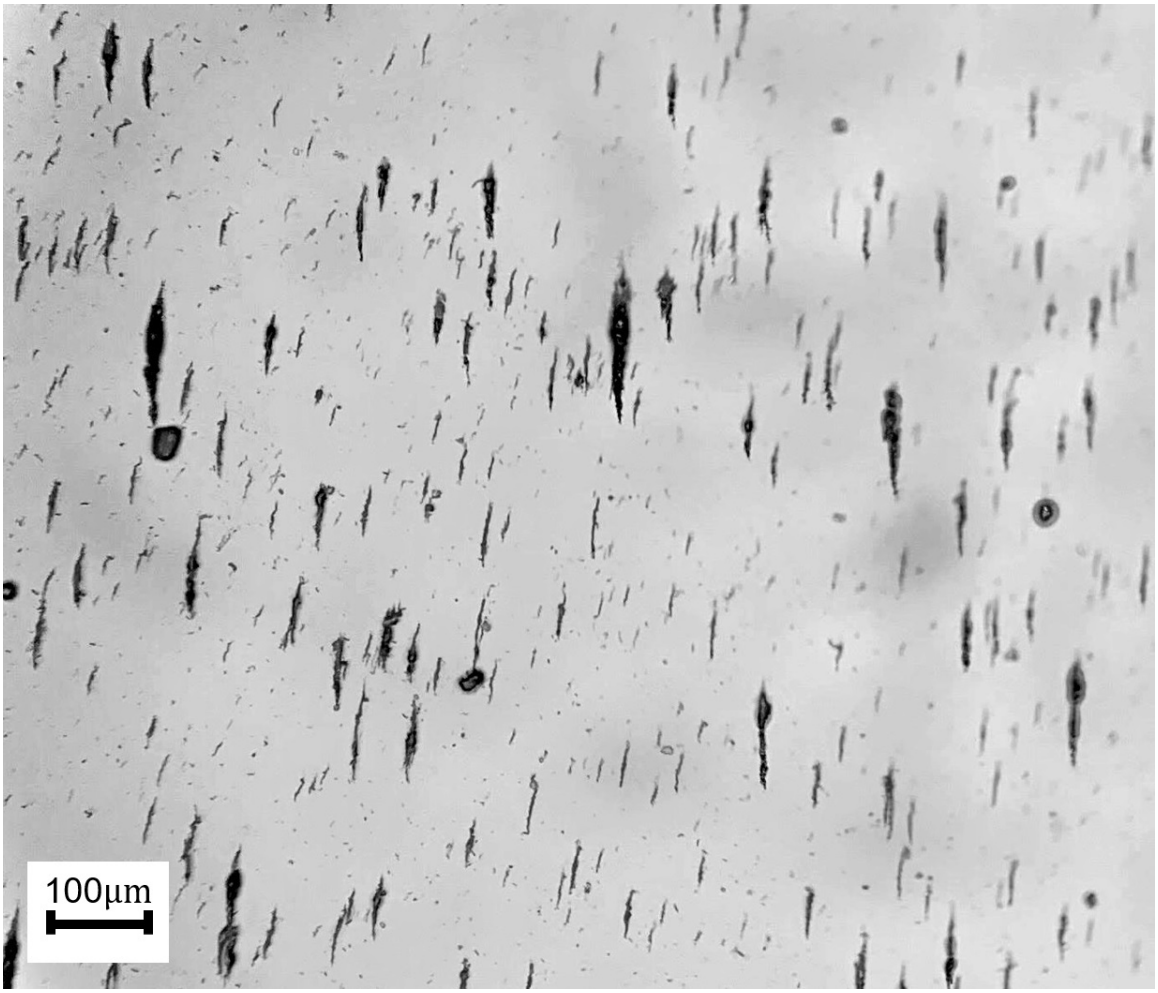

Figure 2.5 An optical image of the magnetically aligned electrospun Janus nanofiber ensembles distributed on a glass substrate.

Chapter 3

Background theory of second harmonic generation

This chapter begins with the basic concepts of linear and nonlinear optics. Then, we will provide a brief introduction to the nonlinear second harmonic generation (SHG) process, which is valid only in noncentrosymmetric materials due to parity symmetry. This coherent process is all-optical and contactless, and therefore ideal for studying nanostructures with irregular shapes and geometries. In the last section of this chapter, we will describe the optical setup and then discuss and interpret the polarization-resolved SHG signal.

3.1 Introduction to linear and nonlinear optics

To begin our journey towards understanding the nature of linear and nonlinear optical effects, we start with an overview of Maxwell's equations, which are the basis of all electromagnetic phenomena when appropriate boundary conditions are supplied.

Linear optics can be used to describe most of the optical phenomena. In a linear system, the interaction of a material with light does not modify its optical properties, meaning the superposition principle is always valid. In order to better understand this system, we first discuss the classical Lorentz oscillator model. In this model, the electron is bound to a much larger mass, the nucleus of the atom, by a hypothetical spring. When a weak field is applied to the atom, the electron slightly displaces from its equilibrium position. As a result, the spring becomes either compressed or

stretched. It is important to note that although both electron and nucleus oscillate, the nucleus contribution can be neglected because of its larger mass. In addition, the electron-spring system oscillates in a periodic form with a constant amplitude and, therefore, can be described by the simple harmonic motion theory. Moreover, the oscillation of this electron-spring system results in a dipole moment which contributes to the polarization of the system. Considering a system with N non-interacting dipoles per unit volume, the polarization is given by:

$$\mathbf{P} = -Ne\mathbf{r}, \tag{3.1}$$

where -e denotes the charge of the electron, and $\mathbf{r}$ is the displacement vector. The polarization can be used to describe the response of the material to an external field using the following macroscopic Maxwell's equations:

$$\nabla \cdot \mathbf{D} = \rho_f, \tag{3.2}$$

$$\nabla \cdot \mathbf{B} = 0, \tag{3.3}$$

$$\nabla \times \mathbf{E} + \frac{\partial \mathbf{B}}{\partial t} = 0, \tag{3.4}$$

$$\nabla \times \mathbf{H} - \frac{\partial \mathbf{D}}{\partial t} = \mathbf{J}_f. \tag{3.5}$$

ρ_f and $\mathbf{J}_f$ denote the free charge density and the current density, respectively. We note that the bound charges are neglected here for simplicity. The macroscopic electric ($\mathbf{E}$) and magnetic ($\mathbf{B}$) field quantities (also called external fields) can be determined in terms of the electric displacement ($\mathbf{D}$) and the magnetic field ($\mathbf{H}$) through the polarization ($\mathbf{P}$) and the magnetization ($\mathbf{M}$) of the material using the following constitutive relations:

$$\mathbf{D} = \epsilon_0 \mathbf{E} + \mathbf{P}, \tag{3.6}$$

$$\mathbf{H} = \frac{1}{\mu_0}\mathbf{B} - \mathbf{M}. \tag{3.7}$$

Here, $\epsilon_0 = 8.8541 \times 10^{-12}$ F/m and $\mu_0 = 4\pi \times 10^{-7}$ N/A^2 are the permittivity and permeability of free space, respectively. In addition, the linear induced polarization can be expressed by the following equation:

$$P(t) = \epsilon_0 \chi^{(1)} E(t). \tag{3.8}$$

And then, it can be generalized as:

$$P_i(t) = \epsilon_0 \sum_j \chi_{ij}^{(1)} E_j(t) \qquad \text{(i,j)=(x,y,z)} \tag{3.9}$$

As it can be seen in the above equation, P(t) is proportional to applied optical field strength E(t) with a dimensionless quantity, $\chi^{(1)}$. This coefficient of proportionality is a scalar quantity in an isotropic material and is called linear optical susceptibility.

In a nonlinear optical system, the optical response of material becomes a nonlinear function of the applied field. Therefore, the optical superposition principle is no longer valid in such a system. The behavior of the electron-spring system in the Lorentz model can also no longer be approximated as a simple harmonic oscillator, meaning it should be considered as an anharmonic oscillator. Moreover, the optical susceptibility (χ) becomes a function of the applied field (χ(E)) and can be expressed as a Taylor series:

$$\chi(E) = \chi^{(1)} + \chi^{(2)}.E + \chi^{(3)}.EE + ... \tag{3.10}$$

Consequently, the nonlinear polarization can be expanded as follows:

$$P(t) = \epsilon_0[\chi^{(1)}E(t) + \chi^{(2)}E(t)E(t) + \chi^{(3)}E(t)E(t)E(t) + ...], \tag{3.11}$$

and, can also be generalized as:

$$P_i(E) = \epsilon_0(\sum_j \chi_{ij}^{(1)} E_j + \sum_{jk} \chi_{ijk}^{(2)} E_j E_k + \sum_{jkl} \chi_{ijkl}^{(3)} E_j E_k E_l + ...). \tag{3.12}$$

Now instead of just one proportionality constant, we have a family of them: $\chi^{(1)}, \chi^{(2)}, \chi^{(3)}, etc.$. The coefficient $\chi^{(n)}$ is the nth-order optical susceptibility, a tensor

of rank n+1. Since $|\chi^{(1)}| > |\chi^{(2)}| > |\chi^{(3)}| > ...$, the higher orders with weaker effects come into play as the intensity of the light increases. Therefore, the first nonlinear process was demonstrated in 1961, shortly after the invention of the laser. When Franken et al. focused a ruby laser ($\lambda = 694$ nm) into a quartz crystal, they observed that the response of the material started deviating from the linear optics, and blue light with a half wavelength ($\lambda = 347$ nm) was generated [69]. This nonlinear phenomenon is known as the second harmonic generation and will be discussed in the next section.

3.2 Second harmonic generation in noncentrosymmetric materials

If we assume an intense monochromatic light with frequency ω is incident on a material with a nonzero $\chi^{(2)}$, the electric field associated with the light is:

$$E(t) = E_0(e^{-i\omega t} + c.c.) = 2E_0 cos(\omega t). \tag{3.13}$$

Therefore, the induced second-order polarization can be written as follows:

$$P^{(2)}(t) = 4\epsilon_0\chi^{(2)}E_0E_0^*(\frac{1 + cos(2\omega t)}{2}), \tag{3.14}$$

$$P^{(2)}(t) = 2\epsilon_0\chi^{(2)}E_0E_0^* + \epsilon_0\chi^{(2)}E_0^2(e^{-i2\omega t} + c.c.). \tag{3.15}$$

In the above equation, the first term with zero frequency describes a constant field and corresponds to the optical rectification. The second term describes a field oscillating at twice the original frequency (2ω), and therefore half the wavelength. This term corresponds to the nonlinear SHG effect and is illustrated schematically in Figure 3.1. An important effect to consider in SHG is the phase-matching process. This process defines the efficiency of the SHG power and ensures that the generated second harmonic signals interfere constructively as they are propagating through a material.

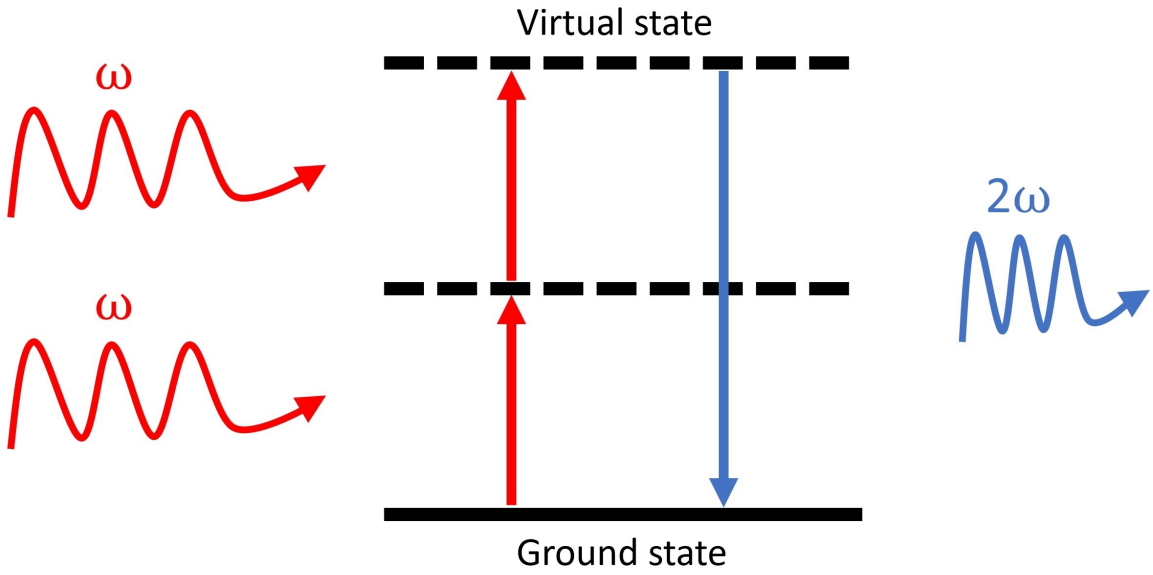

Figure 3.1 Schematic showing the SHG process. Two photons with the same frequency (ω) are emitted from an intense light. When an electron interacts with these two photons, it gets excited to a virtual energy level from its ground state. After a short period of time, typically on the order of femtosecond, the electron decays to its ground state and emits a new photon with twice the frequency (2ω). The original and the generated photons are shown in red and blue, respectively. Solid and dashed lines also indicate the real and virtual energy levels, respectively.

In order to generate a second harmonic signal, we should consider a critical factor: the inversion symmetry of the material. In crystallography, the structure of a material with inversion symmetry remains the same if we invert the position of each atom ($\mathbf{r}$) to its equivalent position ($-\mathbf{r}$) in a unit cell. In other words, a centrosymmetric material is identical to its mirror image with respect to the center of symmetry. All even ordered susceptibility coefficients in such material are zero, meaning the lowest one is the third order, $\chi^{(3)}$. Therefore, the nonlinear SHG effect is possible only in non-centrosymmetric materials with no inversion symmetry. This property can also be explained as follows. If the electric field is reversed in sign ($\mathbf{E} \rightarrow -\mathbf{E}$), the sign of the polarization will also be reversed ($\mathbf{P} \rightarrow -\mathbf{P}$). Therefore, adding a minus sign to both $\mathbf{E}$ and $\mathbf{P}$ in equation 3.11 results in $-\mathrm{P(t)} = \epsilon_0[-\chi^{(1)}\ \mathrm{E(t)} + \chi^{(2)}\ \mathrm{E(t)}\ \mathrm{E(t)} - \chi^{(3)}\ \mathrm{E(t)}\ \mathrm{E(t)}\ \mathrm{E(t)} + ...]$. Therefore, the only possible case is $\mathrm{x}^{(n)} = 0$ for all even n values since the second-order polarization is proportional to the square of the electric field. Another way to explain this property is using the potential energy of the bound electrons in the harmonic motion theory, which is fully described in [70].

Lastly, let's consider the second-order nonlinear optical susceptibility tensor. If the second-order polarization is written as follows:

$$P_i^{(2\omega)} = \sum_{j,k} \epsilon_0 \chi_{ijk}^{(2)} E_j^{\omega} E_k^{\omega}, \tag{3.16}$$

the subscripts i, j, and k can take three possible values: 1,2 or 3. Therefore, $\chi_{ijk}^{(2)}$ is a tensor of rank three with 3^3=27 components:

$$\chi^{(2)} = \begin{pmatrix} \chi_{111}^{(2)} & \chi_{112}^{(2)} & \chi_{113}^{(2)} \\ \chi_{121}^{(2)} & \chi_{122}^{(2)} & \chi_{123}^{(2)} \\ . & . & . \\ . & . & . \\ \chi_{331}^{(2)} & \chi_{332}^{(2)} & \chi_{333}^{(2)} \end{pmatrix}. \tag{3.17}$$

Using the permutation symmetry, $\chi^{(2)}_{ijk} = \chi^{(2)}_{jik}$, we can simplify the above tensor and reduce the number of components to 18 by defining a d-tensor (d_{il}) where $l = jk$ and 1 = 11, 2 = 22, 3 = 33, 4 = 23 = 32, 5 =13 = 31, 6 = 12 = 21. Therefore, this d-tensor can be written as a 3×6 matrix:

$$\begin{pmatrix} P_x \\ P_y \\ P_z \end{pmatrix} = \epsilon_0 \begin{pmatrix} d_{11} & d_{12} & d_{13} & d_{14} & d_{15} & d_{16} \\ d_{21} & d_{22} & d_{23} & d_{24} & d_{25} & d_{26} \\ d_{31} & d_{32} & d_{33} & d_{34} & d_{35} & d_{36} \end{pmatrix} \begin{pmatrix} E_x^2 \\ E_y^2 \\ E_z^2 \\ 2E_yE_z \\ 2E_xE_z \\ 2E_xE_y \end{pmatrix}. \tag{3.18}$$

For a crystalline material, the form of the d-tensor depends on the spatial symmetry of the system. Therefore, the number of non-zero components of this tensor reduces in real materials. For example, for BTO in its noncentrosymmetric tetragonal phase with point group 4mm, the d-tensor can be written as:

$$d_{il} = \begin{pmatrix} 0 & 0 & 0 & 0 & d_{15} & 0 \\ 0 & 0 & 0 & d_{24} & 0 & 0 \\ d_{31} & d_{31} & d_{33} & 0 & 0 & 0 \end{pmatrix}. \tag{3.19}$$

3.3 Experimental SHG setup

In this section, we will first describe the optical setup used to perform the SHG measurements. Then, we will discuss how to interpret the polarization-resolved SHG signal and show that the generated signal is dependent on the polarization of the incident light.

3.3.1 Optical setup

The required high intensity light is generated from a femtosecond pulsed Ti: sapphire laser oscillator (Coherent, Mira 900) with an average output power of 2.5 W, a repetition rate of 76 MHz, and a central wavelength at 820 nm. The incident light is first transmitted through a pair of half-wave plates and a linear polarizer to control the incident power and polarization. The light is then directed through a 570 nm cut-on optical filter to eliminate any SHG light produced in the laser system or by any of the optical components. Afterward, the light is modulated with an optical chopper (Thorlabs, MC2000) at a modulation frequency of 1 kHz. Next, the light is focused onto the sample using a 38.1 mm lens. This lens is mounted on an XYZ translation stage which allows us to expose different regions of the sample while maintaining the focus. The intensity of the laser light at the sample is an important factor to consider when focusing the light into our nanofibers. A very intense light can be hot enough to burn the larger ensembles, which results in a significant increase in the background noise level. Here, the spot size is on the order of a few tens of microns ($\sim$ 10-15 μm).

Following this lens is the sample that is also mounted on an adjustable XYZ stage with a resolution of 60 nm. Initially, the SHG measurements were performed in a transmission geometry where the incident laser light was passing through the sample. In this case, the x-y plane was the plane of incidence, and both the generated signal and the incident laser light were along the x-axis. However, this method resulted in a significant amount of noise in the generated signal. In order to improve the signal-to-noise ratio, we first eliminated all optical components that would increase the level of the background noise. Then, we used a different detector to collect the SHG signal. We also obtained the average results from more data points. However, we still were not able to obtain the desired signal with a lower background noise. Therefore, we decided to perform the SHG measurements in a reflection geometry where the angle between the incident and the reflected beams is 90°. The x-y plane is

still the plane of incidence, but the x- and y-axes are along the reflected and incident beams, respectively. This new geometry reduced the level of the background noise significantly.

After the sample, another lens is used to re-collimate the light and send it to a charge-coupled device camera which provides two-dimensional images of the sample. Afterward, the optical paths of the emitted SHG light and the reflected incident light are separated by an equilateral dispersive prism (Thorlabs, PS852). Following the prism, a dichroic mirror (DMSP650) is used for suppressing any residual fundamental light. The dichroic mirror used here has a 650 nm cutoff wavelength meaning it permits only the light whose wavelength is below this value and reflects the rest. For the polarization-dependent studies, a Glan-Taylor polarizer (GT10) is then placed after the dichroic mirror. This polarizer is rotated through a full 360° by a motorized rotation stage to resolve the polarization of the SHG signal. The angle of the polarizer transmission axis is measured with respect to the y-axis where 0° corresponds to the -y direction. To prevent any non-SHG signal from entering the detector, a 25 mm colored bandpass filter (FGB39) is placed before the detector, which transmits the light that is only in the 360 - 580 nm region. Finally, the SHG signal is collected by a photomultiplier tube (PMT) with a peak sensitivity at 410 nm, the expected SHG wavelength. PMT is connected to a Lock-in amplifier (Standford SR830). The signal from the PMT and Lock-in amplifier is recorded by a computer using the LabVIEW graphical programming language. A schematic of the experimental setup with reflection geometry is shown in Figure 3.2. In this setup, the polarization of the incident light is either parallel (along the x-axis, defined as p-incidence or p-in) or perpendicular (along the z-axis, defined as s-incidence or s-in) to the plane of incidence.

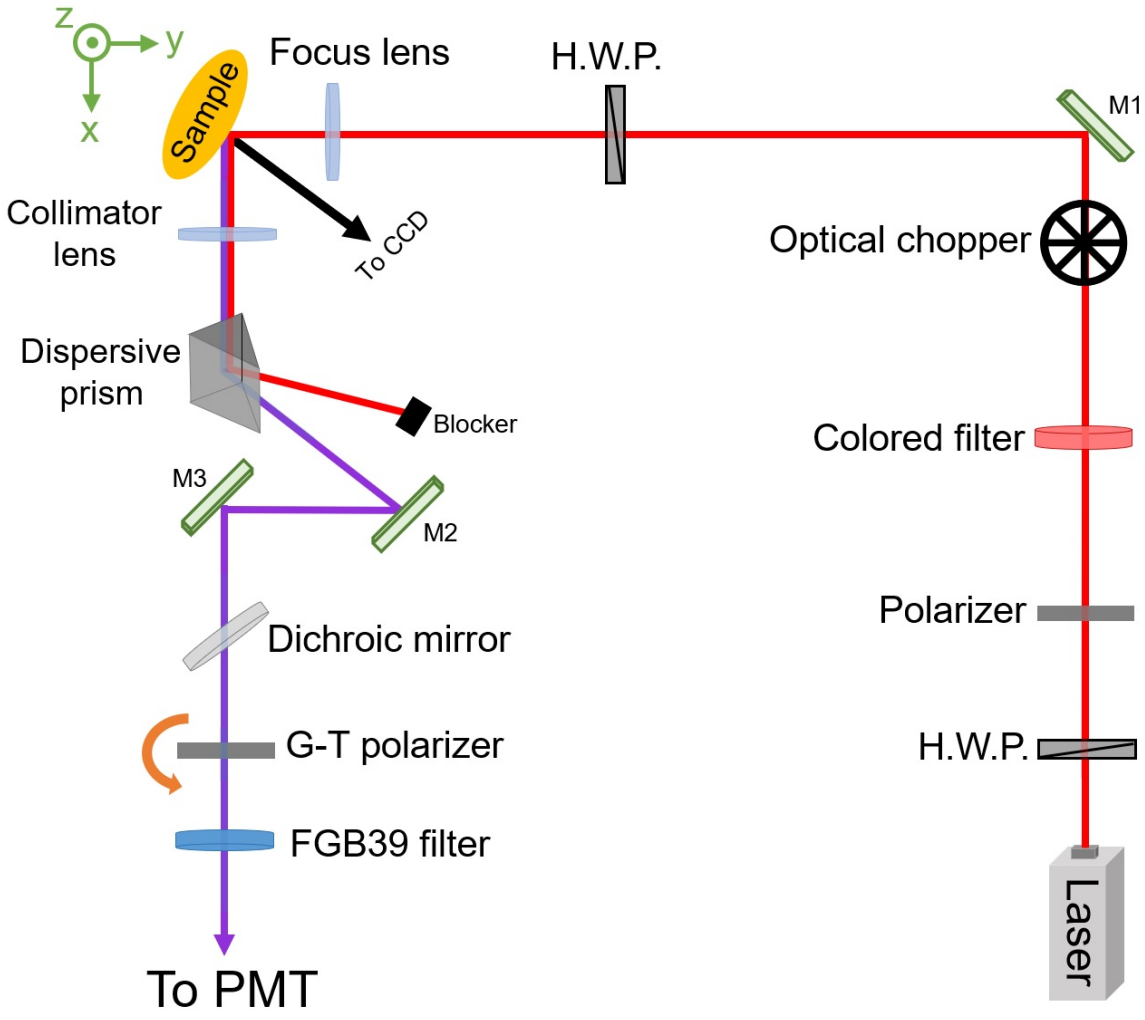

Figure 3.2 Top view of the experimental SHG setup with reflection geometry. H.W.P. and M1-M3 are the half-wave plate and mirrors, respectively. PMT is the photomultiplier tube detector. The Glan-Taylor (G-T) polarizer is mounted on a rotating stage to resolve the SHG signal.

3.3.2 Interpretation of the polarization-resolved SHG signal

In order to fully grasp the dynamics occurring inside the Janus nanofibers during the measurements in the next chapter, we need to first understand what gives rise to the pattern and intensity of the SHG signal. The SHG pattern collecting from BTO dipoles along a single direction is expected to exhibit a two-fold rotational symmetry with its major-axis along the dipoles and no signal along the minor-axis (a figure "8" pattern in two-dimensions). In fact, this pattern is a torus in three-dimensions and is often referred to as the "donut-shaped" pattern. On the other hand, when dipoles are not all aligned in the same direction, we obtain patterns with a nonzero contribution along the minor-axis. We also note that the BTO constituent of the Janus nanofibers is polycrystalline in nature, meaning the dipoles are not necessarily all aligned in the same direction in different domains.

In our setup, in order to provide the 3D information on the BTO dipoles, at least two detectors along the x- and z-axes are needed. However, this is not possible given how our sample is prepared and mounted. Therefore, our current setup, which measures the projection of the excited BTO dipoles onto the y-z plane (the detection plane), does not convey the full 3D dipole orientations. In fact, for a signal to be detected in our setup, two conditions regarding the alignments of the dipoles in the BTO constituent must be satisfied simultaneously: 1) they cannot be completely perpendicular to the incident laser polarization, so they can be excited, and 2) they cannot be completely parallel to the propagation direction of the SHG signal (the detection path along the x-axis) because a dipole does not radiate along its axis. These two restrictions are the keys to understand the dipole alignments in the BTO constituent in SHG measurements. Figure 3.3 provides a summary of how to interpret the polarization-resolved SHG signals under different excitation polarizations.

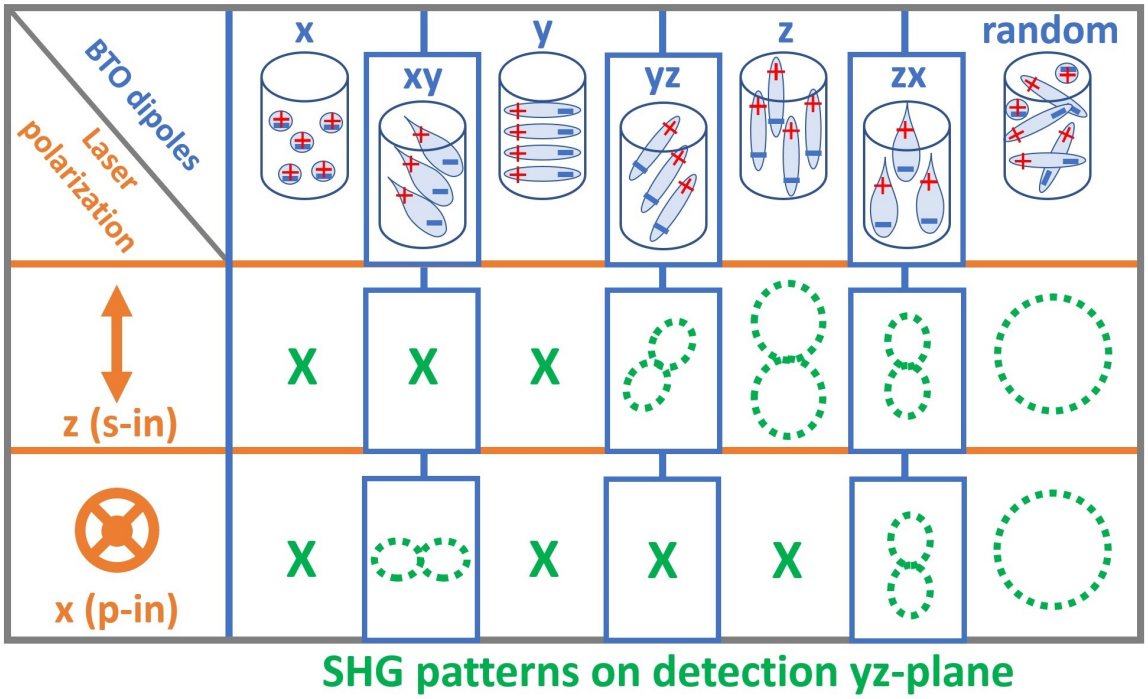

Figure 3.3 Chart showing how to interpret the polarization-resolved SHG signal from BTO dipoles for two different excitation polarization orientations. The polarization of the incident laser is either parallel (p-in) or perpendicular (s-in) to the plane of incidence. All BTO dipoles, laser polarizations, and the SHG patterns are shown on the detection y-z plane.

To better visualize the SHG patterns, we can represent the average BTO dipole alignments under the excitation area with two perpendicular components: one representing the majority dipole contribution (red arrow in Figure 3.4) and the other representing the minority dipole contribution (blue arrow in Figure 3.4). It is important to note that these two arrows only indicate the relative strength and direction of the majority and minority dipole contributions, not their absolute magnitude. In addition, if we have equal magnitude of both red and blue arrows means no preferred average polarization. Using this simple dipole model and the two detection restrictions, we can reconstruct the dipole alignments in the BTO constituent from the polarization-resolved SHG data. In order to explain this reconstruction process, we devise a general guide in Figure 3.4 using a set of SHG data as an example.

In this simple model, we consider three planes perpendicular to the propagation direction of the incident laser (E1, E2, E3) and three planes perpendicular to the propagation direction of the SHG signal to the detector (D1, D2, D3). The E3 and D3 planes are used to show the projections of the dipoles onto the respective planes. The E1 (E2) and D1 (D2) planes show the p-in (s-in) excitation field direction and its associated polarization-resolved SHG signal, respectively. We will begin with the s-in polarization. It can be seen that the signal on D2 is not a pure "figure 8" pattern which means that it contains contributions from both the majority and minority dipoles. It also signifies that the associated s-in field (shown on E2) is exciting both dipole components. This information suggests that there are non-zero projections of both dipole components on D3 and that the directions of these projections should correspond to the major and minor axes of the polarization-resolved SHG pattern in D2. Similarly, on the excitation side, the projections of the dipoles onto E3 should have non-zero component along the s-in direction (at 90°). Next, to completely pin down the orientations of these dipole contributions, we need to look at the signal, or rather the lack of it, taken under p-in excitation as presented in D1. Since the

orientations of the dipoles inside the BTO should not change merely due to a different excitation polarization, then the null signal means their alignments are either 1) both along the direction of signal propagation, or 2) both perpendicular to the p-in direction. It is immediately clear that scenario (1) is invalid because of the non-zero signal on D2. Then from scenario (2), we can conclude that the dipoles have zero projection along the p-in direction (at 0°) on E3. By combining all the information above, we then reconstruct the dipole orientations, as seen in Figure 3.4.

3.4 Chapter summary

This chapter began with a brief introduction to linear and nonlinear optics. Then, we used Maxwell's equations to determine the response of a material to an external electromagnetic field and demonstrate the relationship between the polarization and the applied electric field in both linear and nonlinear cases. Afterward, we briefly discussed the theory of the SHG phenomenon and its symmetry-dependent property. This unique property of SHG makes it a powerful tool to study materials with no inversion symmetry, such as BTO. We also provided a detailed description of the optical setup used to collect the SHG signal from our Janus nanofibers. We also discussed how to interpret the observed polarization-dependent SHG signal for different incident polarization directions. Lastly, we provided a simple dipole model which can be used as a general guide to better understand the SHG data provided in the next chapter.

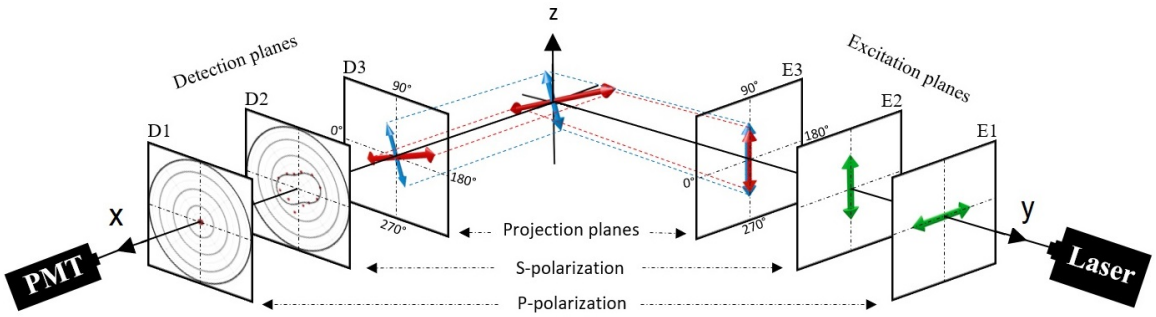

Figure 3.4 Illustration of the BTO constituent of the Janus fiber ensemble acting as two dipoles perpendicular to each other with their projection, excitation, and detection planes. The red (blue) arrow shows the contribution to signals observed along the major (minor) axis. E1, E2, E3 are excitation planes and perpendicular to the propagation direction of the incident light. D1, D2, D3 are detection planes and perpendicular to the propagation direction of the SHG signal. The E3 and D3 planes show the projections of the dipoles onto the respective planes.

Chapter 4

Magnetoelectric coupling in nanofiber ensembles

4.1 Power-dependent SHG measurements

The goal of this section is to obtain the second harmonic signal generated from a single Janus nanofiber ensemble. In addition, we will first conduct a series of control experiments to eliminate any possibility of misinterpreting this signal and also validate the observed magnetoelectric coupling effect, which will be presented and discussed in the following sections of this chapter. To achieve this goal, we will first use a nonlinear crystal and a permalloy film to verify our optical alignment. Then, we will perform the SHG power-dependent measurements on an ensemble of Janus nanofibers, pure CFO nanofibers, pure BTO nanofibers, transparent polyvinyl alcohol (PVA) solution, and a glass substrate. We will see that only the pure BTO and BTO/CFO Janus nanofibers follow the quadratic power-dependent law. Therefore, with this set of control measurements, we establish that we can successfully obtain the SHG signal from a Janus nanofiber ensemble and assert that this signal arises from the BTO constituent only.

4.1.1 SHG measurement on BBO crystal

In order to verify the alignment of the collection path in our optical setup and also maximize the overall intensity of the generated light, we first used beta-barium borate (BBO) crystal. BBO is one of the most common nonlinear optical crystals that can be

used for a wide range of wavelengths and in various techniques, including the second harmonic, third harmonic, sum frequency, and the difference frequency generation processes [71, 72]. Another important property of this double-refracting crystal is its high laser damage threshold [73]. When the phase-matching condition is achieved, the signal generated from this birefringent crystal can be strong enough to be visible to the naked eye. The generated signal from BBO as a function of the average laser power is shown in Figure 4.1. Red dots represent the measured SHG signal, and the solid lines represent the best fit. In our experimental setup (shown in Figure 3.2), the BBO crystal is placed between the red filter and the optical chopper. The light is also reflected from a glass substrate before the collimator lens. Because of the strong generated signal, the excitation power is set under 50 mW to avoid overloading our detector and therefore damaging it. The PMT voltage is set at 0.2 V using the lock-in amplifier since a higher voltage might also damage the detector.

4.1.2 SHG measurement on permalloy film

Another sample used to measure the SHG signal is a permalloy film, an alloy of nickel and iron. The magnetic properties of permalloy are studied using various techniques, such as the magneto-optic Kerr effect (MOKE) and the surface magneto-optic Kerr effect (SMOKE). MOKE is one of the most widely used measurement techniques to describe the polarization of the reflected light from a magnetic material. While permalloy has a face-centered cubic structure, the surface of this film generates SHG signal [74]. Although this light is weaker than the BBO signal and not visible to the naked eye, it is still much stronger than the signal generated from the Janus nanofibers. Therefore, it can also be used to verify our optical alignment. The power-dependent SHG plot of the permalloy film can be seen in Figure 4.2. Here, the PMT voltage is set at 0.7 V.

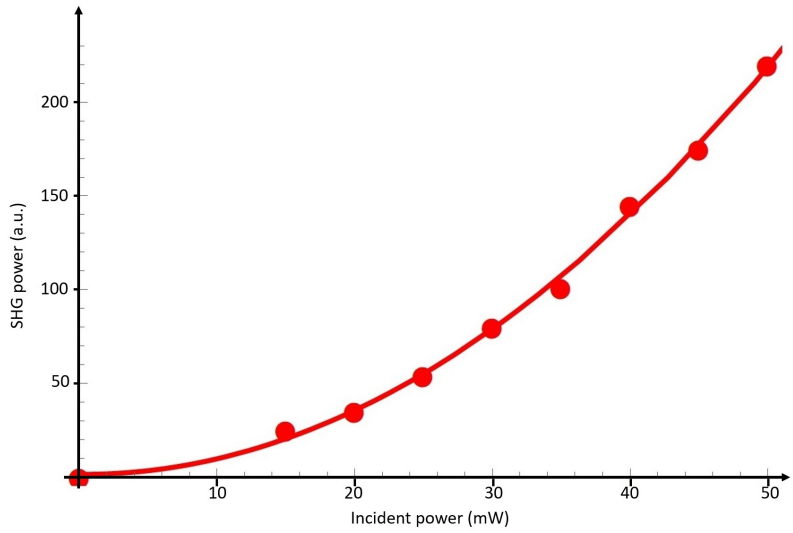

Figure 4.1 Plot of the SHG intensity as a function of the incident power from a BBO crystal. Red circles and solid lines represent the measured SHG signal and the best fit, respectively.

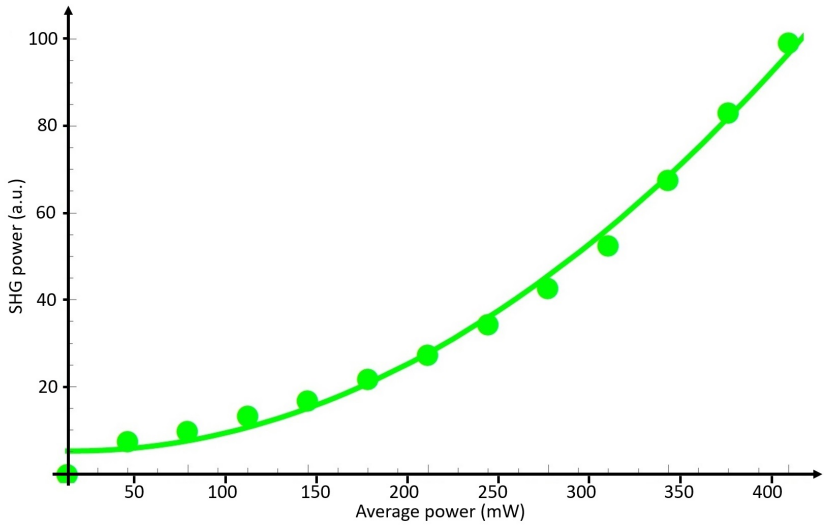

Figure 4.2 Plot of the SHG intensity as a function of the average power from a permalloy film. Green solid lines represent the best fit with $R^2 = 0.9946$.

If we consider a parabola with the equation y = ax^2 + bx + c, the quadratic regression value, R^2, can be simply calculated using $R^2 = 1 - \frac{\alpha}{\beta}$, where

$$\alpha = \sum \left(y_i - ax_i^2 - bx_i - c\right)^2, \tag{4.1}$$

$$\beta = \sum \left(y_i - \overline{y}\right)^2. \tag{4.2}$$

The mean value of the y is $\overline{y} = \frac{\sum y_i}{n}$ for n values. The above R^2 equation gives us a number between 0 and 1, where higher numbers indicate that the data points are closer to the quadratic fit. Here, the calculated quadratic regression from the permalloy film data is $R^2 = 0.9946$.

4.1.3 SHG measurement on BTO/CFO Janus nanofibers

After verifying the alignment of our optical setup, we performed the SHG measurements on a single Janus nanofiber ensemble. The generated second harmonic signal as a function of the average laser power after subtracting the background noise is shown with blue dots in Figure 4.3. Here, the average power is measured on the sample, and the PMT voltage is set at 0.8 V. The blue lines show the quadratic fit to our data with $R^2 = 0.99226$. Each data point is obtained from averaging 500 consecutive measurements in order to obtain precise results. Since our detector is an extremely sensitive light collector and the SHG signal from the nanofibers is relatively weak, we need to ensure that we have sufficiently suppressed any unwanted background signal due to the scattered light. The background data shown in Figure 4.3 (colored red) confirms that the collected SHG signal is indeed from the sample and not from any stray light in the lab or elsewhere in the apparatus. The background noise is measured by blocking the emitted light after the dispersive prism.

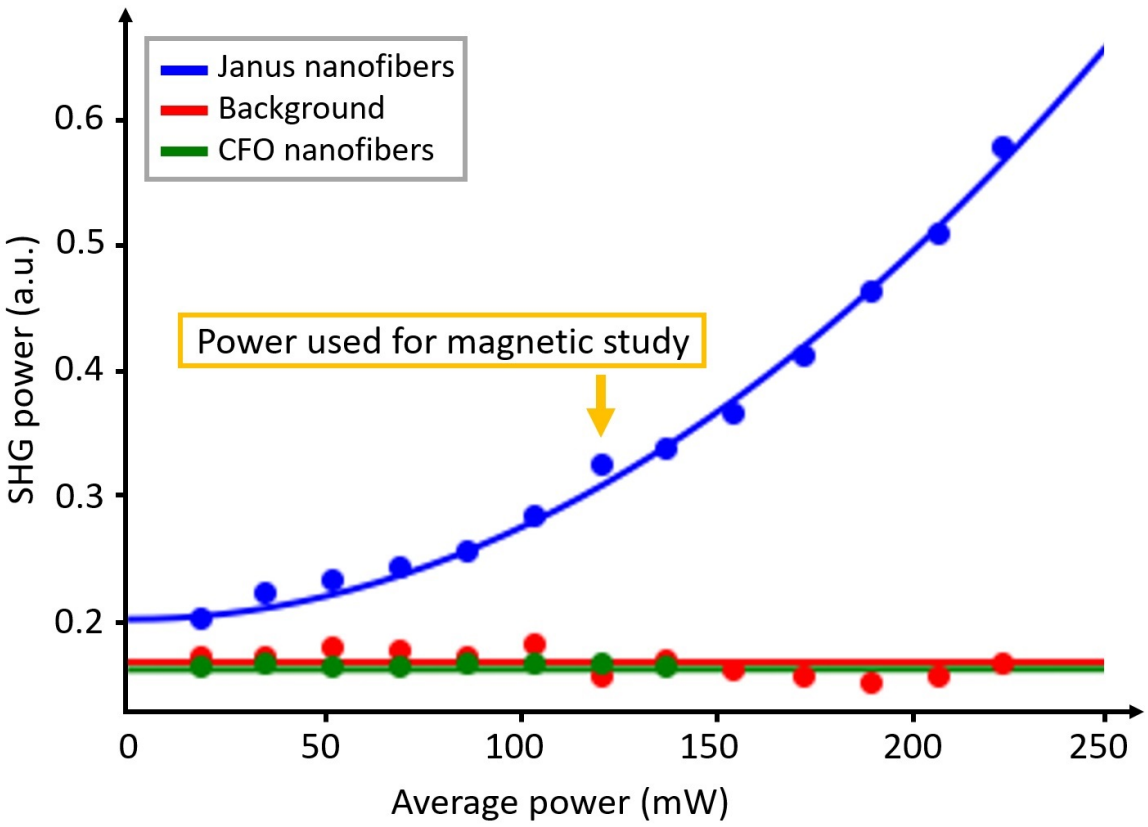

Figure 4.3 Plot of the SHG intensity as a function of the average power on the sample from a Janus nanofiber ensemble after subtracting background noise (blue), the background noise itself (red), and pure CFO nanofibers (green).

4.1.4 SHG measurement on pure CFO and pure BTO nanofibers

Now, to verify that the observed SHG response from Janus nanofibers is only from the BTO constituent, we performed the power-dependent measurements on pure CFO nanofiber ensembles of comparable sizes. The measured SHG response is shown with green color in Figure 4.3. It can be seen that there is no considerable signal from CFO, as expected. This also confirms that the observed SHG light is not from the CFO surface, which also breaks the inversion symmetry. In addition, we performed a similar power-dependent measurement on pure BTO nanofibers for comparison purposes. The results are shown in Figure 4.4, where the quadratic regression is $R^2 = 0.9997$.

As mentioned in section 2.3, the electrospun Janus nanofibers are mounted onto a glass substrate using either water or PVA. We note that SHG is an optical probe and can be used to access buried interfaces if the top medium is transparent. Therefore, to verify that the observed SHG signal is indeed from the BTO constituent of the Janus nanofibers, power dependency measurements are also taken from PVA, which is illustrated in Figure 4.4 (colored red). The PMT voltage is set at 0.75 V for all measurements in this subsection.

4.2 Magnetic field modulation of polarization in Janus nanofibers

In this section, we will apply a magnetic field to BTO and BTO/CFO nanofibers to confirm that only the CFO constituent of Janus ensembles responds to a magnetic field. Afterward, we will perform systematic magnetic field-dependent polarization-resolved SHG measurements on two different Janus ensembles. All magnetic field-dependent measurements are done using a permanent bar magnet with a field strength of ~ 1.5 kOe. As mentioned in section 3.3, the incident light is polarized either parallel (defined as p-in) or perpendicular (defined as s-in) to the plane of incidence. In addition, to change the magnetic field direction, we first move the magnet away

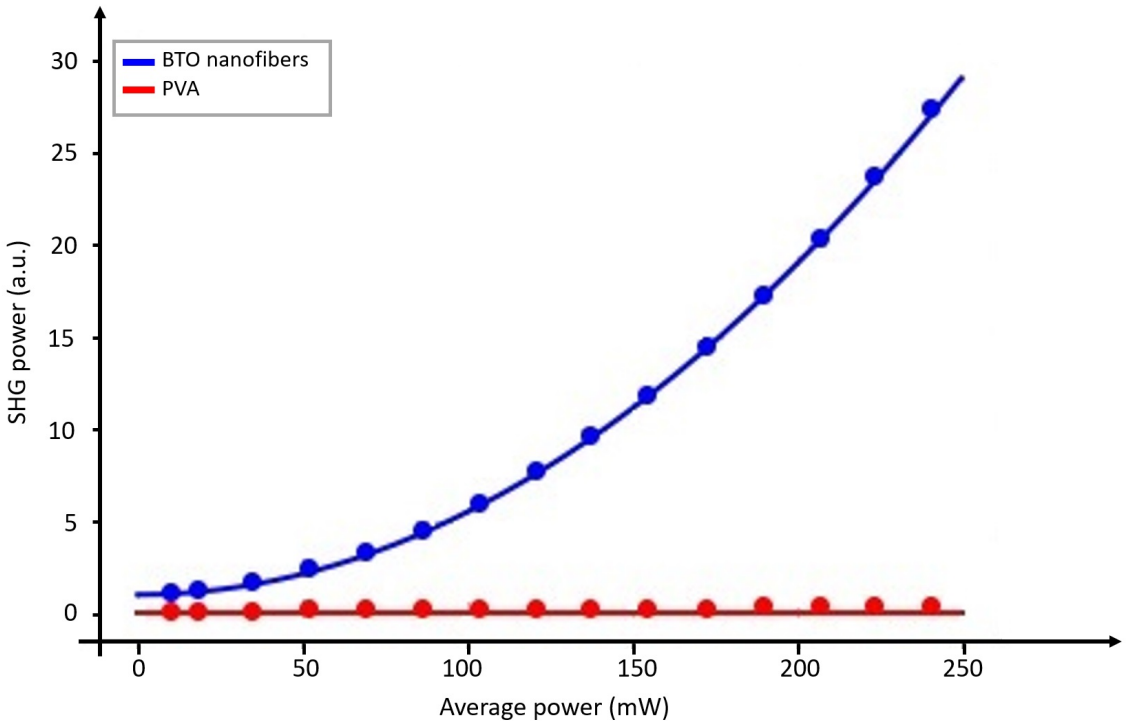

Figure 4.4 Plot of the SHG intensity as a function of the average power from pure BTO nanofibers (blue) and PVA solution (red).

from the sample while maintaining its original direction, rotate it to its new direction, and then move it back towards the sample. This mimics the process of a hysteresis loop measurement and ensures that we are keeping track of the histories of the magnetic field orientation and strength.

4.2.1 Investigation of the magnetoelectric coupling in BTO nanofibers

The magnetic field-dependent polarization-resolved SHG measurement is first performed on pure BTO nanofibers to verify that the magnetic field cannot affect this constituent of the Janus nanofibers. Figure 4.5(a) shows the polarization-resolved SHG data from BTO nanofibers at zero magnetic field. Circles and continuous lines represent measured data and the best fit, respectively. The incident polarization in this measurement is along s-in. The intensity of the signal is also represented by the radial distance from the origin. The response displays a two-fold rotational symmetry defined by the net polarization of the BTO nanofibers. When a magnetic field is applied perpendicular to the fibers in Figure 4.5(b), it can be seen that there are no changes in either polarization orientation or the magnitude of the SHG signal, confirming that BTO does not respond to the magnetic field.

Having a non-zero signal at the origin of the polar patterns indicates a spread of different dipole orientations within the laser spot size and signifies that our data does not come from a perfect linear polarization. This is in agreement with the polycrystalline nature of BTO. In addition, these fibers are randomly aligned on the substrate. In fact, we have also obtained a near circular SHG polarization pattern, which is indicative of perfectly random BTO dipole orientations, by surveying a different location on the sample. See Figure 4.6.

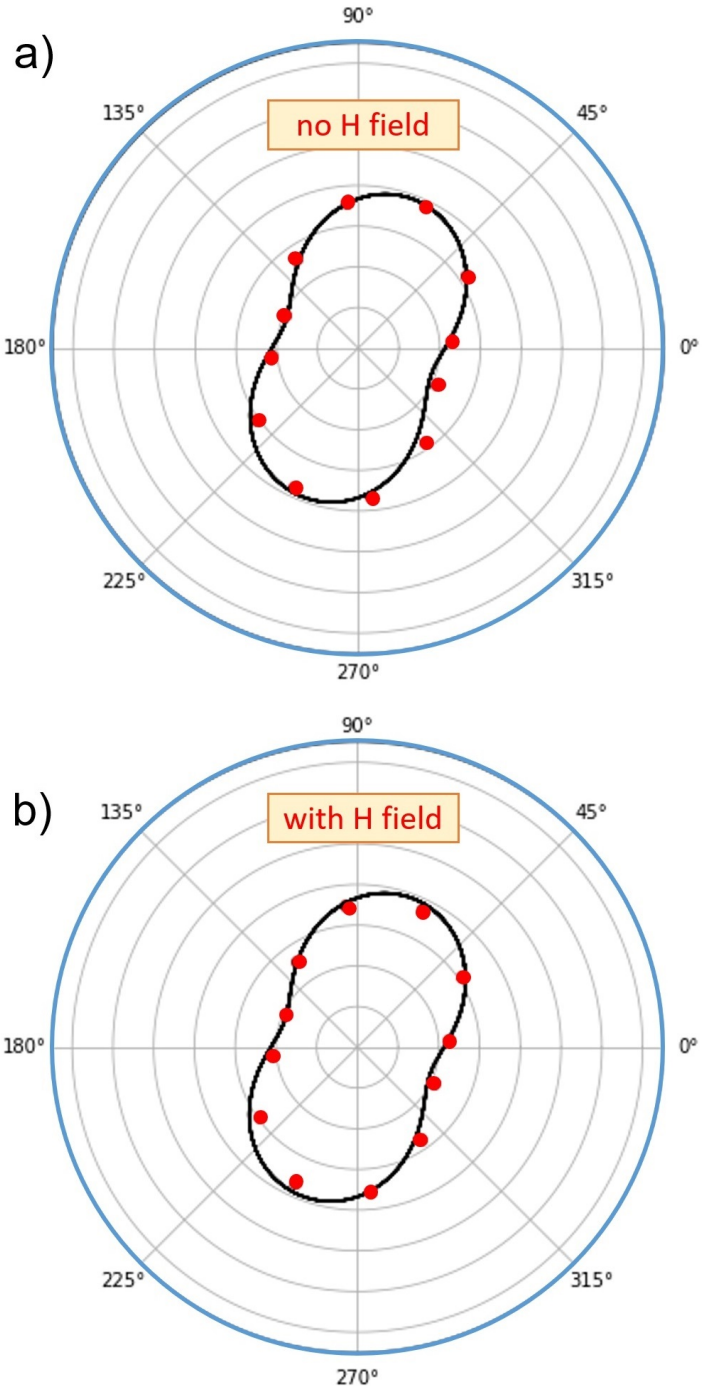

Figure 4.5 The polarization-resolved SHG signal from pure BTO nanofibers (a) at zero and, (b) in the presence of a magnetic field.

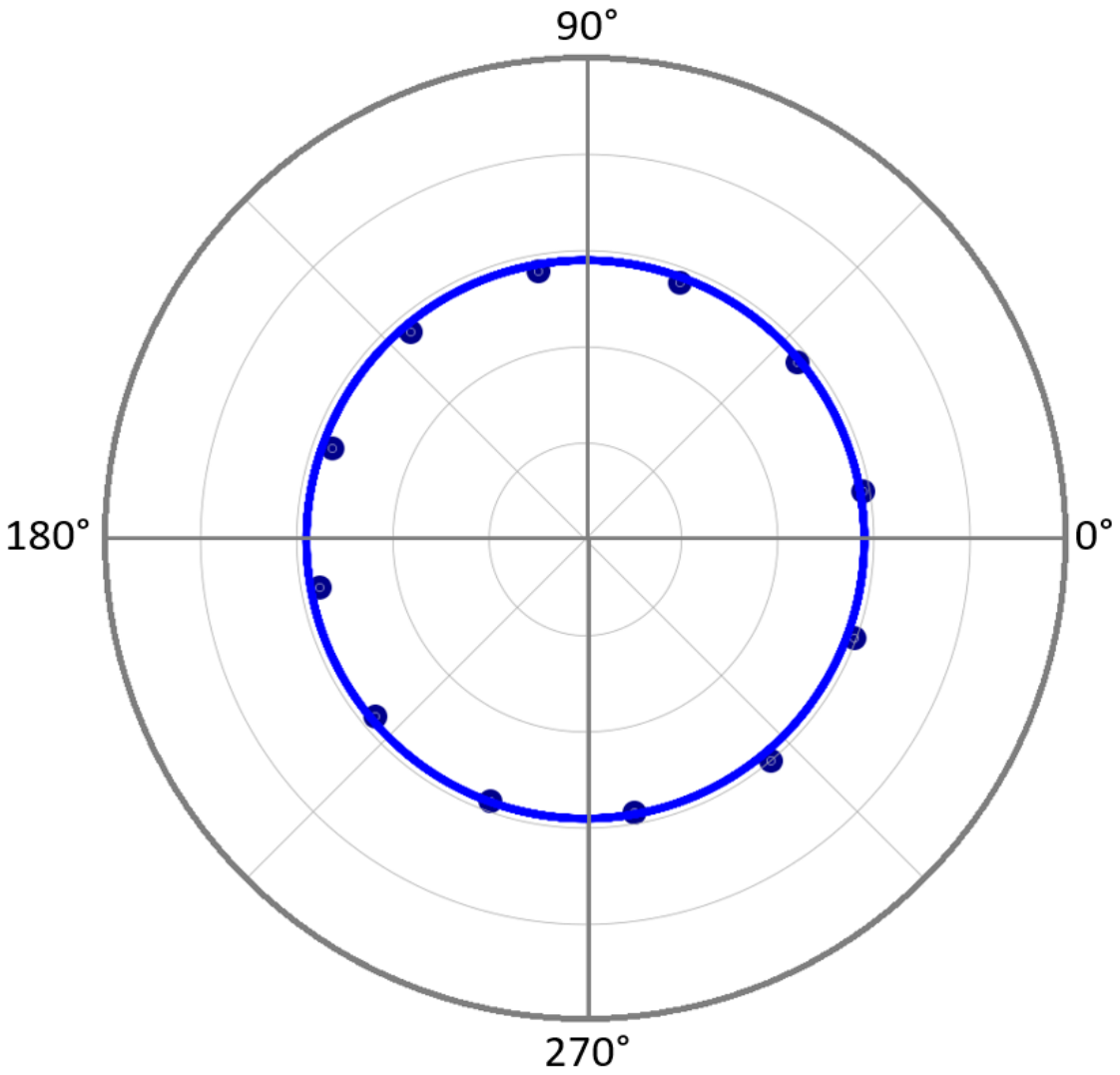

Figure 4.6 The polarization-resolved SHG signal from pure BTO nanofibers that are randomly aligned on the glass substrate. The circular pattern indicates perfectly random dipole orientations.

4.2.2 Investigation of the magnetoelectric coupling in Janus nanofibers

To study the effect of the magnetic field on the polarization-resolved SHG signal in Janus nanofibers, we first moved the magnet closer to an ensemble in four steps, as shown in Figure 4.7. The magnet initially is at a distance of 10 mm from the sample, then 8 mm, 6 mm, and finally 5 mm. In Figure 4.7(d), the intensity of the SHG signal is reduced in magnitude for the p-in excitation while maintaining the same pattern. However, both the intensity and the pattern of the signal are altered for the s-in excitation. Since the applied magnetic field is the only variable in this simple experiment, the observed changes in the SHG signal indicate the existence of the magnetoelectric coupling in these structures.

It also can be seen that there are no changes until the magnet is as close as 5 mm to the sample. This behavior is because of the field strength of our small magnet, which drops off rapidly at a distance of a few millimeters away. This is confirmed using a Gauss meter (Meggitt 5180).

After observing these changes in SHG polar plots, we performed a systematic investigation on two different Janus nanofiber ensembles, as will be presented in the following subsections.

4.2.3 Magnetic field-dependent polarization-resolved SHG measurement from ensemble 1

In this systematic investigation, the magnetic polarization-resolved SHG measurement is performed on an aligned Janus nanofiber ensemble with laser power at 125 mW (shown in Figure 4.3). This power is chosen to minimize heating from the laser while maintaining a sufficient SHG signal. The nanofiber ensemble alignment direction is perpendicular to the x-y plane, i.e., along the z-axis, which is also parallel to the CFO easy axis [75]. We apply two sequential pairs of fields on this ensemble where the fields within each pair are antiparallel, and the pairs are perpendicular

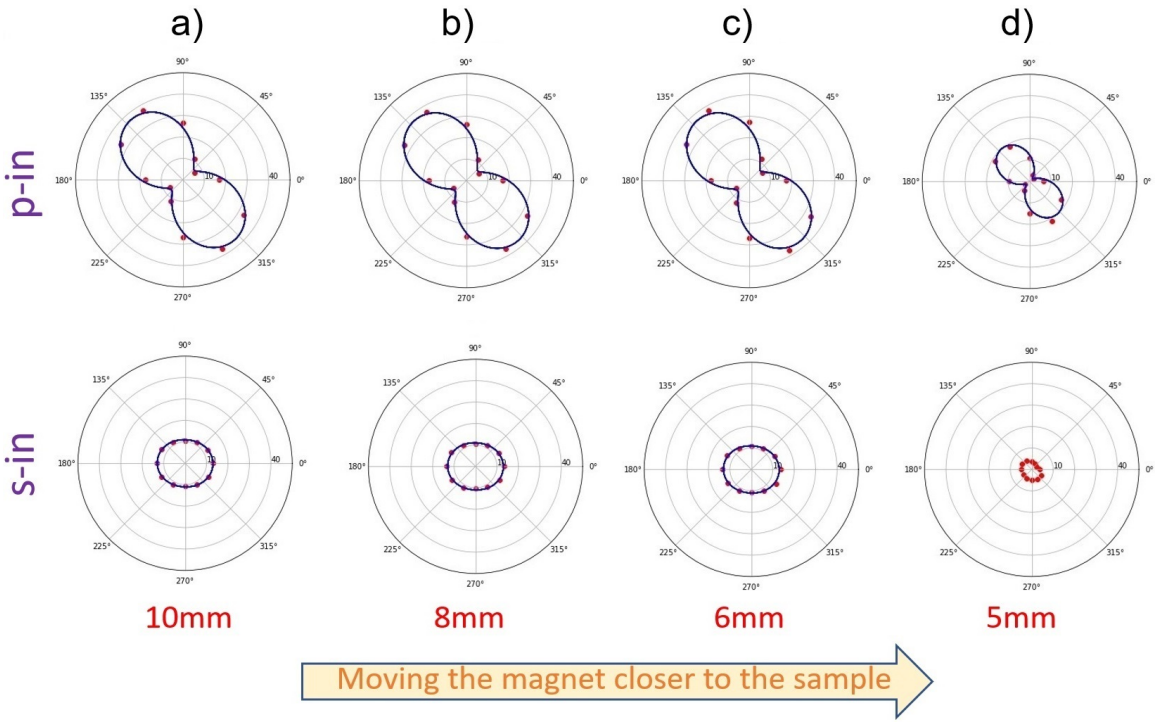

Figure 4.7 The polarization-resolved SHG signals from a Janus nanofiber ensemble as the magnet is moving closer to the sample. The distance between the magnet and the sample is about (a) 10 mm, (b) 8 mm, (c) 6 mm, and (d) 5 mm.

(dashed boxes in Figure 4.8). The antiparallel field pairs and 90° rotation between pairs are designed to study how parallel and perpendicular magnetization changes in the CFO along and between the easy and hard axes affect the strain transfer in this nanofiber system, respectively.

We begin our measurement with no magnetic field in Figure 4.8(a). When there is no field, a two-fold pattern is obtained for the s-in excitation with its major-axis along $\theta = 160°$ and a nonzero signal along its minor-axis at $\theta = 70°$. The angle of the major-axis, θ, is measured counterclockwise from the horizontal axis, $\theta = 0°$. No sizable signal is observed for the p-in excitation. The results at zero field represent the initial dipole projections on the detection (y-z) plane. Afterward, a magnetic field along the +x direction is applied to the sample. One can see clearly that after applying this field, the SHG pattern for s-in is reduced in magnitude and has a new major-axis along $\theta = 80°$. We note that there is no signal along the minor-axis, which seems to signify that we are measuring signals from unidirectional dipoles. The signal from p-in excitation is still negligible. Then, when we apply the magnetic field in the -x direction (H(-x) in Figure 4.8(c)), the signal magnitude becomes almost 4 times larger and maintains its orientation under s-in excitation. A nonzero signal also appeared under p-in excitation with its major-axis along $\theta = 87°$. We rotate the magnetic field again by 90° from H(-x) towards H(-z). This rotation produces drastic changes in the SHG signal strength for both s-in and p-in excitations, as indicated by the data in the red boxes in Figure 4.8(d). The SHG signal is increased by more than 3 times for s-in and about 7 times for p-in excitation. The plots indicated in the red boxes in Figure 4.8(d) are rescaled by a factor of 5 to accommodate the large signal. We have also replotted all other SHG plots on the same scale as Figure 4.8(d) in red to facilitate better visualization of the relative signal strengths.

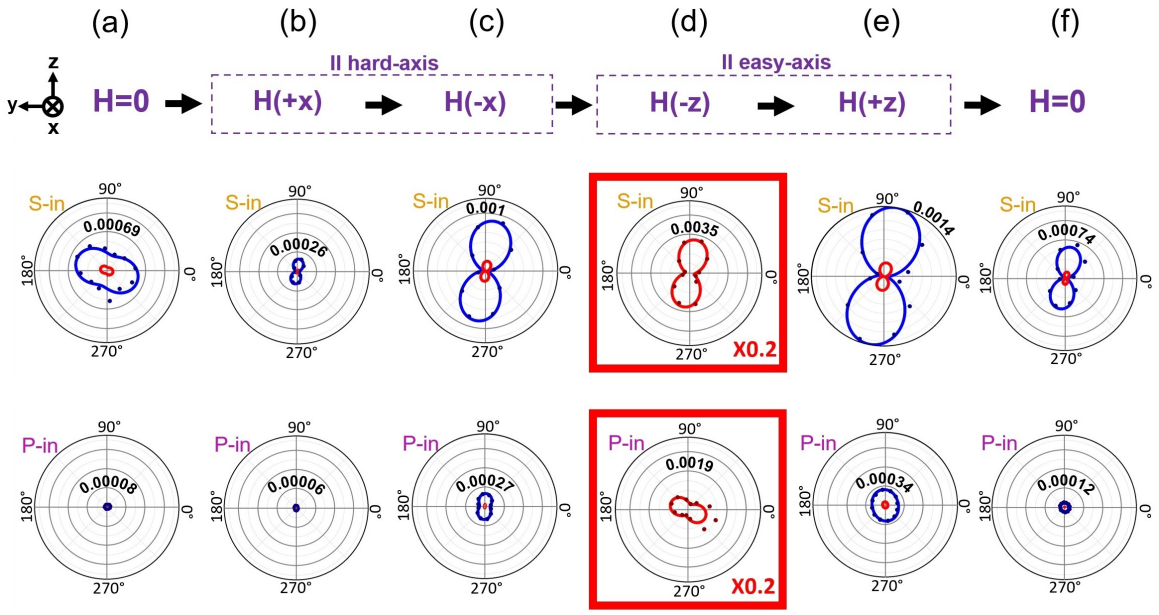

Figure 4.8 Magnetic field-dependent polarization-resolved SHG signals from the first Janus nanofiber ensemble: (a) at zero magnetic field (b-e) under four different magnetic field directions and (f) after removing the field. The directions of the applied magnetic field are indicated on top in purple. Dots represent the measured SHG signal at the rotated polarization, and the solid lines represent the best fit. Numbers are the maximum SHG signal intensity in arbitrary units (a.u.) and are measured by the radial distance from the origin. All blue plots have a maximum radial distance of 0.0015 (a.u.). All red plots are on the same scale with a maximum radial distance of 0.0075 (a.u.). Plots in (d) are only plotted on the red scale, which are rescaled by a factor of 5 for this ensemble.

The last magnetic field orientation is rotated 180° along +z direction (H(+z) in Figure 4.8(e)). In this case, the SHG signals under both s-in and p-in excitations seem to recover a similar pattern produced under magnetic field orientation H(-x) (before the drastic change). In the final step, when the magnetic field is removed, the SHG polarization patterns under both excitation directions shown in Figure 4.8(f) exhibit merely a reduction in strength in comparison to the patterns under magnetic field H(+z). This behavior signifies the memory of these multiferroic Janus nanofibers.

4.2.4 Magnetic field-dependent polarization-resolved SHG measurement from ensemble 2

We repeated the entire magnetic-dependent experiment using a different Janus nanofiber ensemble and applied the magnetic field in different sequences by reversing the order of the field directions. In other words, the order of the antiparallel x and z field pairs is swapped in this ensemble with respect to the first one, as can be seen in dashed boxes in Figure 4.9.

In Figure 4.9(a), when there is no magnetic field, two-fold patterns are observed for both s-in and p-in excitations having major-axis along $\theta = 30°$ and $\theta = 130°$, respectively. Observing nonzero polar patterns in the initial state is likely because this ensemble is being exposed to different magnetic field directions before performing this experiment. Then, H(+z) is applied to the fiber ensemble that rotates both major-axes toward +z direction (Figure 4.9(b)). The major-axis is along $\theta = 53°$ for s-in excitation and $\theta = 112°$ for p-in excitation. In addition, both the SHG signals are increased in magnitude. Afterward, when the field is rotated by 180° in Figure 4.9(c), the SHG signal under s-in excitation is reduced in magnitude, having a new major-axis along $\theta = 81°$ with no signal along the minor-axis. No sizable signal is observed for the p-in excitation. Then when H(-x) is applied, no clear two-fold patterns are observed for s-in and p-in excitations with a drastic change in the signal strengths.

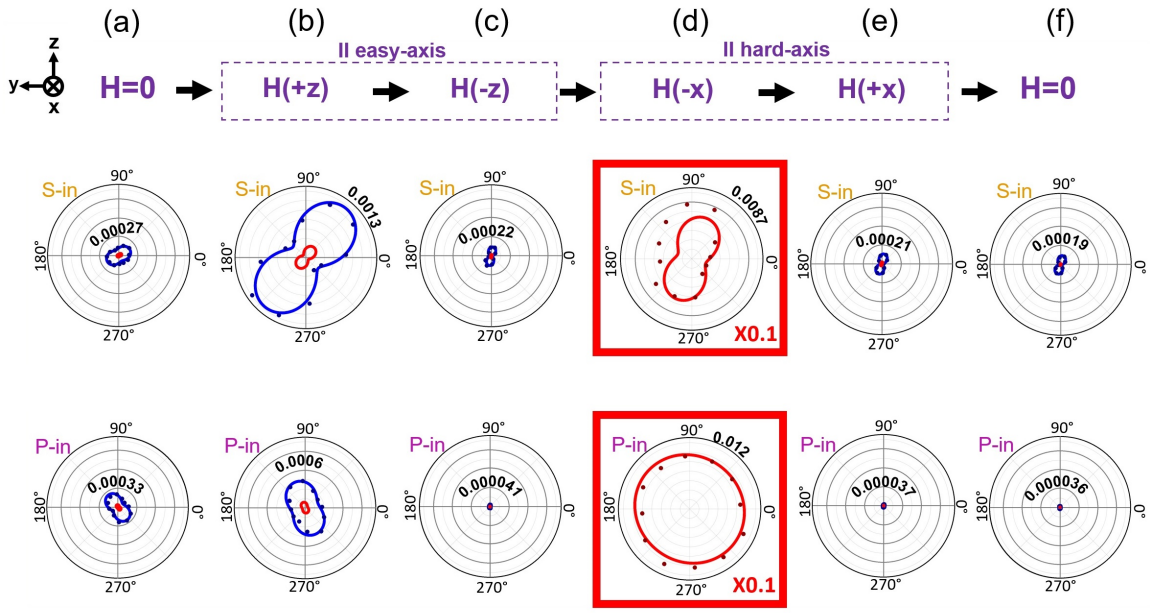

Figure 4.9 Magnetic field-dependent polarization-resolved SHG signals from the second Janus nanofiber ensemble: (a) at zero magnetic field (b-e) under four different magnetic field directions and (f) after removing the field. All blue plots have a maximum radial distance of 0.0015 (a.u.). All red plots are on the same scale with a maximum radial distance of 0.015 (a.u.). Plots in (d) are only plotted on the red scale, which are rescaled by a factor of 10 for this ensemble.

We note that this change in the SHG intensity is observed after rotating the magnetic field by 90° (similar to Figure 4.8(d)). Here, the polar plots in Figure 4.9(d) are rescaled by a factor of 10 in order to compare to the other signals. Finally, the magnetic field is rotated by 180° one more time in Figure 4.9(e). Again, both SHG patterns become mostly similar to Figure 4.9(c). The major axis is along $\theta = 76°$ for s-in excitation having a two-fold pattern and p-in excitation signal is negligible. In the final step, when the field is removed, no changes are observed in the SHG polarization patterns in Figure 4.9(f) in comparison to Figure 4.9(e).

In both ensemble measurements, each data point of the polarization-resolved SHG signal is obtained from averaging 300 consecutive measurements. In addition, each data point takes 90 seconds, and each SHG plot has 12 data points. Moreover, in order to ensure that each set of measurements begins with the sample at room temperature, there is a 5-minute cool-down time after each set to change the magnetic field direction and the incident polarization. As a result, the total measurement time for each ensemble is about 4.5 hours.

Now let's consider both ensembles in Figures 4.8 and 4.9. Although the initial conditions of these two ensembles, including the residual strain and the initial dipole projections, are different from each other, we observe distinct similarities in the relative changes of the nanofiber behaviors after applying magnetic fields. The first notable change in the SHG signal is when we apply the first field, H(+x), on the first ensemble and H(+z) on ensemble 2. Specifically, in ensemble 1, the intensity and pattern of the SHG signal for s-in are significantly altered by the field, whereas that for p-in remains unchanged (Figure 4.8(b)). In ensemble 2, the intensity of the signal for both s-in and p-in is changed significantly while maintaining the same pattern (Figure 4.9(b)). A second trend shared by both ensembles is the similarity in the SHG signal after field reversals. For ensemble 1, the dipole projections in Figure 4.8(e) show a similar signal to that seen in Figure 4.8(c) (both pattern and intensity) and

Figure 4.8(a) (only intensity). The same trend is observed in ensemble 2, as shown in Figures 4.9(e), 4.9(c) and 4.9(a). A third trend is that the largest change in the SHG signal occurs during the 90° field rotation, from -x (hard axis) to -z (easy axis) for ensemble 1 and the reverse for ensemble 2. In both cases, as shown in Figures 4.8(d) and 4.9(d), the SHG signals grow tremendously in intensity for both excitations as well as exhibit a tendency to deviate from the two-fold symmetry pattern, which is especially evident in ensemble 2. This behavior implies a mixture of dipole polarization direction has arisen in the system upon 90° field rotation. In contrast to the third trend, the last trend notes the negligible change in the SHG signal upon field removal. In both ensembles, the pattern of the SHG signal for both excitations remains the same with a slight reduction in intensity as compared to that prior to field removal (Figures 4.8(f) and 4.9(f)).

4.3 Discussion of polarization-resolved SHG measurements

4.3.1 A "toy model" to describe the overall shape change of Janus fibers

To understand the magnetic field-dependent evolution of the SHG signals, we first take into account the cylindrical geometry of the Janus nanofiber system. As mentioned earlier, the predominant magnetoelectric coupling mechanism in the BTO/CFO composites is strain transfer across a shared interface between the ferroic phases. Therefore, the unique geometry of the nanofibers, which can be represented by a long cylinder not pinned to a substrate, allows strain transfer to occur through the overall shape change. This is unlike in thin films, where the strain transfer is mainly mediated through the interface. In addition, recall that there are two magnetostriction coefficients in CFO: a small positive along the hard axis and a larger negative one along the easy axis. Thus, for example, an applied magnetic field along the easy axis of fiber should cause simultaneous axial compression and radial expansion. In fact, this behavior has been observed in CFO grains 10-100 μm in size [76].

Considering the overall geometry of the fibers, we present a "toy model" in which a longitudinal (axial) compressive or tensile stress causes deformation in the transverse (radial) directions with an opposite sign to maintain a constant volume [36, 77]. We also note that the conducted MOKE (magneto-optical Kerr effect) data show that the hysteresis loop of our Janus nanofibers is asymmetric, meaning the magnetization traces out a minor loop when reversing the field [75]. This is unlike the "standard hysteresis", where fully reversing the field direction causes domain reversal with no change in the magnetization magnitude and hence strain. In this toy model, we consider a simple case where the magnetic field reversal causes an overall reduction in the strain of the system. However, when we investigate the hysteretic behaviors of these fibers more carefully in the following subsection, we will see that the field reversal causes either a reduction or an increase in the system strain.

Let's first consider ensemble 1 (SHG data of this ensemble is shown in Figure 4.8). Figure 4.10(a) shows a schematic illustration of a single nanofiber with little strain prior to applying a magnetic field. In the first field pair (H(+x) and H(-x)), applying H(+x) along the hard axis causes an expansion in CFO along x and compression along y with negligible change along the easy axis. Transferring this magnetically induced strain through the shared interface deforms the BTO constituent of the fiber, as shown in Figure 4.10(b). As a result, we can say that the dipole projection along y disappears with almost no change in the projection along z. This is in agreement with the data shown in Figure 4.8(b). Since the polarization in the BTO constituent is predominantly along x at this point, s-in leads to negligible SHG, whereas p-in leads to SHG that radiates along x and thus cannot be detected by our setup. After reversing the magnetic field, the reduced magnetization and hence strain causes the CFO constituent to relax (Figure 4.10(c)). This behavior can explain the SHG signal in Figure 4.8(c) that has a similar intensity to that seen in Figure 4.8(a) but is oriented along z.

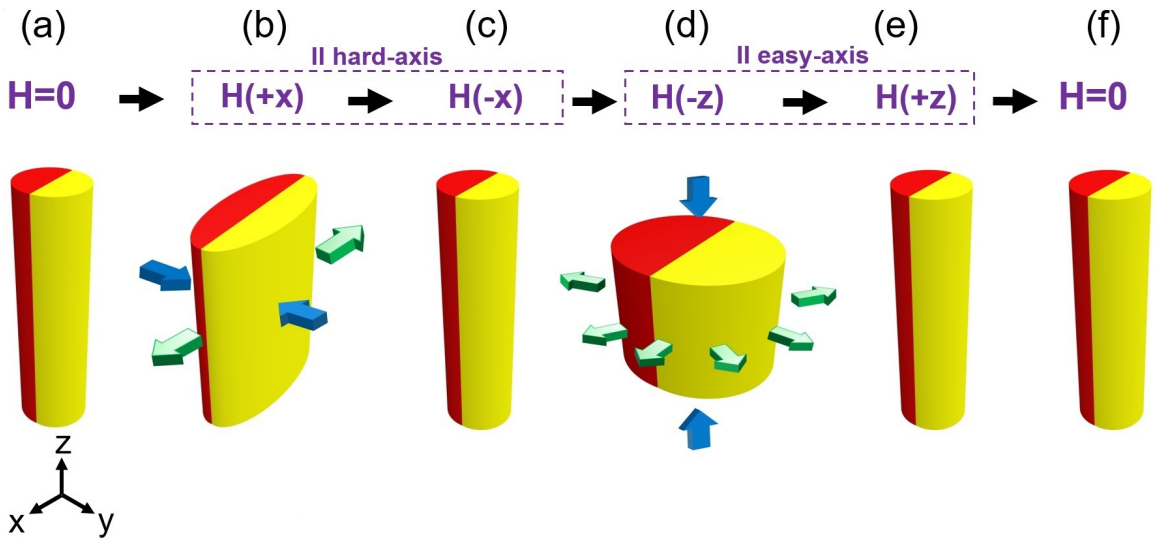

Figure 4.10 Schematic illustration of the first Janus nanofiber ensemble: (a) at zero magnetic field (b-e) under four different magnetic field directions and (f) after removing the field (corresponding to the magnetic field orientations shown in Figures 4.8(a-f)). Green and blue arrows show the expansion and compression directions, respectively.

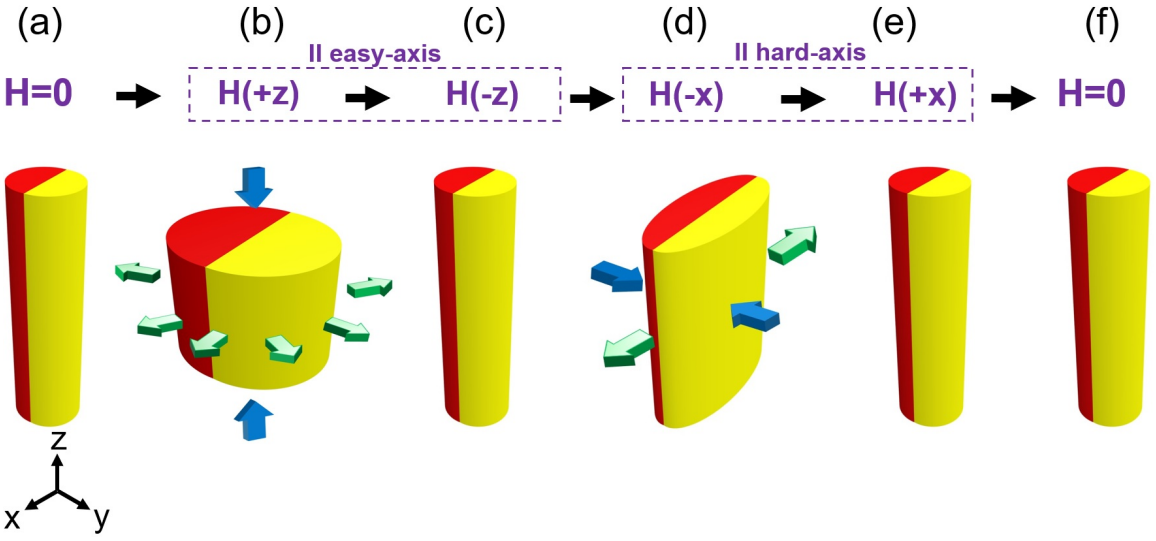

Figure 4.11 Schematic illustration of the second Janus nanofiber ensemble (corresponding to the magnetic field orientations shown in Figures 4.9(a-f)).

In the second pair (H(-z) and H(+z)), applying H(-z) along the CFO easy axis causes axial compression, and therefore a radial expansion (shown in Figure 4.10(d)) leading to a significant strain increase. This radial strain in x-y plane means much larger SHG for both excitation polarizations, as seen in Figure 4.8(d). In fact, it has been shown that rotating the field by 90° significantly increases both magnetostriction and piezoelectric effects compared to that from field reversal [36, 78]. Since the change in strain transferred from the CFO constituent is no longer uniaxial in this case, it can only be explained using tensors which our simple model does not consider. However, the model does qualitatively explain our results. Again, reversing the magnetic field in Figure 4.10(e) reduces the compressive stress in the CFO constituent such that it relaxes towards its unstressed state prior to H(-z), similar to that shown in Figure 4.10(c). As a result, it can be seen that the dipole projections in Figure 4.8(e) show a similar signal as Figure 4.8(c) (both pattern and intensity) and Figure 4.8(a) (only intensity because of the initial arbitrary state). In the last step, reducing the magnetic field to zero in Figure 4.10(f) decreases both magnetization and strain in CFO, leading to a slight reduction in SHG intensity but maintaining a similar pattern as shown in Figure 4.8(f). We can also apply this simple model to interpret the SHG from the second Janus nanofiber ensemble, as can be seen in Figure 4.11.

4.3.2 CFO asymmetric hysteresis loops

Here, we discuss the hysteresis behavior of the Janus nanofiber system in more detail. As mentioned earlier, since the 1.5 kOe field strength used is below the saturation field value for these fibers, the path that the magnetization traces as we move the magnet closer to the sample is different from the path as we move the magnet away. Unlike systems with symmetric hysteresis loops where magnetization magnitude remains unchanged upon full field reversal, such action in these nanofiber systems will actually lead to either higher or lower magnetization due to their asymmetric loops. Using the

asymmetric hysteresis loop, we provide physical explanations behind the qualitative changes at the four key transitions in the field sequence: 1) from zero field to the first applied field, 2) after field reversal, 3) 90° field rotation from easy to hard axis or vice versa, and 4) after field removal. Figure 4.12 provides schematics describing how the CFO constituents of both ensembles evolve along their respective magnetic hysteresis loops during the field sequence. The shape of the loops is from MOKE data previously conducted on these Janus nanofibers.

First, we assume the fibers possess some residual magnetization at zero field and hence are in an arbitrary state of strain. At the first key transition presented in Figures 4.12(b-i) and (b-ii), the application of H(+x) and H(+z) increase the magnetization in the +x direction for ensemble 1 and in the +z direction for ensemble 2, respectively. This first field puts ensemble 1 (2) at the starting point of a hard (easy) axis minor hysteresis loop.

Next, the second key transition is the reversal of the magnetic field. We have two instances of the second key transition occurring before and after the 90° field rotation. As previously discussed, the field reversal should in general lead to different magnetization and hence different strain from the starting point due to the asymmetric nature of the hysteresis behavior in these nanofibers. This is indeed what we observe in both ensembles 1 and 2, where the SHG signals in all four occasions (Figures 4.8(c) and (e), and Figures 4.9(c) and (e) are different from those prior to field reversal (Figures 4.8(b) and (d), and Figures 4.9(b) and (d)). Except for the first field reversal in ensemble 1 (from H(+x) to H(-x) in Figures 4.8(b) and (c)), all other field reversals lead to a decrease in the SHG intensity suggesting a reduction in magnetization and strain. However, since we do not have detection for SHG from dipoles lying in the x-direction, it is difficult to conclude definitively what is occurring on the BTO side due to the changing strain on the CFO side. It is also possible that the deformation in the BTO is plastic rather than elastic, leading to a more complex picture of the

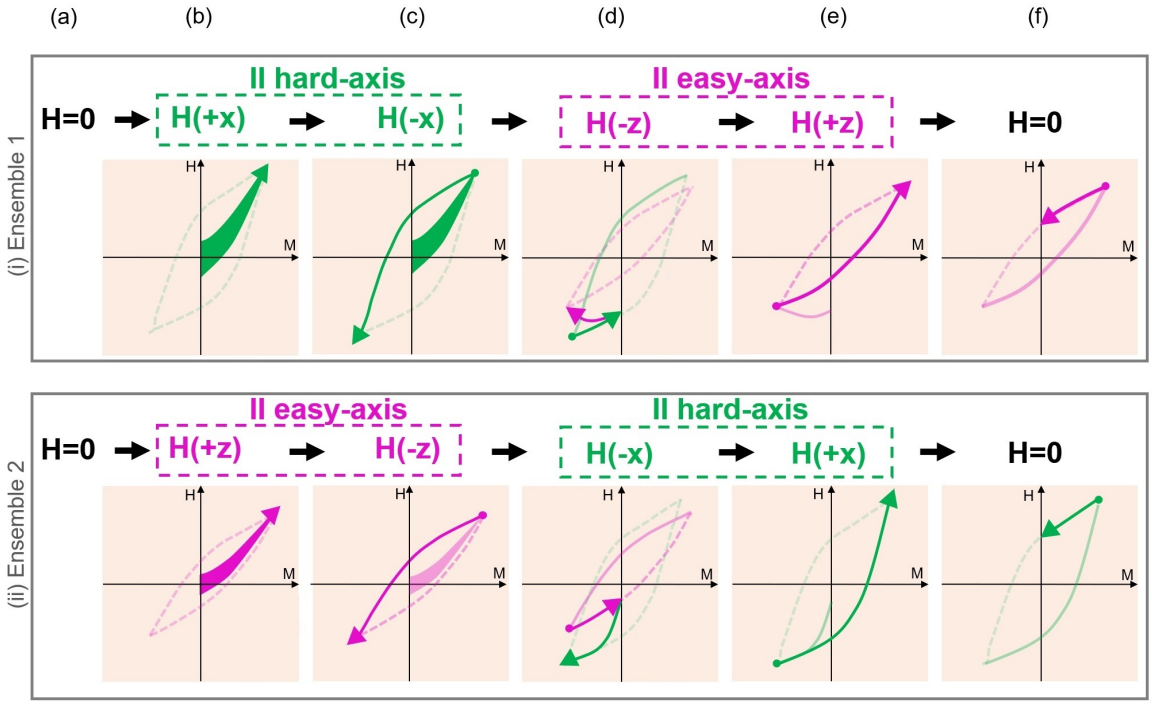

Figure 4.12 Schematic illustration of H-M hysteresis loop traces of the two Janus nanofiber ensembles 1(i) and 2(ii): (a) at zero magnetic field (b-e) under four different magnetic field directions and (f) after removing the field (corresponding to magnetic field orientations in Figures 4.8(a-f) and 4.9(a-f)). The hard and easy axis loops are shown in green and purple, respectively.

magnetoelectric coupling between the two constituents. This possibility will be explored more when we discuss the XRD data in the next section. In addition, we note that each field reversal is represented by a trace along the same hysteresis minor loop as seen in Figures 4.12(c) and (e), whereas the first and third key transitions (Figures 4.12(b) and (d)) involve deviations from the same loop. In particular, the 90° field rotation in the third key transition is represented by changing from a hard axis minor loop to an easy axis minor loop for ensemble 1 as shown in Figure 4.12(d-i) and vice versa for ensemble 2, as shown in Figure 4.12(d-ii).

At the last key transition, reducing the magnetic field to zero decreases both magnetization and strain only slightly in CFO, as seen in the hysteresis loop traces in Figures 4.12(f-i) and 4.12(f-ii). As expected, this leads to minimal change in the SHG patterns for both ensembles, as shown in Figures 4.8(f) and 4.9(f).

4.4 Probing the magnetically-induced strain with X-ray diffraction

In order to verify that the observed changes in the polarization-resolved SHG are indeed caused by the magnetoelectric coupling in the lattice constants and not from optical artifacts, XRD (Rigaku Ultima IV) with Cu K-alpha radiation and a wavelength of 1.5406 Å is performed on another Janus nanofiber ensemble with and without magnetic field at room temperature. We note that due to the restriction of the XRD equipment, we do not keep the magnet inside the instrument. Therefore, we apply and then remove the fields to load the sample into the chamber. In addition, a mica film is used here as the substrate.

First, the XRD measurement is performed with no magnetic field to document the initial state of this nanofiber ensemble (Figure 4.13). Then, H(+z) and H(+x) are applied to the sample, respectively, to analyze the effect of different magnetic field orientations on the lattice constants of the BTO and CFO constituents of the Janus nanofibers. The fields are applied via the same permanent bar magnet used in the

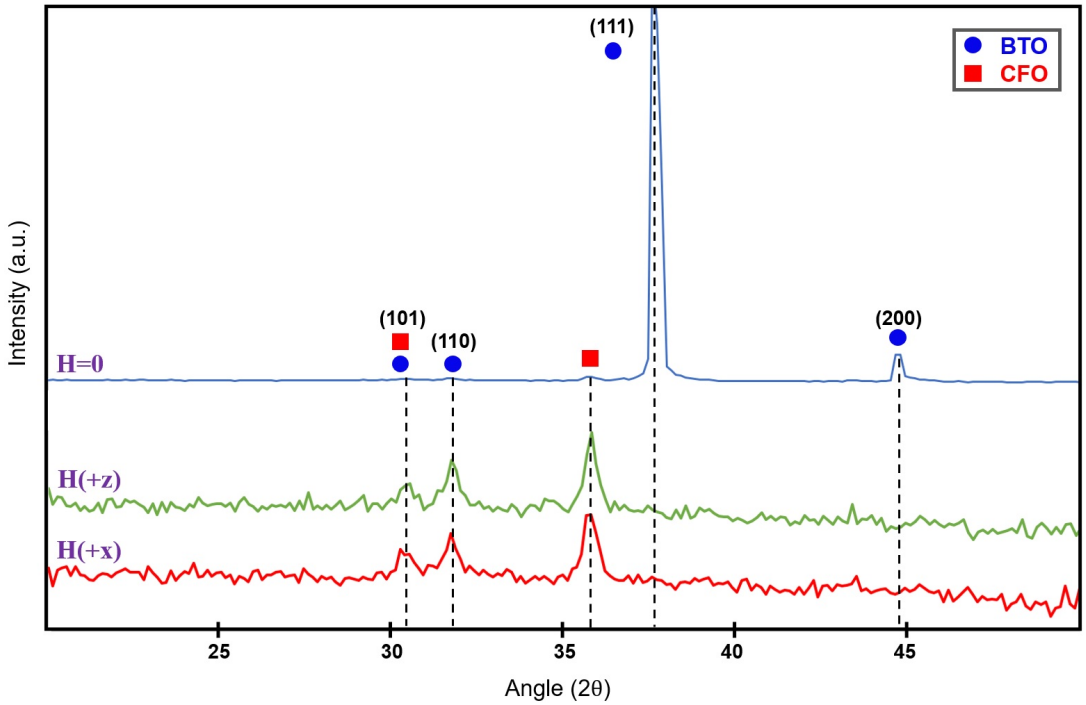

Figure 4.13 XRD patterns recorded for a BTO/CFO Janus nanofiber ensemble at room temperature. The spectra are indexed to BTO (blue circles) and CFO (red square). We begin with no magnetic field (H=0). Then, the H(+z) and H(+x) fields are applied. The 2θ scan is varied between 15° and 50°.

magnetic field-dependent SHG measurements ($\sim$ 1.5 kOe) for 5 minutes. When the H(+z) field is applied, it can be seen that the BTO (111) and (200) peaks disappear, and some other CFO and BTO peaks show up. However, when the H(+x) is applied, no significant changes are observed. After observing clear changes in the distinct peaks of both BTO and CFO while applying a magnetic field, we have decided to perform a more systematic field-sequence XRD study on a different ensemble, as illustrated in Figure 4.14.

For this ensemble, we again start with no magnetic field. Then, the XRD measurement is repeated on the same spot under the same condition to record the changes caused by H(+z) field. Similarly, H(-z), H(+z), H(+x), and H(-x) fields are applied respectively. Here, we have extracted the d-spacings of the 111 planes, d_{111}, for CFO under these five magnetic field directions using a simple Bragg's law calculation, $d_{111} = \frac{n\lambda}{2sin\theta_{111}}$. Here, n=1, l=1.5406 Å, and q is the angle of the diffracted wave. The 2θ value at which the 111 CFO peak appeared at its maximum intensity is used to determine q for each magnetic field condition, and the d-spacing is then calculated. At zero field, d_{111}=4.94 Å. After the application of H(+z) in the first key transition, we observe a drastic change in the CFO (111) peak which decreases and shifts to higher angles with a corresponding d_{111} = 4.82 Å, a sign of decreased lattice constant, suggesting compression, as expected. When we reverse the field during the second key transition, the CFO (111) peak goes back to a similar position to that of the zero field with a corresponding d_{111} = 4.91 Å. This change also agrees with the SHG data showing a general reduction in strain upon field reversal. However, as the field is switched back to H(+z) again, the CFO (111) peak does not recover its reduced d-spacing from the first applied H(+z) field but rather stays at a larger d-spacing of d_{111} = 4.96 Å. In fact, the CFO (111) peak stays at this d-spacing for the remainder of the field sequence.

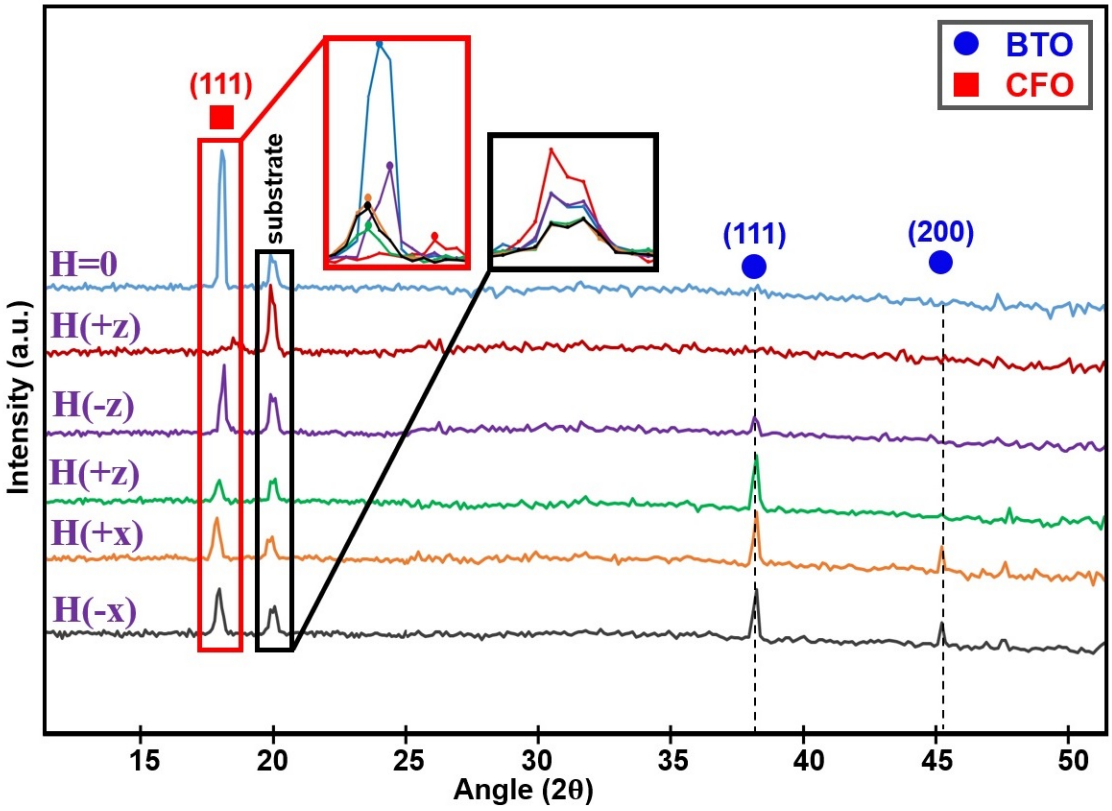

Figure 4.14 XRD patterns recorded for a BTO/CFO Janus nanofiber ensemble. The spectra are indexed to BTO (blue circles) and CFO (red square). We begin with no magnetic field (H=0). Then, the fields are applied in the order of (+z), (-z), (+z), (+x), and (-x) directions. The zoom-in view of the CFO (111) and substrate peaks in the insets indicate that the substrate peaks do not shift.

If we follow the BTO (111) peak, we see a similar trend in terms of repeatability, where it starts as a low peak, disappears as the first H(+z) field is applied, returns upon field reversal, and continues to grow after the second H(+z) field is applied. This suggests plasticity instead of elasticity in the coupling. The third key transition of 90° field rotation (going from +z to +x) is equally significant in the XRD measurements. Here we see a sudden appearance of the BTO (200) peak, which can be related to the drastic change observed in our SHG measurements.

The schematic of the hysteresis loop traces for the field sequence used in the XRD can also be seen in Figure 4.15. Lastly, the 2D XRD plots of the second ensemble used in XRD measurements are shown in Figure 4.16. The well-defined diffraction spots validate modeling the behavior in these fiber ensembles as a single fiber.

4.5 Chapter summary

This chapter began with the power-dependent SHG measurements performed on CFO, BTO, PVA solution, a glass substrate, and an ensemble of BTO/CFO Janus nanofibers. We observed that only the BTO and BTO/CFO nanofibers showed a quadratic behavior, confirming that our SHG measurement method only monitors the BTO constituent of the Janus ensembles. We also used a BBO crystal and permalloy film to ensure the alignment of the collection path in our optical setup. Afterward, we applied a magnetic field to BTO to verify that this constituent of the Janus system does not respond to the magnetic field. Next, when we applied the field to Janus nanofibers, we observed clear changes in the polarization-resolved SHG data for different magnetic field orientations. This behavior indicates the magnetodielectric coupling effect in this multiferroic system.

In order to better visualize the observed field-dependent changes, we used a simple toy model to describe the overall geometry of the fibers and their deformation when a field is applied along the easy and hard axes of the magnetostrictive CFO. In this

simple model, we assumed that the field reversal reduces the system strain because of the asymmetric hysteresis loops of our nanofibers. However, reversing the field can actually either reduce or increase the system strain leading to a higher or lower magnetization. We investigated this effect by mapping the possible hysteresis loops for each magnetic field direction in our field sequence study. Lastly, we performed the magnetic field-dependent XRD measurements to confirm that the observed changes in the SHG data are indeed from the changes in the BTO and CFO lattice constants caused by the magnetoelectric coupling effect.

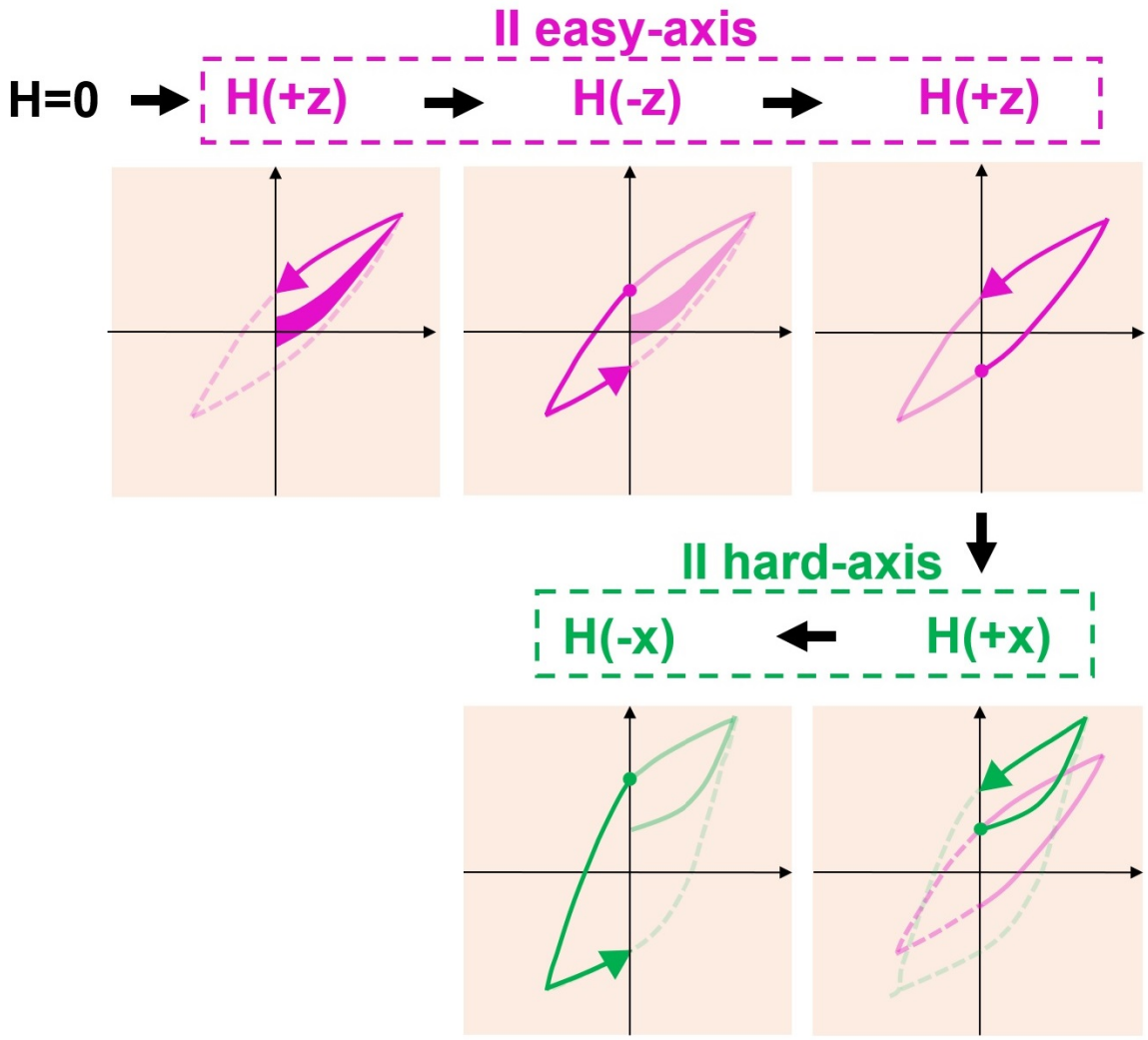

Figure 4.15 Schematic illustration of H-M hysteresis loop traces for the field sequence used in the second XRD measurements. The hard and easy axis loops are shown in green and purple, respectively.

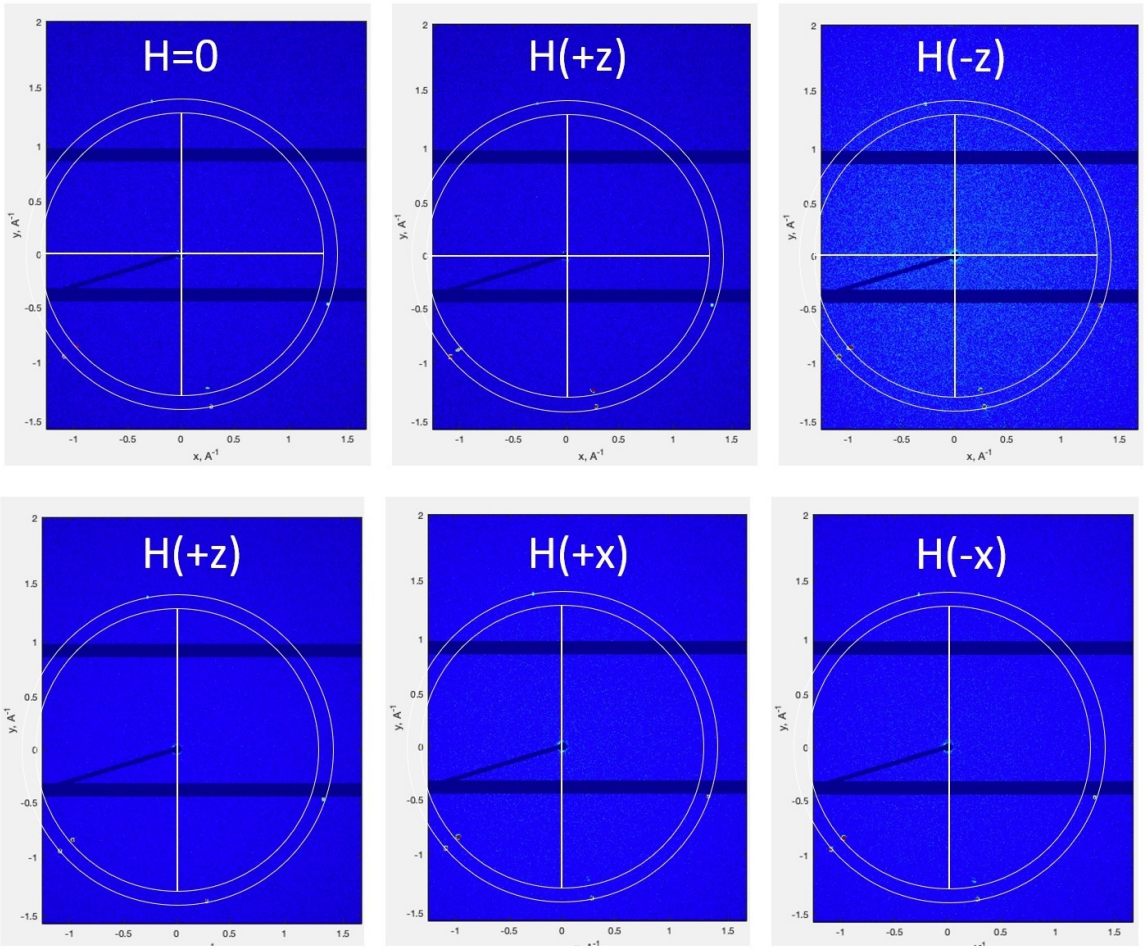

Figure 4.16 2D XRD patterns recorded from the Janus nanofiber ensemble used in the second magnetic field-dependent XRD measurements (Figure 4.14).

Chapter 5

Theory and characterization of InAs/GaAs self-assembled quantum dots

5.1 Theory of semiconductor quantum dots

Nanostructured materials can be classified into three categories depending upon the number of degrees of freedom that the charge carriers experience within them: two-dimensional wells, one-dimensional fibers, and zero-dimensional dots in which the carriers are confined in one, two, and three dimensions, respectively. Confining charge carriers in all three dimensions leads to unique properties in quantum dots (QDs), which are the main focus of this work.

5.1.1 semiconductor materials

In a semiconductor material, the energy bands consist of a series of closely spaced energy levels. The highest occupied energy band at absolute zero kelvin is referred to as the valence band, and the lowest unoccupied energy band is referred to as the conduction band. The Fermi level lies between the valence and conduction bands in pure semiconductors, making them energetically separated. In a semiconductor material in its ground state, the conduction band is empty while the valence band is fully occupied with electrons. When these electrons are optically excited to the conduction band, they leave behind a "hole" in the valence band. This positively charged hole can then couple to a negatively charged electron by an attractive Coulomb interaction, forming a quasiparticle called the exciton.

In order for an electron to transit from the valence band to the conduction band, a minimum amount of energy is required, which is called the band gap or energy gap and is typically measured in electron volts (eV). When electrons transit to the conduction band, they can freely move and conduct the electric current through the crystal. Therefore, the band gap is an important factor in determining the electrical conductivity of a material. In particular, insulators generally have large band gaps that prevent conductivity in them, while semiconductors have smaller band gaps. On the other hand, conductors with either very small or no band gaps have high electrical conductivity even in the presence of weak fields.

Moreover, there are two different types of band gaps in semiconductors depending on their electronic band structure: direct and indirect. In materials with a direct band gap, the minimum of the conduction band and the maximum of the valence band are directly on top of each other in k-space. Therefore, no change in momentum is required for the electron transition. As a result, these materials can absorb and emit light efficiently. On the contrary, the electron transition cannot occur without a change in momentum in semiconductors with an indirect band gap.

5.1.2 SEMICONDUCTOR QUANTUM DOTS

QDs are nanostructures made of semiconductors in which the excitons are confined in all three spatial dimensions, analogous to "particle-in-a-box". QDs with unique size- and shape-dependent optical and electronic properties are an attractive candidate for a variety of promising applications in the nanoscale region, such as solar cells, diode lasers, and medical imaging [79, 80, 81, 82]. A single QD contains a hundred to a few thousand atoms with diameters typically in the range of 2 to 10 nanometers. However, they exhibit properties intermediate between macroscopic semiconductors and atoms. In addition, because some of their important properties, such as their discrete energy levels, can be compared to individual atoms, they are known as "artificial atoms".

5.2 Characterization of MBE grown quantum dots

The sample studied in this work contains indium arsenide (InAs) self-assembled quantum dots that are fully encapsulated in gallium arsenide (GaAs). Both these materials are semiconductors with a direct band gap. In this section, we will begin with an overview of GaAs properties first. Then, we will discuss the growth method used to form our QDs as well as the structure of the particular sample used here.

5.2.1 characterization of GaAs

GaAs is a notable material with various applications ranging from lasers and LEDs to quantum computing and energy-harvesting devices [24, 25, 27, 28, 29, 83, 84]. This compound semiconductor consists of gallium (Ga), an element from group III, coupled with arsenic (As), an element from group V of the periodic table. GaAs has a zinc-blende crystal structure with a face-centered cubic translational symmetry. The non-centrosymmetric structure of GaAs is shown in Figure 5.1, where the As and Ga atoms are represented in red and blue, respectively. It can be seen that this conventional unit cell is composed of four GaAs molecules where As atoms bond to four Ga atoms and each atom of Ga bonds to four As atoms. As a result, there are four As atoms and fourteen Ga atoms in this cell.

The band gap energy of GaAs (E_g) depends on the temperature (T), and can be calculated using the following equation:

$$E_g(T) = 1.519 - 5.405 \times 10^{-4} \frac{T^2}{T + 204}, \tag{5.1}$$

where T and E_g are typically measured in K and eV, respectively [85].

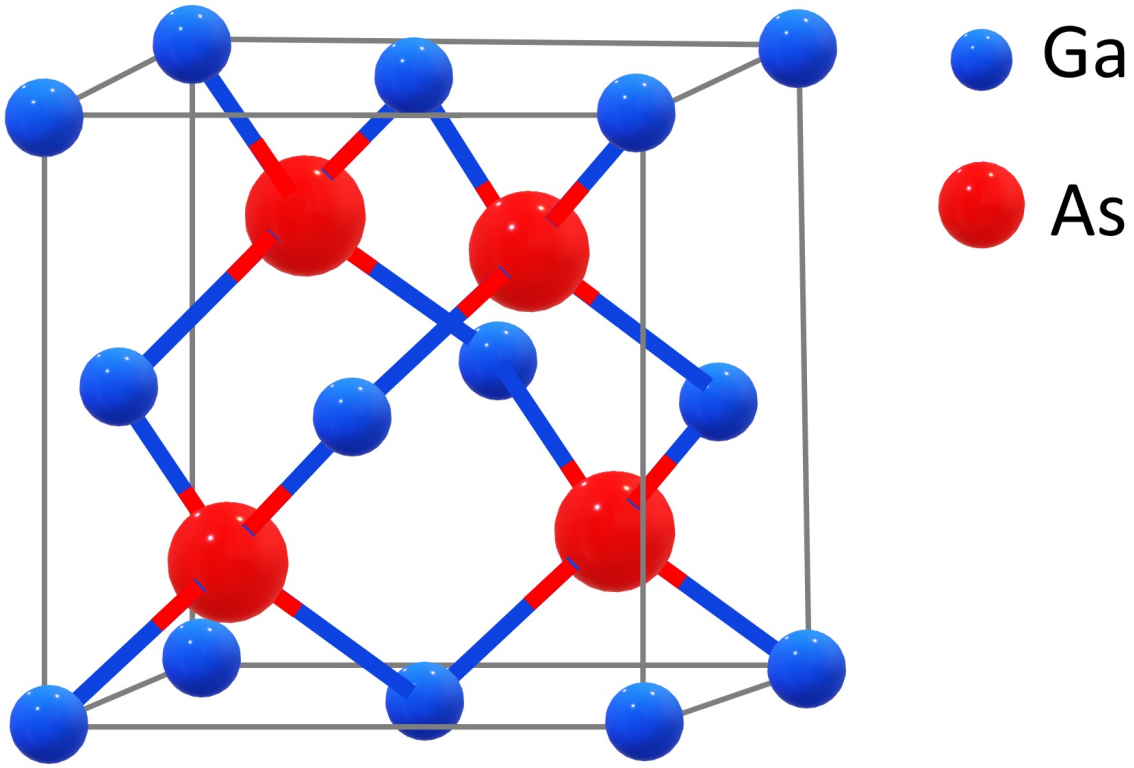

Figure 5.1 Schematic representation of a conventional unit cell of GaAs with the cubic zinc-blende crystal structure. As and Ga atoms are shown in red and blue, respectively. Each As atom is bonded to four Ga atoms, and each Ga atom is bonded to four As atoms.

So, the band gap energy of GaAs is $E_g = 1.422$ eV at room temperature. Compared with other semiconductors such as silicon, GaAs is more stable over a wider temperature range with a high level of carrier mobility. Additionally, the band gap energy of InAs, the other semiconductor used in our sample, is $E_g = 0.354$ eV at room temperature, which is smaller than the GaAs band gap [86].

5.2.2 MBE grown quantum dots

The QDs studied in this work are grown using the molecular beam epitaxy (MBE) technique at the Naval Research Laboratory. MBE is a widely used method to grow semiconductor heterostructures. In general, there are three main epitaxial growth modes: layer-by-layer (Frank-van der Merwe), 3D islanding (Volmer-Weber), and layer-by-layer followed by 3D islanding (Stranski-Krastanov). In the latter mode, which is used to grow our sample, the QDs form as a result of the lattice mismatch between different semiconductor crystal structures.

In our particular sample, a monolayer of InAs is epitaxially grown on a surface of GaAs. GaAs and InAs have a lattice mismatch of ~ 7 % where the lattice constant is 5.6533 Å in GaAs, and 6.0584 Å in InAs [87]. This monolayer of InAs adopts the lattice constant of GaAs and forms a thin layer known as the wetting layer. As the wetting layer thickens, the mismatch between these two materials causes more strain, and therefore increases the free energy of the system. At a critical thickness, it is energetically more favorable for atoms to nucleate three-dimensional islands than keeping the lattice constant of the substrate. As a result, the islands form on top of the wetting layer to reduce the free energy of the system.

5.2.3 Sample structure

Our sample is grown on top of a 500 nm Si-doped GaAs buffer layer which is mounted on a 500 μm N+ GaAs wafer. Then, a 30 nm layer of undoped GaAs is grown on

top of the buffer layer. The InAs self-assembled QDs are formed atop this layer with a nominal thickness of 2.8 nm. There is a 150 nm layer of undoped GaAs on the top of all these layers to encapsulate the QDs. This top layer is called the capping layer. The structure of our QD sample is shown in Figure 5.2.

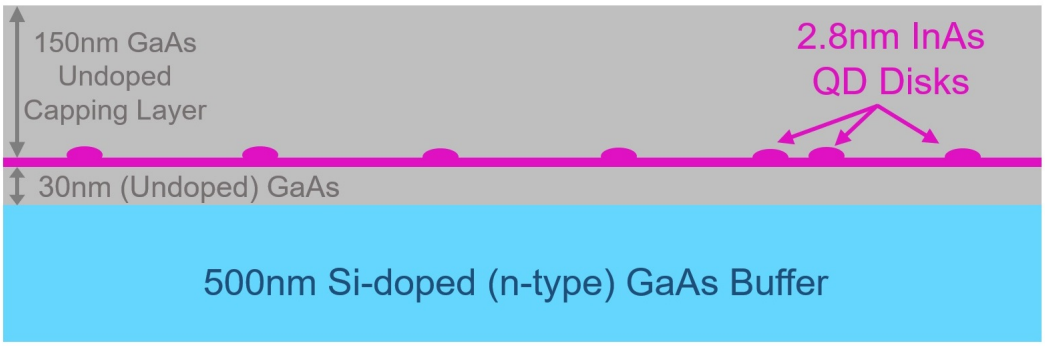

Figure 5.2 Structure of the QD sample grown by MBE.

5.3 Hybrid plasmonic/QD device

In order to fabricate the hybrid plasmonic/QD device studied in this work, the electron-beam lithography (EBL) and optical lithography (photolithography) techniques were initially used. However, in order to obtain more precise features with a higher resolution, we decided to use a thermal probe nanolithography system (NanoFrazor Explorer, Heidelberg Instruments Nano) to define the shape of the plasmonic structures. NanoFrazor is a maskless fabrication tool based on thermal scanning probe lithography. The patterns can be precisely written with either an ultra-sharp heatable silicon tip (with a radius of > 10 nm and about 750 nm length) for nanoscale features, or a CW laser (405 nm wavelength CW fiber laser source with the beam waist of about 1 μm, and up to 150 mW output power on the sample) for microscale features.

The fabrication process starts with cleaning the sample surface, and then coating it with two layers: a layer of a lift-off resist and a layer of a thermal resist. Then, the thermal resist is evaporated using the NanoFrazor in the desired areas. Afterward, the etching process is performed to have the plasmonic structures closer to the embedded QDs. In general, this step can be done using two methods: wet etching and dry etching. Some of the main advantages and disadvantages of these two methods are shown in table 5.1. Wet and dry etching are generally isotropic and anisotropic, respectively. The main difference between these two is in their vertical and lateral etching rates. In the isotropic etching, the sample is etched uniformly in all directions at the same rate, leading to undercutting. In contrast, the vertical etch rate is different from the lateral etch rate in the anisotropic case. The lateral etch ratio can also be defined as R_L = horizontal etch rate/vertical etch rate, where $R_L = 1$ for isotropic etching, $0 < R_L < 1$ for anisotropic etching, and $R_L = 0$ for directional etching.

Table 5.1 Some of the advantages and disadvantages of the wet and dry etching.

	Wet Etching	Dry Etching
Advantage	-Low cost -Fast with high etching rate -Good material selectivity	-Able to define small features -More repeatble -Capable of automating
Disadvantage	-Unable to define small features -Chemical contamination issues -Poor repeatability	-High cost -Poor selectivity -Toxicity of some gases
Directionality	Isotropic	Anisotropic

In order to obtain high-resolution features with sharp sidewalls, anisotropic dry etching, such as reactive-ion etching (RIE), would be an ideal process. In addition, the ideal gas to etch GaAs in our sample would be chlorine. However, this gas is not available at our facilities due to its extreme toxicity level. A proper alternative to chlorine would be Freon-12 (CCl2F2) which is banned to protect the ozone layer, and therefore it is also not available. Consequently, we used the chemical wet etching method in this fabrication process.

This etching step is followed by depositing a silver film to support the SPP modes. Then, the resists are lifted off, and the entire sample is coated by a semi-transparent layer of chromium (Cr) to form a Schottky diode. When the fabrication process is completed, atomic force microscopy (AFM) is used to accurately determine both the vertical and lateral dimensions of the etched grooves. Despite using the chemical wet etching method, high-resolution grooves with sharp sidewalls are achieved, as can be seen in Figure 5.3. A schematic diagram of the fabrication process is also illustrated in Figure 5.4. The details of this process can be found in Appendix A.

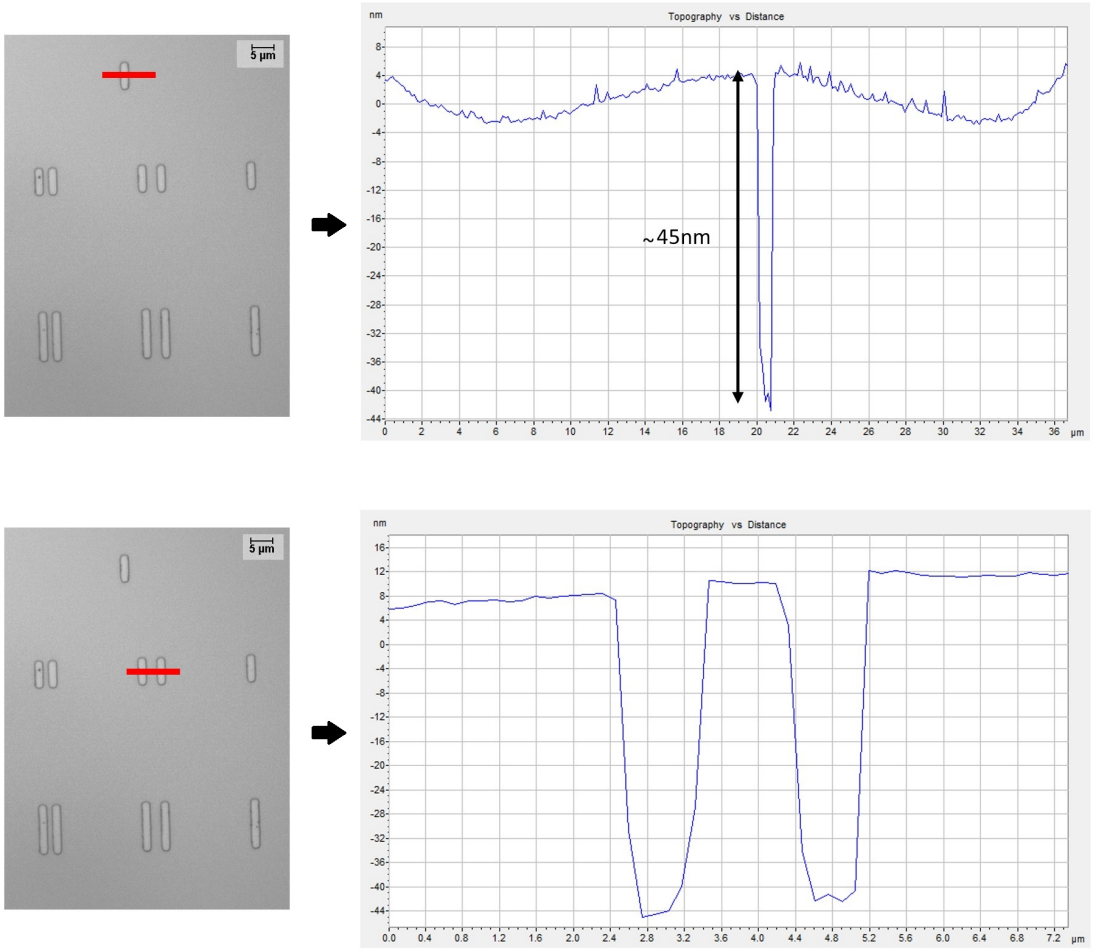

Figure 5.3 AFM images and corresponding line scans of three etched grooves after depositing 60 nm of Ag and 5 nm of Cr. The illustrated depth profiles confirm that the capping layer is etched down to $\sim$ 110 nm with sharp sidewalls.

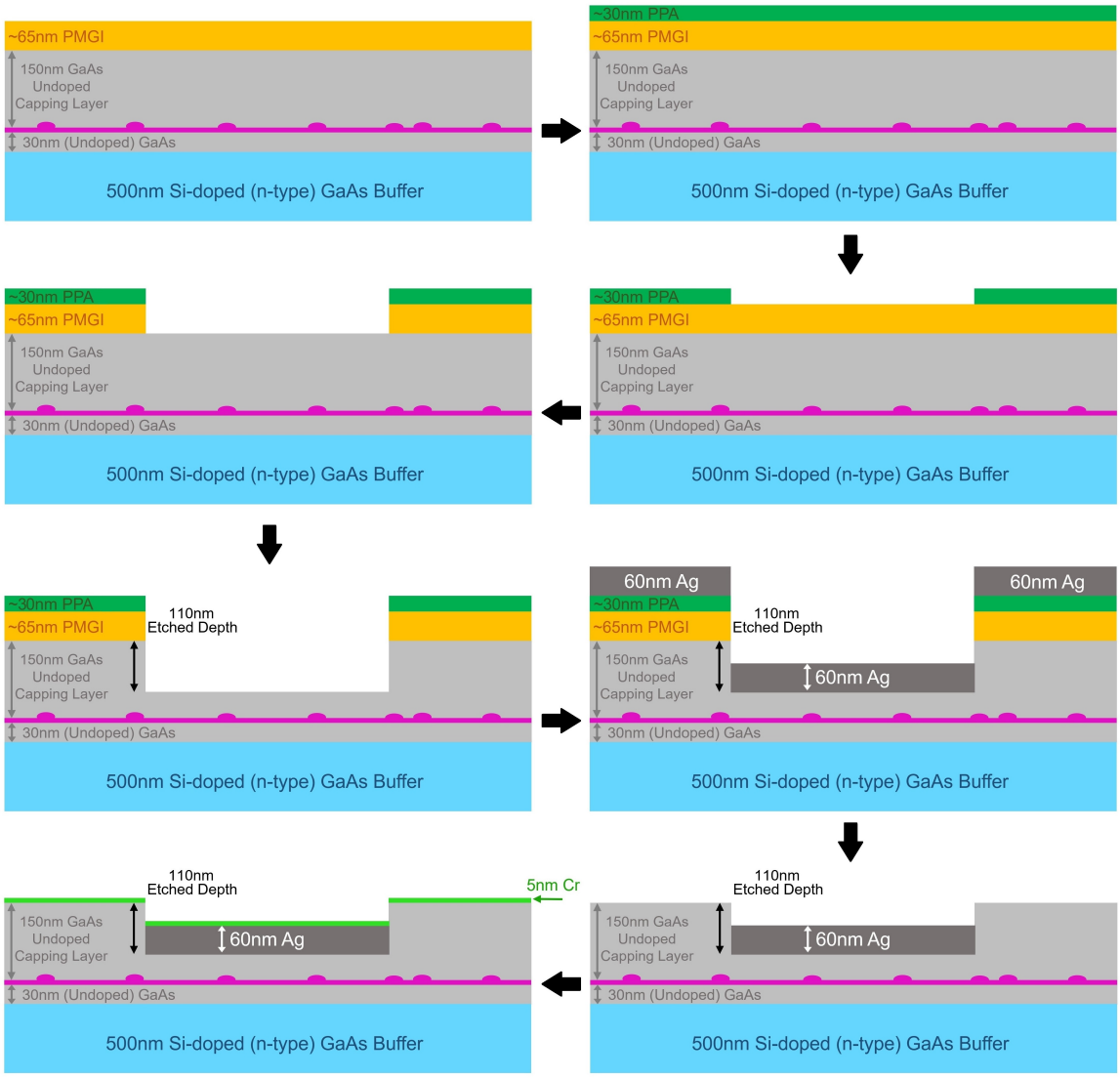

Figure 5.4 Schematic diagram of the fabrication process.

Lastly, the sample is affixed to a chip carrier and electrically gated by connecting the top and bottom surfaces to two electrodes. Upon completion of all of the above steps, the sample is mounted inside the specimen chamber of a Cryostatation (Montana Instruments) and stabilized at 4 K in order to suppress any thermal noise. Additionally, connecting the electrodes to a lock-in amplifier allows us to apply an external bias across the sample. The schematic illustration of the post-fabrication structure of our hybrid plasmonic/QD device and the corresponding energy band diagram of the Schottky diode are illustrated in Figure 5.5.

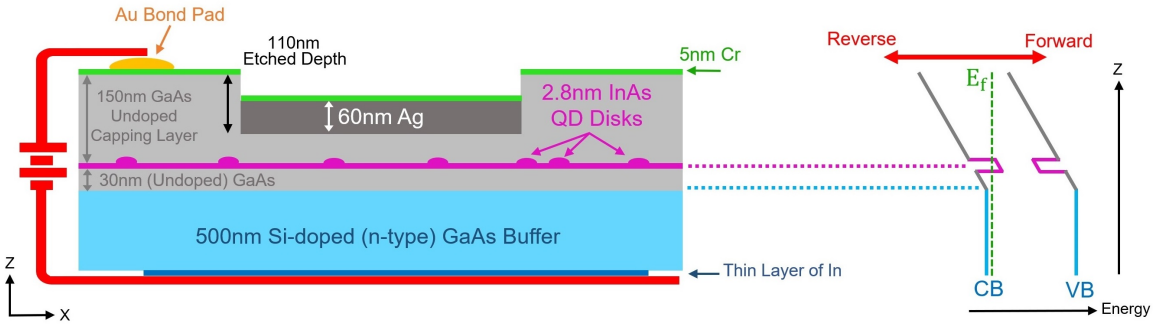

Figure 5.5 Post-fabrication structure of the hybrid plasmonic/QD device. The corresponding energy band diagram is shown on the right. CB, VB, and E_f stand for conduction band, valence band, and Fermi energy, respectively.

5.4 Background theory of surface plasmon polaritons

The coupling between the delocalized electron oscillations and the electromagnetic excitations that propagate along a conductor–dielectric or conductor–air interface at certain frequency regimes can be described by surface plasmon polaritons (SPPs). These evanescent waves decay exponentially into both neighboring media as they move away from the interface (Figure 5.6). In order to characterize these delocalized electrons, this section begins with a brief overview of the Drude-Lorentz model. In addition, since SPPs are electromagnetic surface waves, we will use the macroscopic Maxwell's equations to obtain the general form of the wave equation and the material dispersion relations. Then, using these relations as well as defining a propagation geometry, we will explain the SPPs at a single interface between two media. Afterward, we will obtain the relationship between the dielectric functions of these two materials by applying appropriate boundary conditions at the interface. Lastly in this section, we will discuss the dispersion relations for two different polarizations and will show that only one of them can support SPPs. We also note that we will only discuss nonmagnetic, isotropic, and homogeneous media here.

5.4.1 the Drude-Lorentz model

Charge carriers in conductors play an important role in the existence of surface waves. The optical response of these carriers can be predicted using the Lorentz and Drude models. In particular, the Lorentz model describes insulators, whereas the Drude model considers the semiconductors and conductors [88]. These two models, or a combination of them, are also sometimes referred to as the Drue-Lorentz model in some literatures.

Recall that in the Lorentz oscillator model in section 3.1, the electrons are bound to the nucleus forming an electron-spring system. Therefore, using Newton's second

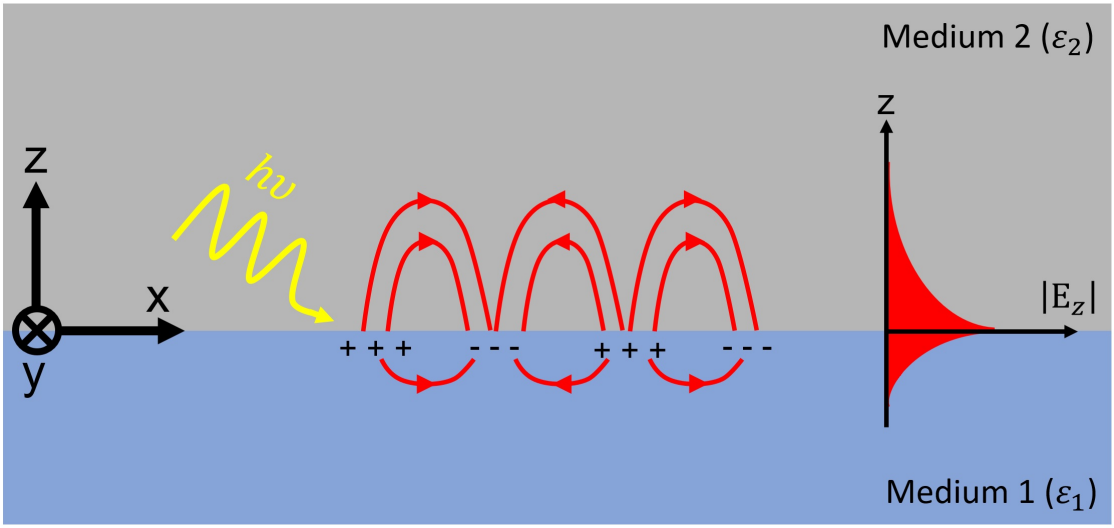

Figure 5.6 A simple schematic of an SPP wave propagating along a conductor–dielectric interface. The associated exponential decay of field along the x direction with maximum amplitude at $z = 0$ is shown on the right.

law, the motion of an electron in the presence of a time-dependent electric field, $\mathbf{E} = \mathrm{E}_0 e^{-i\omega t}$, with an amplitude of E_0 and angular frequency of ω can be expressed as:

$$m\frac{d^2\mathbf{r}}{dt^2} = \mathbf{F}_{total} = \mathbf{F}_{spring} + \mathbf{F}_{damping} + \mathbf{F}_{driving} = -m\omega_0^2\mathbf{r} - m\gamma\frac{d\mathbf{r}}{dt} + e\mathbf{E}, \tag{5.2}$$

where m, ω_0, and $\mathbf{r}$ in $\mathbf{F}_{spring}$, which can be described by Hooke's law, are the mass of the electron (9.109×10^{-31} kg), the natural oscillation frequency ($\sqrt{k_{spring}/m}$), and the displacement of the electron from equilibrium, respectively. The second force, $\mathbf{F}_{damping}$, describes the velocity-dependent damping force on the electron with the linear damping coefficient γ. And finally, e and $\mathbf{E}$ in $\mathbf{F}_{driving}$ represent the absolute value of the electron charge and the driving electric field, respectively. We note that the magnetic force is neglected. Rearranging the above equation results in:

$$\frac{d^2\mathbf{r}}{dt^2} + \gamma\frac{d\mathbf{r}}{dt} + \omega_0^2\mathbf{r} = \frac{e}{m}\mathbf{E}. \tag{5.3}$$

Assuming the solution to this equation is $\mathbf{r} = r_0 e^{-i\omega t}$, r_0 can be obtained as follows:

$$r_0 = \frac{eE_0}{m(\omega_0^2 - \omega^2 - i\omega\gamma)}. \tag{5.4}$$

The imaginary term in the denominator indicates that the motion of the electron is out of phase with respect to the driving electric field. In addition, using the above equation, dipole moment can be written as:

$$\mathbf{p} = e\mathbf{r} = \frac{e^2\mathbf{E}}{m(\omega_0^2 - \omega^2 - i\omega\gamma)}. \tag{5.5}$$

If there are N non-interacting oscillators per unit volume, we can define the relative dielectric function of this set of oscillators, $\varepsilon_r(\omega)$, using the equations 3.1 and 3.8 and $\mathbf{P} = \varepsilon_0(\varepsilon_r - 1)\mathbf{E}$, as:

$$\varepsilon_r(\omega) = \frac{\varepsilon}{\varepsilon_0} = 1 + \frac{Ne^2}{m\varepsilon_0}\Big(\sum_j \frac{f_j}{\omega_j^2 - \omega^2 - i\gamma_j\omega}\Big), \tag{5.6}$$

where f_j is the oscillator strength. Here, only the first linear order is shown, and all higher-order effects are neglected for simplicity.

Unlike insulators, electrons in conductors and semiconductors are not bound to their nuclei. In this case, the Drude model can be used to describe the behavior of these delocalized carriers. In this model, the metal is formed of a collection of heavy immobile ions, whereas the gas of electrons can move freely. When electrons collide with the heavy ions with a probability per unit time, $1/\tau$, they scatter randomly in different directions having a new velocity. Here, τ is known as the collision time and is independent of the position or velocity of the electron. The new velocity of electrons is also independent of their initial velocity but changes according to the temperature of the region where the collision happened. We note that the effect of the electron-electron interaction is ignored here. The natural oscillation frequency can also be ignored ($\omega_0 = 0$) since the electrons are not bound to the nucleus, unlike the Lorentz model. Therefore, in the presence of an electric field, r_0 can be obtained as follows:

$$r_0 = \frac{eE_0}{m^*(-\omega^2 - i\omega/\tau)}, \tag{5.7}$$

where m^* is the effective mass of the electron. Then, the dipole moment and the polarization expressions give us:

$$\varepsilon_r(\omega) = 1 - \frac{\omega_p^2}{\omega^2 + i\omega/\tau}, \tag{5.8}$$

where $\omega_p = \sqrt{\frac{Ne^2}{m^*\varepsilon_0}}$ is called the plasma frequency. For a plane wave that is propagating along the x-direction, i.e. $E = E_0 e^{i(k_x x - \omega t)}$ and E_0 is independent of time, by setting $\tau \to \infty$ and substituting the propagation constant $k_x = \frac{\omega}{c}\sqrt{\varepsilon_{metal}}$ into the above equation, we get:

$$k_x = \frac{\omega}{c}\sqrt{1 - \frac{\omega_p^2}{\omega^2}}, \tag{5.9}$$

where k_x can be either real or imaginary depending upon the frequency ω. If $\omega > \omega_p$, k_x becomes a real number, and the metal behaves like dielectrics. However, when the frequency is smaller than the plasma frequency ($\omega < \omega_p$), k_x becomes imaginary. In this case, the electromagnetic waves propagate along the surface of the metal, and the coupling between the light and the collective electron oscillations results in an exponentially decaying field. This property will be discussed in more detail in the following section.

5.4.2 Propagation of electromagnetic waves

In this section, we will first discuss the general form of the wave equation using the macroscopic Maxwell's equations. Then, we can derive explicit expressions for the electric and magnetic field components by considering the polarization of the incident light, and also using the Helmholtz form of the wave equation in a one-dimensional configuration.

By taking the curl of the Maxwell's curl equations (3.4 and 3.5) in the absence of external charge and current densities and using the vector operator identity, $\nabla \times (\nabla \times \mathbf{A}) \equiv \nabla(\nabla \cdot \mathbf{A}) - \nabla^2 \mathbf{A}$, we obtain:

$$\nabla \times \nabla \times \mathbf{E} = \nabla \times (-\frac{\partial \mathbf{B}}{\partial t}). \tag{5.10}$$

Thus, the electric wave equation can be derived as:

$$\nabla^2 \mathbf{E} - \frac{\varepsilon}{c^2} \frac{\partial^2 \mathbf{E}}{\partial t^2} = 0, \tag{5.11}$$

since $\nabla \cdot \mathbf{D} = \nabla \cdot (\varepsilon \mathbf{E}) = 0$ in free space. A similar wave equation can also be obtained for the H field. Therefore, for the electromagnetic waves propagating at the speed of light, $c = \frac{1}{\sqrt{\mu_0 \epsilon_0}} = 3.00 \times 10^8$ m/s, the general form of the wave equation is:

$$\nabla^2 \mathbf{F} - \frac{\varepsilon}{c^2} \frac{\partial^2 \mathbf{F}}{\partial t^2} = 0, \tag{5.12}$$

where F can be either the **E** or **H** field. The general form of a harmonic plane wave can also be written as:

$$\mathbf{F}(\mathbf{r},t) = \mathbf{F}(\mathbf{r})e^{-i\omega t}, \tag{5.13}$$

which gives us the Helmholtz form of the wave equation, after inserting into equation 5.12:

$$\nabla^2\mathbf{F}(\mathbf{r},t) + (\varepsilon(\frac{\omega}{c})^2)\mathbf{F}(\mathbf{r},t) = 0, \tag{5.14}$$

where $(\frac{\omega}{c})$ is the propagation wave vector in vacuum. The next step to characterize the surface waves is defining a propagation geometry. Here, we consider a simple one-dimensional system where a surface wave propagates along the x-direction in the x-z plane of a cartesian coordinate system, as shown in Figure 5.7 (a). In this simple system, permittivity depends only on one spatial coordinate, meaning $\varepsilon = \varepsilon(z)$. Therefore, the propagating waves at z = 0 can be expressed as:

$$\mathbf{F}(x,y,z) = \mathbf{F}(z)e^{ik_x x}. \tag{5.15}$$

Inserting this equation into equation 5.14 results in:

$$\frac{\partial^2\mathbf{F}(z)}{\partial z^2} + (\varepsilon(z)(\frac{\omega}{c})^2 - k_x^2)\mathbf{F}(z) = 0. \tag{5.16}$$

It can be shown that the above equation has complex exponential solutions, meaning that the electromagnetic fields decay exponentially away from the interface in the form of $\mathbf{F}(z) = \mathbf{F}_1 e^{+k_1 z}$ and $\mathbf{F}(z) = \mathbf{F}_2 e^{-k_2 z}$ for $z < 0$ and $z > 0$ regions, respectively. We note that the real parts of both k_1 and k_2 are positive here.

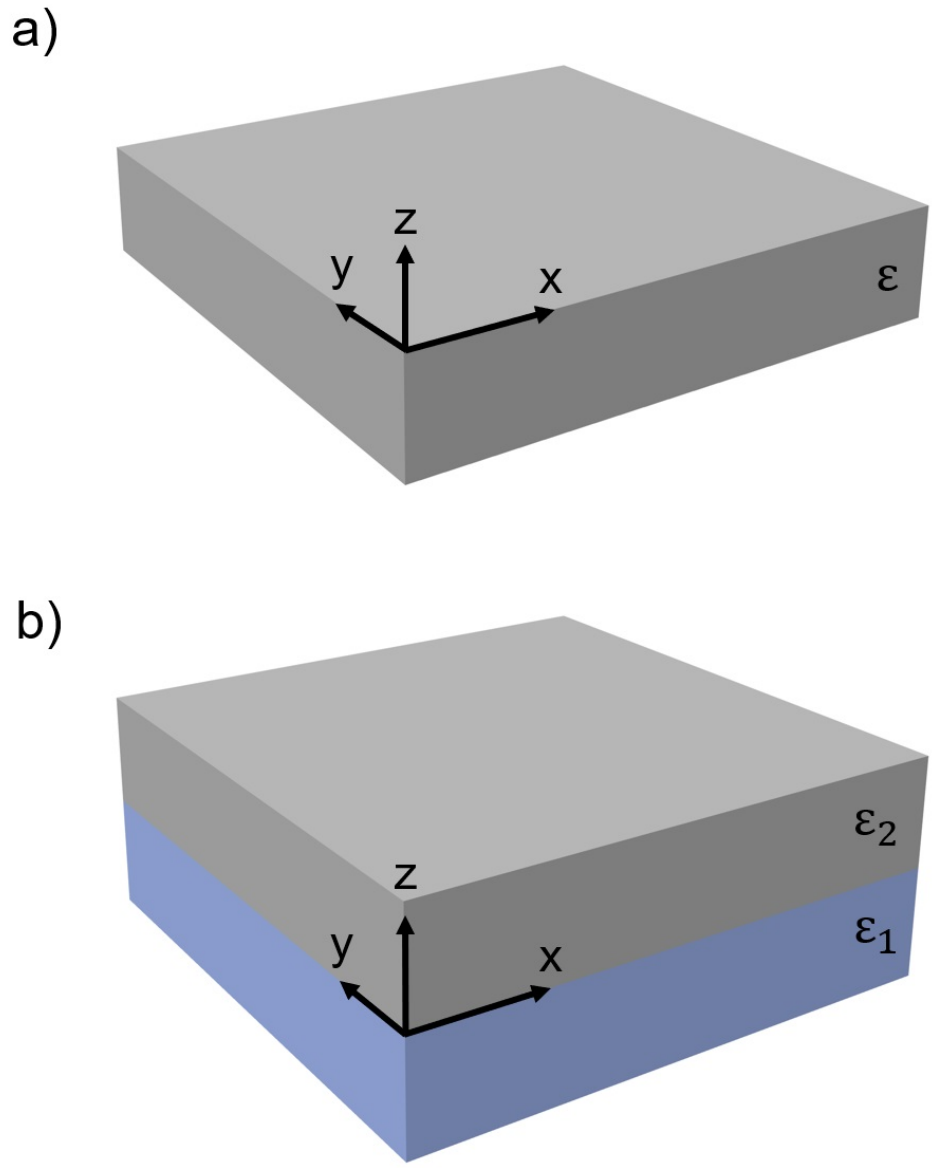

Figure 5.7 (a) Geometry for a surface wave propagation along a flat plane in the x direction. (b) Geometry for a surface wave propagation along a single interface at z = 0 that separates medium 1 with permittivity ε_1 at z < 0 region and medium 2 with ε_2 at z > 0 region.

Now in order to find explicit expressions for different components of E and H fields using the wave equation, we should consider the polarization of the incident light. There are two possible directions for incident polarization. When the magnetic field is normal to the plane of incidence and the electric field is parallel to it, we have the p-polarized transverse magnetic mode or TM. And, when the electric field is normal to the plane of incidence and the magnetic field parallel to it, we have the s-polarized transverse electric mode or TE. For an electromagnetic field with the angular frequency ω traveling in the x-z plane, it can be shown that the only non-zero field components for the TM polarized mode are E_x, E_z, and H_y. In contrast, the H_x, H_z and E_y are the non-zero field components for the TE polarized mode. Therefore, if Maxwell's equations are applied to a wave that is propagating along the x-direction ($\frac{\partial}{\partial x} = ik_x = |k_x|$), and is homogeneous in the y-direction ($\frac{\partial}{\partial y} = 0$), the wave equation for such a wave with TM polarization and in terms of the only non-zero H field component can be written as:

$$\frac{\partial^2 H_y}{\partial z^2} + (\varepsilon(\frac{\omega}{c})^2 - k_x^2)H_y = 0, \tag{5.17}$$

where $\frac{\partial}{\partial t} = -i\omega$ in the frequency domain. The electric field components can be derived as:

$$\mathbf{E}_z = -\frac{k_x}{\omega\varepsilon_0\varepsilon}H_y, \tag{5.18}$$

$$\mathbf{E}_x = -\frac{i}{\omega\varepsilon_0\varepsilon}\frac{\partial H_y}{\partial z}. \tag{5.19}$$

The wave equation and the nonzero magnetic field components for TE mode can also be obtained as:

$$\frac{\partial^2 E_y}{\partial z^2} + (\varepsilon k_0^2 - k_x^2)E_y = 0, \tag{5.20}$$

$$\mathbf{H}_z = \frac{k_x}{\omega\mu_0}E_y, \tag{5.21}$$

$$\mathbf{H}_x = \frac{i}{\omega\mu_0}\frac{\partial E_y}{\partial z}. \tag{5.22}$$

5.4.3 Dispersion relation of surface plasmon polaritons at a single interface

In order to characterize SPPs, let's consider a system consisting of a flat plane interface at $z = 0$ that separates two materials: one with a real dielectric constant ε_1 which occupies the region $z < 0$, and one with a real dielectric constant ε_2 which occupies the region $z > 0$. A schematic representation of this system is shown in Figure 5.7 (b). In this configuration, x-z plane is the plane of incidence, and k_1 and k_2 are the transverse components of the wave vector in materials 1 and 2, respectively. Using equations 5.17 - 5.19, the **E** and **H** field components can be derived as:

$$z < 0 \begin{cases} \mathbf{H}_y(z) = Ae^{(ik_x x + k_1 z)} \\ \mathbf{E}_z(z) = -A\frac{k_x}{\omega\varepsilon_0\varepsilon_1}e^{(ik_x x + k_1 z)} \\ \mathbf{E}_x(z) = -A\frac{ik_1}{\omega\varepsilon_0\varepsilon_1}e^{(ik_x x + k_1 z)} \end{cases} \tag{5.23}$$

and,

$$z > 0 \begin{cases} \mathbf{H}_y(z) = Be^{(ik_x x - k_2 z)} \\ \mathbf{E}_z(z) = -B\frac{k_x}{\omega\varepsilon_0\varepsilon_2}e^{(ik_x x - k_2 z)} \\ \mathbf{E}_x(z) = B\frac{ik_2}{\omega\varepsilon_0\varepsilon_2}e^{(ik_x x - k_2 z)} \end{cases} \tag{5.24}$$

Using Maxwell's equations, the boundary conditions for the electromagnetic waves at the interface ($z = 0$) can be written as:

$$\varepsilon_1 E_z(z = 0^+) = \varepsilon_2 E_z(z = 0^-), \tag{5.25}$$

$$H_y(z = 0^+) = H_y(z = 0^-), \tag{5.26}$$

$$E_x(z = 0^+) = E_x(z = 0^-). \tag{5.27}$$

The above equations simply say that the normal component of the electric displacement vector, the transverse component of the magnetic field, and the tangential component of the electric field must be continuous across the interface between the two media. Applying the first condition at the boundary results in A = B. The second condition also gives us a similar result.

However, the continuity of the tangential electric field results in the following relation:

$$\frac{k_1}{\varepsilon_1} + \frac{k_2}{\varepsilon_2} = 0. \tag{5.28}$$

In addition, using equation 5.17, we have:

$$k_x^2 - k_i^2 = \varepsilon_i (\frac{\omega}{c})^2. \tag{5.29}$$

Now, by combining equations 5.28 and 5.29, the SPP dispersion relation at the interface can be obtained as:

$$k_x = \frac{\omega}{c} \sqrt{\frac{\varepsilon_1 \varepsilon_2}{\varepsilon_1 + \varepsilon_2}}. \tag{5.30}$$

Here, the imaginary component of the wavevector along the perpendicular direction is responsible for the SPPs propagation. Therefore, in order to have an imaginary k_x, $\varepsilon_1 < -\varepsilon_2$ in the above equation, meaning ε_1 and ε_2 must be opposite in sign. In other words, surface waves are only supported at the interface between two materials where the real parts of their dielectric functions have opposite signs across the interface.

Now, let's consider a TE polarized light. In this case, the **E** and **H** field components can be derived as:

$$z<0\begin{cases}\mathbf{E}_y(z)=Ae^{(ik_x x+k_1 z)}\\ \mathbf{H}_z(z)=A\frac{k_x}{\omega\mu_0}e^{(ik_x x+k_1 z)}\\ \mathbf{H}_x(z)=A\frac{ik_1}{\omega\mu_0}e^{(ik_x x+k_1 z)}\end{cases} \tag{5.31}$$

and,

$$z>0\begin{cases}\mathbf{E}_y(z)=Be^{(ik_x x-k_2 z)}\\ \mathbf{H}_z(z)=B\frac{k_x}{\omega\mu_0}e^{(ik_x x-k_2 z)}\\ \mathbf{H}_x(z)=-B\frac{ik_2}{\omega\mu_0}e^{(ik_x x-k_2 z)}\end{cases} \tag{5.32}$$

Applying boundary conditions to the interface results in:

$$A(k_1+k_2)=0. \tag{5.33}$$

As explained earlier, both Re[k_2] >0 and Re[k_1] >0 . Therefore, A must be zero in the above equation, which results in A = B = 0. This implies that SPPs are not possible with TE polarization, and they only exist for TM surface modes.

We note that we only considered a special case with a single interface between two non-magnetic materials. In fact, TE mode is possible in materials with large negative permeabilities [89, 90], or in heterostructures with multiple thin layers of dielectrics [91, 92]. However, these cases will not be discussed here. Therefore, we conclude that SPPs occur at a simple planar interface between two materials having dielectric functions with opposite signs, and only in the TM polarization mode. Because the dielectric function of a conductor is real and negative (in the lossless approximation), and the dielectric function of a dielectric is real and positive, ε_1 and ε_2 can represent a conductor and a dielectric medium, respectively.

Lastly, let's consider the dispersion relation in real conductors. If we assume the media 1 and 2 in Figure 5.7 (b) are lossless metal and air ($\varepsilon = 1$), respectively, the propagation constant can be obtained as $k_x = \frac{\omega\sqrt{\varepsilon_{metal}}}{c}$. Note that we assumed an ideal metal here where the imaginary part of the ε_{metal} is zero. In this case, a forbidden region forms in the dispersion curve where no propagation is allowed. However, both the dielectric function and the propagation constant are complex in real metals. Therefore, it can be seen that the forbidden region entirely vanishes, and the wave vector of the SPPs approaches a maximum but finite value at the surface plasmon frequency of the system. An example of the dispersion curve at the silver/silica and silver/air interface is shown in Figure 5.8.

5.5 Chapter summary

This chapter began with a brief overview of the properties of the semiconductor materials and QDs. We also discussed the GaAs properties, the MBE growth method, and the structure of our particular sample. Afterward, we talked about the sample fabrication process used to embed the silver nanostructures in our sample. All these steps are performed in a cleanroom in the SmartState Center for Experimental Nanoscale Physics at the University of South Carolina.

In the last section, we discussed both Lorentz and Drude models to better understand the behavior of the delocalized electrons in conductors and semiconductors. By exploiting Maxwell's equations and applying appropriate boundary conditions, we then obtained the SPP dispersion at a single interface between two media for both TE and TM polarizations. We also showed that the SPP waves propagating at the interface between two non-magnetic materials occur only in the TM polarization mode.

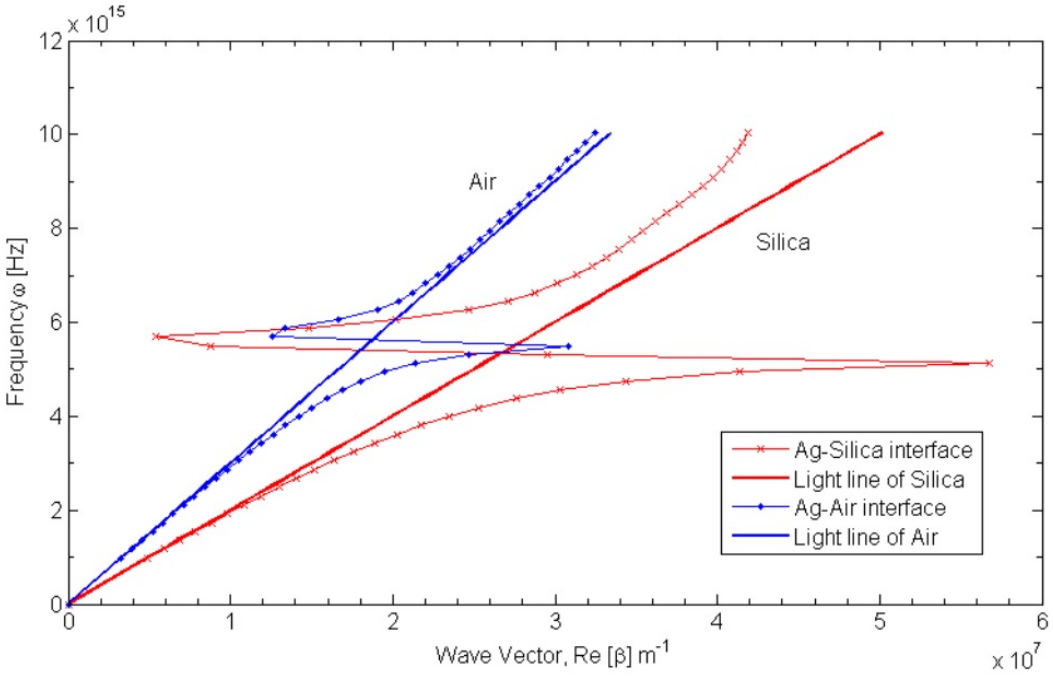

Figure 5.8 An example of the dispersion curve of SPP confined at the silver/silica and silver/air interface and their corresponding light lines are shown in red and blue, respectively. Source: [93].

Chapter 6

Photoluminescence characterization of InAs/GaAs quantum dots

In this chapter, we will investigate the photoluminescence (PL) characteristics of the hybrid plasmonic/QD sample. To achieve this goal, we will excite the bound electrons using two different energies, one above and one below the low-temperature band gap of GaAs. Photons with energies below the GaAs band gap excite electrons into the conduction band. This creates holes in the valence band and, therefore, excitons, as explained earlier. On the other hand, photons with energies above the GaAs band gap excite a large number of free carriers into the conduction band. Although these electrons still relax to the lower states and form excitons, the extra carriers in the plasma lead to complex interactions between the electrons and holes. Consequently, we will not be able to analyze the microscopic dynamics of this system. However, we can distinguish the transitions between different exciton charge species in a single QD as a function of the power and voltage.

6.1 Photoluminescence optical setup

In the above GaAs band gap excitation measurements, a fiber-coupled CW laser (Coherent) is used as the excitation source with a central wavelength at 532 nm. The incident laser light is first directed through an optical short-pass filter (Thorlabs, FESH0900) to eliminate the wavelengths longer than 900 nm, the range of the QD emission. Afterward, the light is transmitted through two linear polarizing films

(Thorlabs, LPVIS) with a half-wave plate (Thorlabs, WPH05M-532) between them. The combination of these three optical components is used to control the power and the polarization angle of the incident laser light. When the polarization and the power are set, the light is focused onto the sample using an NIR microscope objective (Mitutoyo infinity corrected). This lens allows us to focus the light to a spot size of ~ 1 micron. In order to be able to focus the light normal to the sample and move it over different regions while maintaining the focus, the objective lens is mounted on an XYZ translation stage consisting of three mirrors. These mirrors are mounted at 45° with respect to each other.

This measurement is performed in a reflection geometry where the angle between the incident and the reflected beams is 0°. Therefore, the generated signal and the reflected laser light are both collected using the same lens. Afterward, a non-polarizing beamsplitter (Thorlabs, CM05-BS017, 700-1100 nm) is used to transmit the generated light through a long-pass filter (FELH0900). This filter is used to eliminate any remaining laser light or any light of wavelengths below 900 nm. In addition, using a flip-mirror after the beamsplitter, the light can be sent to a charge-coupled device camera.

Following the long-pass filter is a lens that focuses the light into a spectrometer (HORIBA, iHR550). The spectrometer is attached to a CCD camera (Andor Newtons) cooled to -70 °C. It resolves the signal using the 1200 grooves/mm grating. The opening slit width is also set at 0.1 (angular units). The collected signal by the spectrometer is recorded by a computer using the LabVIEW program. Moreover, all data are measured using the full vertical binning mode with the integration time of 5 seconds, which is much longer than the recombination lifetime of our QDs (on the order of 1 ns). A schematic of the experimental setup is shown in Figure 6.1.

A similar optical setup is used for the below GaAs band gap excitation, except for the change in the wavelength-dependent optical components. For example, the green

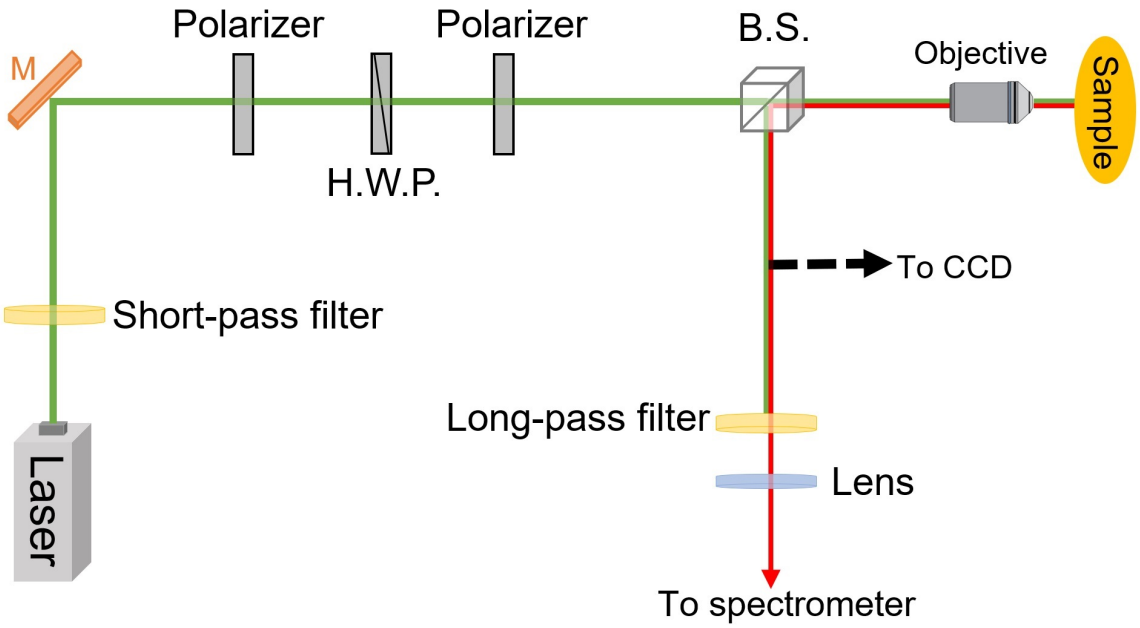

Figure 6.1 The experimental setup with a reflection geometry used for the PL characterization of InAs/GaAs QDs. The incident laser light is first passed through a short-pass filter. Then a combination of two polarizers and a half-wave plate (H.W.P.) is used to control the intensity and polarization of the laser beam. Afterward, an NIR microscope objective (Mitutoyo infinity corrected) with magnification 50× and focal length 200 mm is used to focus the light onto the sample. The sample is mounted inside the specimen chamber of a Cryostatation and stabilized at 4 K. The generated signal is collected using the same lens, and then transmitted through a non-polarizing beamsplitter (B.S.) and a long-pass filter. The sample can also be monitored using a charge-coupled device camera (CCD) by placing a flip-mirror in the path. Afterward, the light is focused into a spectrometer to resolve the signal.

CW laser is replaced with a fiber-coupled NIR diode laser with a central wavelength at 880 nm (Thorlabs, CLD1010). In addition, the linear polarizing films and the half-wave plate are replaced with a Glan-Taylor polarizer (Thorlabs, GT10-B) and a 915 nm half-wave plate (Thorlabs, WPH05M-915). In this case, the spot size is slightly larger than the size of the green light. However, it is still focused on the order of $\sim$ 1 micron using the same microscope objective.

Lastly in this section, let's consider the effect of the incident polarization on the PL signal collected from QDs. As mentioned in section 5.4, the polarization can be either in TE or TM mode. In addition, it can be seen in Figure 5.3 that the studied silver structures in our sample have a long rectangular shape. Accordingly, the electric field lines of the TE mode are along the long axis of these structures, and therefore perpendicular to their short axis. As a result, they will diffract away from the silver structures. Consequently, there is no coupling between the light and the metal surface, meaning the TE polarization will not affect the QD PL emission (Figure 6.2).

The situation is totally different for the TM polarization. In this mode, the electric field lines are parallel to the short axis of the structures, and therefore perpendicular to their long axis. As a result, the SPP waves propagate along the surface of silver structures, meaning the light can couple to the QDs in this configuration. This results in forming excitons inside the dots. The coupling between the excitons and the SPP waves will affect the PL emission of the QDs that are closer to the plasmonic structures. This polarization-dependent property of the PL signal will be discussed in more detail in the following sections.

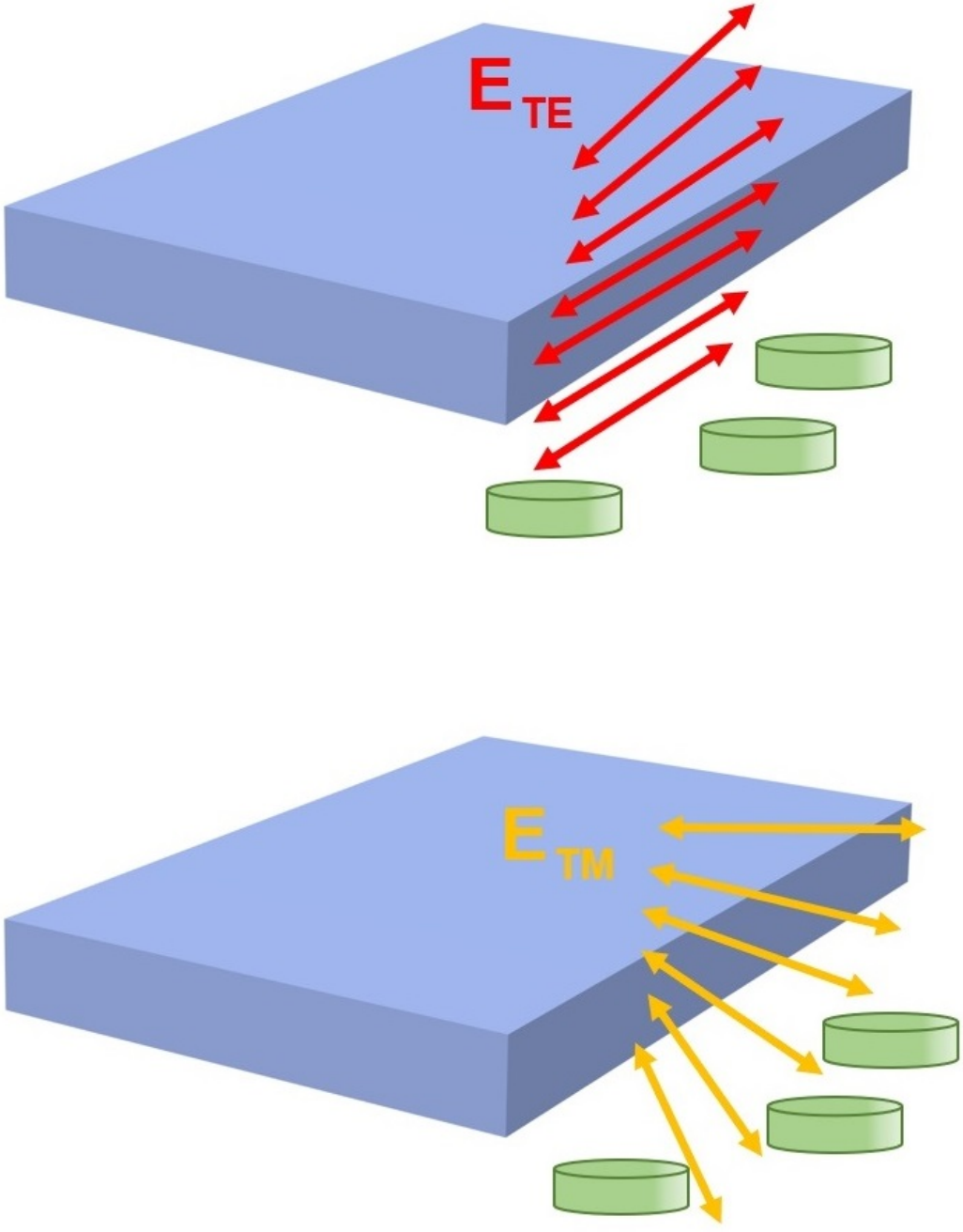

Figure 6.2 Effects of the incident TE and TM polarizations on silver structures and QDs.

6.2 Above GaAs band gap excitation measurements

The plasmonic/QD device is first characterized with a 532 nm CW laser using the optical setup described in the previous section. Using this green laser, we can easily distinguish the incident light from the QD emitted signal, which is in the near-infrared region. Here, the energy of the incident photons is about 2.33 eV, which is above the band gap of the GaAs at 4 K, $E_g = 1.519$ eV.

In this case, the electrons are excited into the conduction band, where they are not confined by the QDs anymore. In fact, the light can be absorbed into the GaAs capping layer, which results in injecting a large number of carriers into the conduction band. Afterward, the excited electrons first relax non-radiatively and then fall back to the lower energy states, where they again become confined by the dots. Although they still form excitons by coupling to the other trapped holes there, the large number of carriers in the conduction band lead to complex interactions between the electrons and holes. Therefore, the microscopic dynamics of this system cannot be understood easily and will not be discussed in this work. However, we are able to observe the transitions between different exciton species in a single QD.

Specifically, we will first study the discrete QD emission peaks in the presence and absence of the silver structures for TE and TM excitation polarizations, while both voltage and power are fixed. Then, we will investigate the transitions between exciton charge states as a function of the power and external bias applied across the sample.

6.2.1 Polarization-dependent effects in the plasmonic/QD device

In order to confirm that the disk-shaped QDs do not exhibit any polarization-dependent behavior, the PL signal is first measured for both TE and TM polarizations while the dots are excited away from the silver. Afterward, a similar measurement is performed in the presence of the silver slabs to see the effect of the SPP waves propagating along

the plasmonic structures. The resulting PL data as a function of the emission energy can be seen in Figure 6.3(a), when QDs are excited away from the silver structures, and in Figure 6.3(b), when QDs are excited over the structures. In these measurements, the incident power and the applied voltage are fixed at 40 μW and 0.9 V, respectively. Clear discrete emission peaks from single QDs are observed in both Figures 6.3(a) and (b). Although the shapes of the emission peaks are slightly different in these two graphs, no drastic difference between the overall number of counts is observed. This behavior is likely due to the thickness of the GaAs capping layer in our sample. As mentioned earlier, this thickness is only $\sim$ 150 nm in the absence of any etched structures, meaning there is $\sim$ 40 nm of GaAs below the 60 nm of silver slabs. However, previous studies performed on a similar sample with a capping layer of 280 nm and 100 nm of GaAs below the silver structures showed a noticeable difference between the QD emission peaks in these two cases. It was observed that the peaks were drastically narrower when QDs excited over the silver compared to the peaks when they were far away from the metal surface [94].

The main difference between the two graphs in Figure 6.3 is the distinction between the TE and TM emission signals. When exciting QDs away from the silver, the overall PL spectra of both polarizations are nearly similar. In contrast, a clear polarization-dependent behavior can be seen in some of the emission peaks when exciting QDs on the silver. Because this effect is only observed in the presence of the silver slabs, it does not arise from the symmetry-breaking factor in the dots. In fact, the disk-shaped QDs exhibit no polarization-dependent behavior since they are axially symmetric.

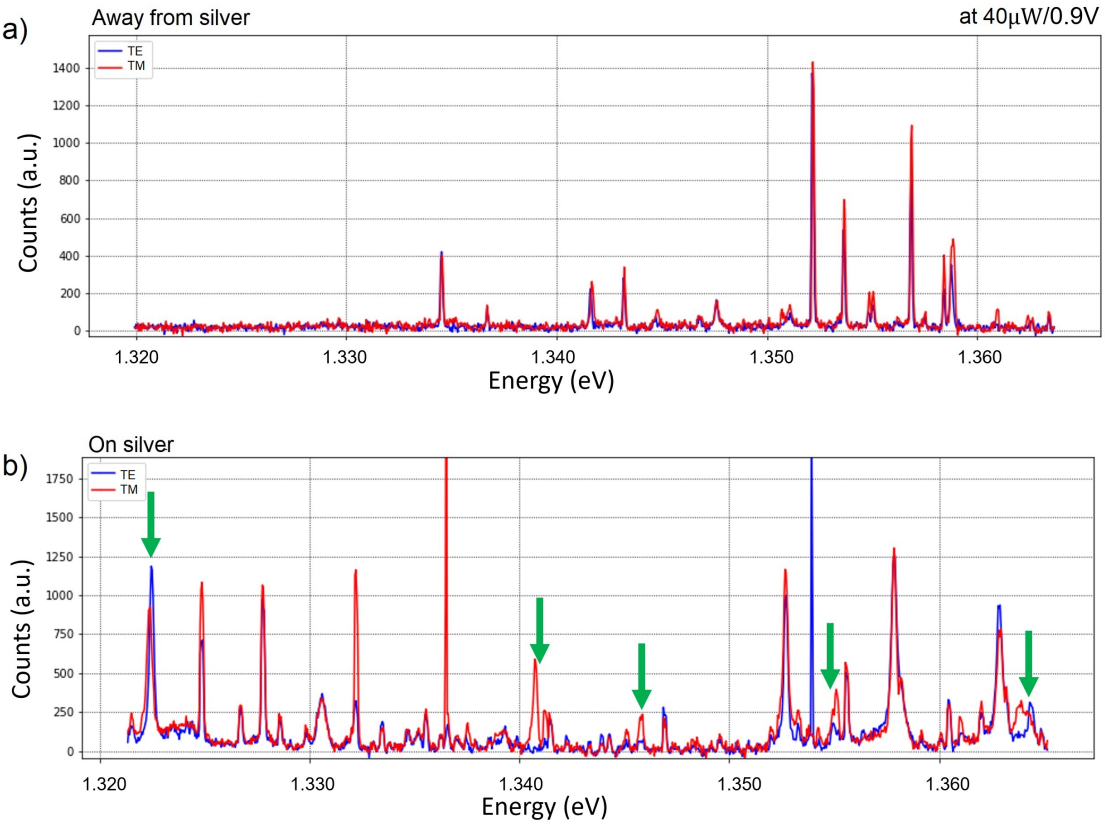

Figure 6.3 Measured PL data as a function of the emission energy when dots are excited (a) away, and (b) over the silver structures. The measurements are performed for both TE and TM polarizations which are shown in blue and red, respectively. No significant difference is observed in the PL signal collected away from silver. The polarization-dependent shifts in the PL energy of some of the emission peaks in the presence of silver are shown by green arrows.

Moreover, significant shifts in the PL energy of some of the peaks are observed in Figure 6.3(b), which are indicated by green arrows. However, no shifts in the emission peaks can be seen in Figure 6.3(a). The observed energy shifts indicate the transitions between exciton species inside a QD. This is because different charge species emit light at different wavelengths when the electron and the hole are recombined in the recombination process. We note that any splitting in the PL spectrum of a single QD is well below the resolution of our detection setup, and therefore cannot be detected. Consequently, the observed behavior is indeed due to the coupling between the SPP waves and the excitons, and specifically by the light with TM polarization.

6.2.2 Voltage- and power-dependent effects in the plasmonic/QD device

Here, the PL signal is measured from the QDs over the silver structures for both TE and TM polarizations, while an electric field is applied through the sample. As explained in the fabrication process, the silver paste connected to a thin layer of In and the N+ GaAs buffer layer on the bottom surface of the sample, and a thin layer of Cr on the top surface allows us to apply a bias across the sample.

The measured PL signals as a function of the emitted photon energy and the external voltage are shown by color maps in Figure 6.4. The photon energy and the applied voltage are shown on the horizontal- and the vertical-axes, respectively. Therefore, each row of pixels can be considered as the collected PL data at a fixed voltage, e.g. similar to Figure 6.3. And each column of pixels indicates an emission peak, where its intensity is shown by a particular color. The bright pixels represent a greater number of counts, while the black pixels represent the background with a little signal. These measurements are done for two different excitation powers, 30 μW and 35 μW, as shown in Figures 6.4(a) and 6.4(b), respectively. These power values are measured after the microscope objective in the setup. The data from TM polarization is shown in the left panel, whereas the right panel shows the data from

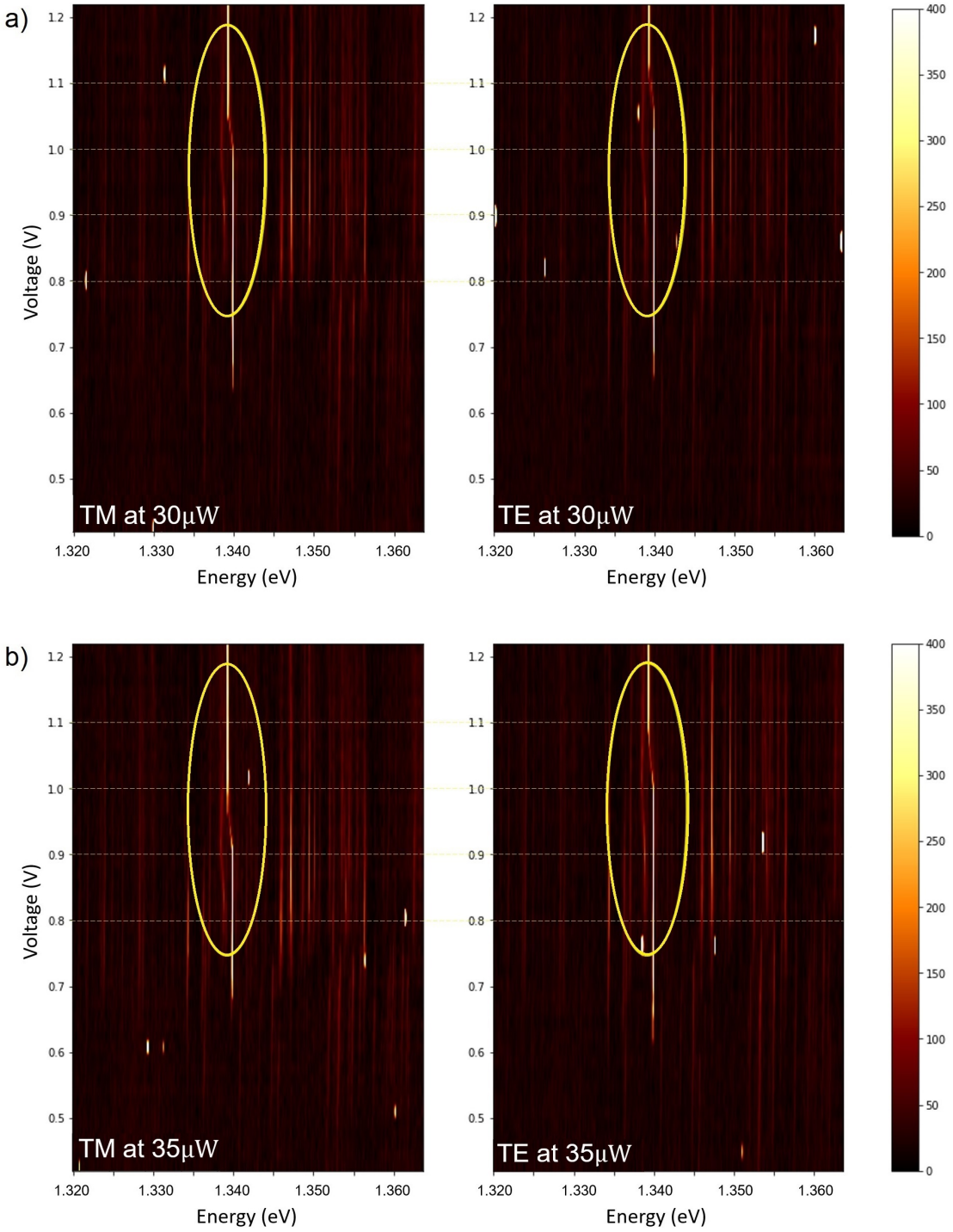

Figure 6.4 Bias-dependent PL maps on the silver at (a) 30 μW, and (b) 35 μW. The area indicated by yellow ovals illustrates a specific transition between two exciton species within a single QD. This transition is observed at a lower voltage for the higher power. In addition, it is occurred at a higher voltage for the TE mode compared to the TM mode, at a fixed power.

the TE polarization mode. The first observed feature is the emission lines that are not entirely aligned with the vertical-axis. Specifically, the indicated area in the yellow ovals shows a specific emission peak that shifts slightly towards higher energy values over a range of voltages. As mentioned earlier, these energy shifts are due to the changes in the exciton binding energy in a single QD.

Another significant observed feature in these graphs is the required voltage for the exciton charge species transitions. Although all these transitions occur in the positive bias range, the required voltage is dependent on the incident polarization at a fixed power. At 30 μW, the transition is seen at $\sim$ 1.03 V for TM polarization, whereas it occurs at $\sim$ 1.1 V for TE polarization (Figure 6.4(a)). Interestingly, the required voltage for this transition is totally different when the excitation power is set at 35 μW, as shown in Figure 6.4(b). The energy shift is observed at a bias of $\sim$ 0.95 V for TM polarization, and at a bias of $\sim$ 1.05 V for TE polarization. These results imply that the required voltage for the charge species transitions is also dependent on the incident power at a fixed polarization. It can be seen that the transition is shifted downward for each polarization as the power is increased, meaning lower voltages are required to force the transitions to occur when the power is larger. As mentioned before, different exciton species have different emission energies meaning the observed transitions are associated with a particular exciton in a particular QD. In other words, for a different exciton, these shifts occur at different voltages and powers depending upon the QD's shape, size, and the confining potential.

We also note that the observed emission lines correspond to all the excited QDs within the laser beam spot with a Gaussian profile. Therefore, other lines in Figure 6.4 represent the emission lines of the dots that are further away from the silver-GaAs interface. These lines are either perfectly aligned with the vertical-axis or do not exhibit any polarization-dependent behavior.

Lastly, in order to see how the voltage-dependent maps look like in the absence of the plasmonic structures, a similar measurement is performed on the QDs on and away from the silver slabs at a fixed power and at two new regions of the sample (Figure 6.5). The incident power is set at 40 μW in these measurements. It can be seen that the emission lines are perfectly aligned with the vertical-axis with no transitions for the measured data away from silver in Figure 6.5(a). In contrast, some of the vertical lines are drifted in Figure 6.5(b), similar to Figure 6.4. Consequently, our results confirm that the observed behavior is indeed due to the effect of the SPP field in the presence of the silver structures, and the shifts are from two different exciton species within a QD.

6.3 Below GaAs band gap excitation measurements

In this section, the sample is characterized using an NIR diode laser with a central wavelength at 880 nm. Here, the energy of the incident photons is about 1.41 eV, which is below the band gap of the GaAs at 4 K. Consequently, there are fewer carriers into the GaAs conduction band, meaning no power-dependent effect will be seen in the exciton transitions. Therefore, only the polarization-dependent effect is investigated in this case.

Similar to the above band gap case, the PL signal is collected from QDs for both TE and TM excitation polarizations on and away from the silver structures. The resulting PL data can be seen in Figure 6.6(a), when QDs are excited away from the silver, and in Figure 6.6(b), when QDs are excited on the silver. Clear discrete peaks from single dots are still observed in both cases. However, the emission peaks look narrower compared to the case of the above band gap measurements since now there are fewer carriers in the conduction band.

In addition, the overal shape of the PL signal looks different in this case. A likely reason is that the 880 nm diode laser used here excites both the QDs and the wetting

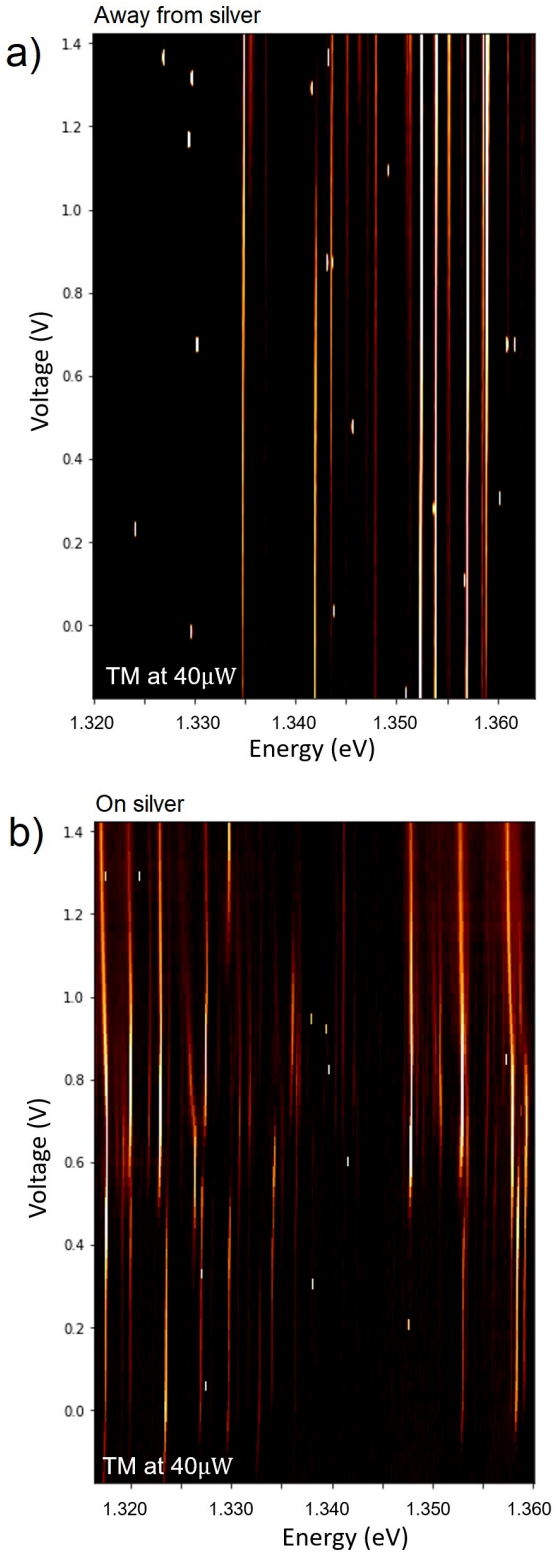

Figure 6.5 Two examples of the bias-dependent PL maps (a) away from silver, where the emission lines are perfectly aligned with the vertical-axis, (b) on the silver, where some of the lines are drifted.

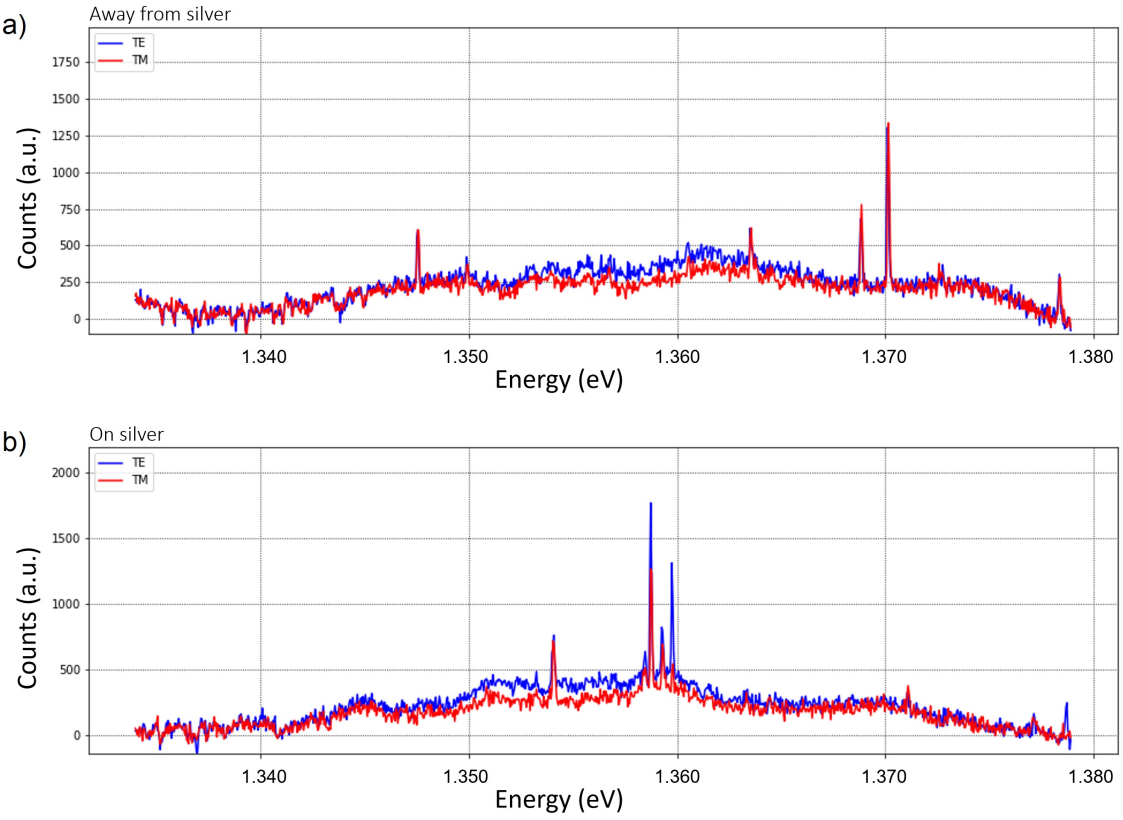

Figure 6.6 880 nm PL data as a function of the emission energy when QDs are excited (a) away, and (b) on the silver structures. The measurements are performed for both TE and TM polarizations which are shown in blue and red, respectively. A polarization-dependent effect can be seen in the PL energy of the emission peaks in the presence of silver.

layer below them. As a result, the wetting layer, which is InAs in our sample, produces a strong background noise. Although this background can affect the resolution of our data, its shape and level are similar for both polarizations and in both on and away from silver cases. Additionally, this broadband background signal can be easily distinguished from our narrow QD emission peaks. Moreover, only the tail of the wetting layer is observed in our PL data since most of it is blocked by the long-pass filter placed before the detector. In the sample studied previously, this background level was easily subtracted by an exponential fit.

Another possible reason for the observed noise can be the chosen energy range, which is very close to the blocked region by the long-pass filter. However, most of the emission peaks are observed in this region. The thickness of the GaAs capping layer of our sample can also be a possible reason for the observed effect. As mentioned earlier, this layer is $\sim$ 130 nm thinner than the sample used in the previous studies. The GaAs layer below the silver structures is also $\sim$ 60 nm thinner. Therefore, it is possible that the strong 880 nm excitation field affects the QDs in a different way in this sample. These reasons can also explain the significant reduction in the number of the observed peaks in Figure 6.6. An example of the PL data collected from the sample studied previously is illustrated in Figure 6.7.

One observed feature in Figure 6.6 is the polarization-dependent behavior in the PL data. For the data measured away from the silver, no drastic difference is observed between the overall number of counts of the emission peaks in TE and TM polarizations. For the data measured on silver, the TE excitation peaks exhibit a stronger intensity than the TM peaks, as illustrated in Figure 6.6(b). This is unlike the results observed in the previous section. This behavior can be explained by the interaction between the SPP field and the electric mesoscopic moment of the QDs [95]. Considering the dipole coupling terms, this interaction can result in either constructive or destructive interferences. The first case leads to enhancement of the radiative decay

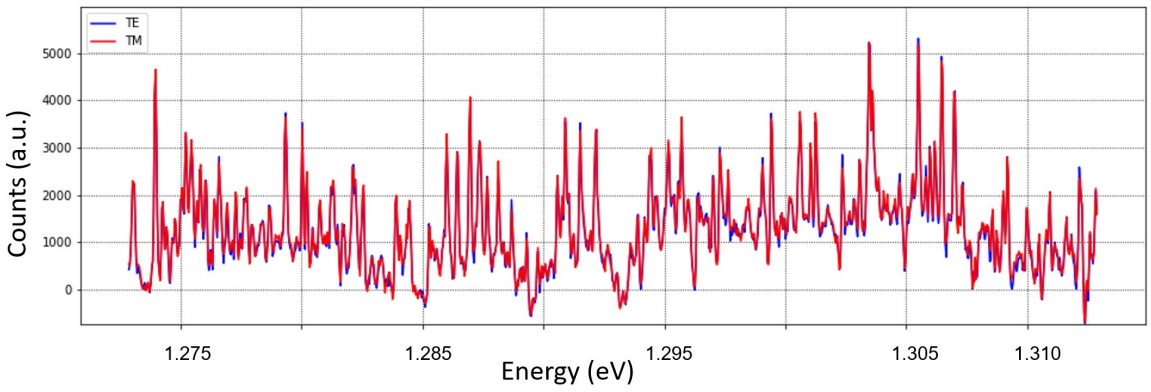

Figure 6.7 An example of the 880 nm PL data as a function of the emission energy from a different QD sample with a thicker capping layer.

rate, whereas the latter interaction suppresses it. As a result, we can say that a destructive interference resulted in the lower signal intensity for the TM polarization in our system. We also observed that many of the emission peaks are slightly shifted in the presence of the silver slabs. An example of the observed shift is illustrated in Figure 6.8. It can be seen that these shifts are very small, and therefore cannot be detected well because of the resolution of our optical setup. Since this effect is consistent, it cannot be the result of optical artifacts. It also cannot be due to a change in the intensity of the excitation field since it does not alter the internal energy of the excitons in a QD. In addition, this behavior is observed only in the presence of the silver-GaAs interface. Consequently, these shifts are likely due to the effect of the SPP field propagating on the plasmonic structures in the TM mode. However, we note that more investigations are needed to truly validate this observed behavior.

6.4 Chapter summary

In this chapter, we first described the optical setup used to collect the PL signal from QDs. We then investigated the PL characteristics of the hybrid plasmonic/QD sample in two cases. In the case of the above GaAs band gap, we observed a significant polarization-dependent effect in the PL signal when QDs were excited over the silver structures. This effect was not observed far away from silver. Then, we discussed how the transitions between the charge species of excitons within a single dot were affected by an applied voltage and power. We observed this transition shifted downward in the TM mode, compared to the TE mode at a fixed power. We also observed another downward shift for each polarization direction as the power was increased. In the case of the below GaAs band gap, we observed discrete emission peaks with a polarization-dependent effect in the PL signal in the presence of silver. However, the overall intensity of the peaks in the PL signal was lower for TM polarization compared to the TE polarization. This effect can be due to the interaction between

the SPP field and the electric mesoscopic moment of the dots. Further studies are required to truly confirm this effect.

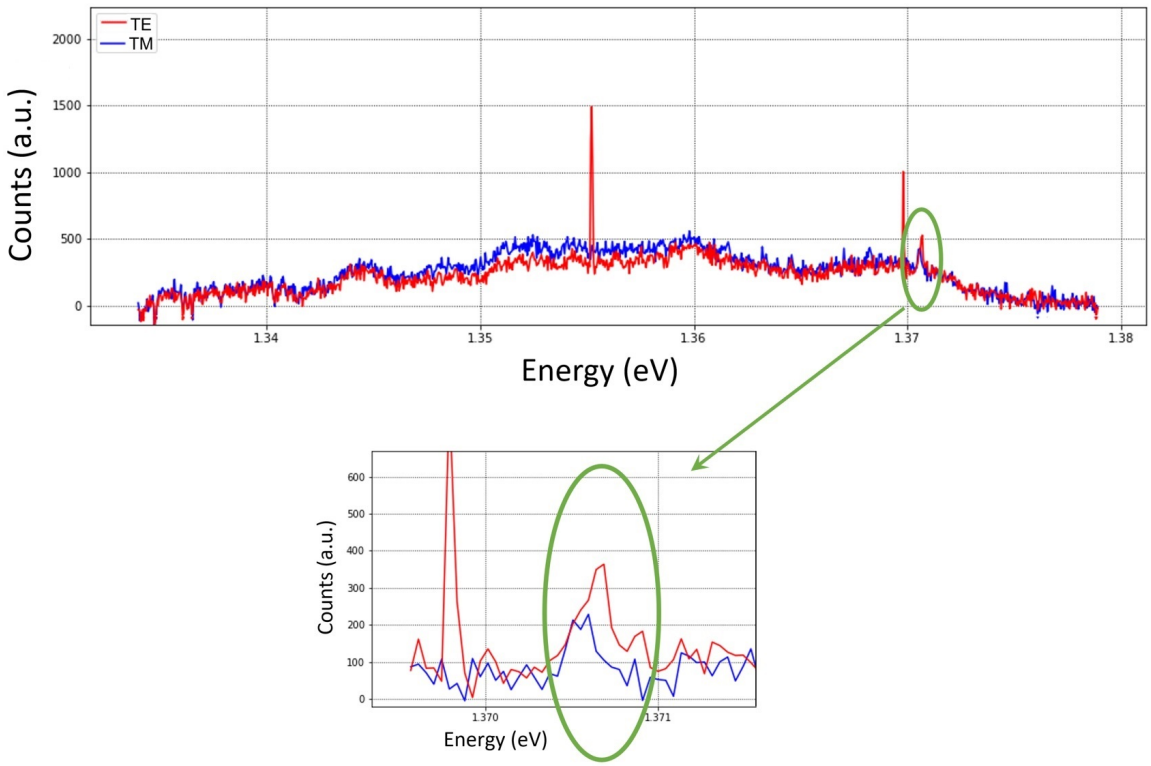

Figure 6.8 An example of the 880 nm PL data taken on the silver. The zoom-in peak in the inset indicates a slight shift in the emission energy. This behavior is observed in several peaks.

Chapter 7

Summary and future directions

In this thesis, we optically investigated two nanoscale hybrid systems. The outcome of this research will help guide future investigations to better evaluate similar hybrid nanoscale systems and enable the eventual implementation of the promising materials used here into practical devices.

The first hybrid system studied in this work consists of composite multiferroic BTO/CFO nanofibers with a Janus structure. In order to investigate this system, we used the optical SHG technique to monitor the changes in the ferroelectric BTO constituent while modifying the magnetization in the ferrimagnetic CFO. We observed robust evidence of the magnetoelectric coupling in the system by the application of a magnetic field alone at room temperature. We showed that this behavior only happens in multiferroic composites and is not intrinsic to either of the individual constituents. Using SHG corroborated by XRD, we also confirmed that the observed changes in the polarization-resolved SHG are indeed caused by the magnetoelectric coupling in the BTO and CFO lattice constants.

The SHG signal in this hybrid system can be affected by several factors. For example, previous studies have shown that the transferred strain can be reduced by cracks, impurity, and residual strain at the interface [96, 97]. Therefore, not having a homogeneous and coherent interface between the ferroic constituents can affect the measurement values. This is why the same absolute behaviors are not repeatable across different fiber ensembles. Consequently, enhancing the shared interface between the two ferroic phases is a major step that needs to be done in the future.

Another future crucial step is adding a detector along the z-axis in the SHG setup. This additional detection plane can provide 3D information on the BTO dipole orientations. Moreover, more precise and systematic SHG studies corroborated by XRD can be done in order to track the evolution of the observed field-dependent strain-mediated effect and also obtain quantitative information in this nanofiber system. In addition, two bar magnets with well-defined field lines can be used to better clarify the CFO behavior. Another future direction can be using the Piezoresponse force microscopy (PFM) technique to monitor the magnetic field-dependent changes in the ferroelectric BTO domains [7, 8].

The second nanoscale hybrid system studied here consists of self-assembled semiconductor InAs/GaAs quantum dots and SPP supporting plasmonic structures. To investigate this coupled system, the incident photons were excited with two different energies: one above the encapsulating GaAs band gap, and one below it. In the case of the above GaAs band gap, the QDs were excited on and away from the silver structures. We observed a polarization-dependent effect in the PL signal induced by the SPP fields, and only with a nearby silver. Then, we were able to detect the transitions between the exciton charge species within a single QD by applying a voltage across the fabricated sample. In the case of below the GaAs band gap excitation, we observed a similar polarization-dependent effect in the PL signal when QDs were excited over the silver slabs. However, we observed a reduction in the intensity of the TM peaks, unlike what we observed in the above excitation case. We also found that some QD emission peaks were slightly shifted in the PL data. However, a more detailed study is needed to further confirm these behaviors.

The most challenging step in studying this hybrid system was the fabrication process. In fact, the main focus of this work was finding a repeatable and promising fabrication recipe in order to achieve the desired plasmonic structures. The lack of proper equipment in some fabrication steps delayed this project, and therefore

performing more data collection was beyond the time constraints of this work. As a result, the first future goal can be either taking more data using the same sample, or fabricating a new sample. Here, the presented data are collected from a piece of the original sample with little embedded QDs. Therefore, using a sample piece with more QDs can be helpful to observe stronger effects. The self-assembled dots are also distributed randomly on top of the wetting layer in this sample. Thus, using a different technique to grow the QDs at specific locations can indeed introduce new ideas, such as studying the coupling between two specific QDs and using SPP fields to mediate an excited exciton from one to another [98]. Further work can also be done using plasmonic structures with different geometries, such as different shapes with both sharp and round corners, or different metal/insulator combinations to see how they change the SPP fields at the interface. Lastly, another future direction can be performing the more complex time-domain studies. For example, the wave pulse shaping technique can be used to investigate the exciton recombination lifetime in this hybrid system [99, 100].

Bibliography

[1] Ce-Wen Nan. "Magnetoelectric effect in composites of piezoelectric and piezomagnetic phases". In: *Physical Review B* 50.9 (1994), p. 6082.

[2] Ce-Wen Nan et al. "Multiferroic magnetoelectric composites: Historical perspective, status, and future directions". In: *Journal of applied physics* 103.3 (2008), p. 1.

[3] Gustau Catalan and James F Scott. "Physics and applications of bismuth ferrite". In: *Advanced materials* 21.24 (2009), pp. 2463–2485.

[4] Manfred Fiebig. "Revival of the magnetoelectric effect". In: *Journal of physics D: applied physics* 38.8 (2005), R123.

[5] Jing Ma et al. "Recent progress in multiferroic magnetoelectric composites: from bulk to thin films". In: *Advanced materials* 23.9 (2011), pp. 1062–1087.

[6] CL Zhang et al. "The magnetoelectric effects in multiferroic composite nanofibers". In: *Applied Physics Letters* 94.10 (2009), p. 102907.

[7] Shuhong Xie et al. "Multiferroic CoFe 2 O 4–Pb (Zr 0.52 Ti 0.48) O 3 core-shell nanofibers and their magnetoelectric coupling". In: *Nanoscale* 3.8 (2011), pp. 3152–3158.

[8] Bi Fu et al. "Magnetoelectric coupling in multiferroic BaTiO3-CoFe2O4 composite nanofibers via electrospinning". In: *EPL (Europhysics Letters)* 111.1 (2015), p. 17007.

[9] Matthew J Bauer et al. "Magnetic field sensors using arrays of electrospun magnetoelectric Janus nanowires". In: *Microsystems & nanoengineering* 4.1 (2018), pp. 1–12.

[10] Ce-Wen Nan et al. "Magnetic-field-induced electric polarization in multiferroic nanostructures". In: *Physical review letters* 94.19 (2005), p. 197203.

[11] Dwight Viehland et al. "Tutorial: Product properties in multiferroic nanocomposites". In: *Journal of Applied Physics* 124.6 (2018), p. 061101.

[12] Ying-Hao Chu et al. “Electric-field control of local ferromagnetism using a magnetoelectric multiferroic”. In: *Nature materials* 7.6 (2008), pp. 478–482.

[13] Ramaroorthy Ramesh and Nicola A Spaldin. “Multiferroics: progress and prospects in thin films”. In: *Nanoscience And Technology: A Collection of Reviews from Nature Journals* (2010), pp. 20–28.

[14] LW Martin, Y-H Chu, and RJMS Ramesh. “Advances in the growth and characterization of magnetic, ferroelectric, and multiferroic oxide thin films”. In: *Materials Science and Engineering: R: Reports* 68.4-6 (2010), pp. 89–133.

[15] G Lawes and GJPDAP Srinivasan. “Introduction to magnetoelectric coupling and multiferroic films”. In: *Journal of Physics D: Applied Physics* 44.24 (2011), p. 243001.

[16] Michael Lorenz et al. “Multiferroic BaTiO3–BiFeO3 composite thin films and multilayers: strain engineering and magnetoelectric coupling”. In: *Journal of Physics D: Applied Physics* 47.13 (2014), p. 135303.

[17] Dhiren K Pradhan et al. “Exploring the magnetoelectric coupling at the composite interfaces of FE/FM/FE heterostructures”. In: *Scientific reports* 8.1 (2018), pp. 1–11.

[18] Md Rafiqul Islam et al. “Bi 0.9 Ho 0.1 FeO 3/TiO 2 Composite Thin Films: Synthesis and Study of Optical, Electrical and Magnetic Properties”. In: *Scientific reports* 9.1 (2019), pp. 1–13.

[19] Justin D Starr, Maeve AK Budi, and Jennifer S Andrew. “Processing-Property Relationships in Electrospun Janus-Type Biphasic Ceramic Nanofibers”. In: *Journal of the American Ceramic Society* 98.1 (2015), pp. 12–19.

[20] B Ravel et al. “Local structure and the phase transitions of BaTiO3”. In: *Ferroelectrics* 206.1 (1998), pp. 407–430.

[21] Millicent B Smith et al. “Crystal structure and the paraelectric-to-ferroelectric phase transition of nanoscale BaTiO3”. In: *Journal of the American Chemical Society* 130.22 (2008), pp. 6955–6963.

[22] Stephen John Moss and Anthony Ledwith. *Chemistry of the Semiconductor Industry*. Springer Science & Business Media, 1989.

[23] H-JJ Yeh and John S Smith. “Fluidic self-assembly for the integration of GaAs light-emitting diodes on Si substrates”. In: *IEEE Photonics technology letters* 6.6 (1994), pp. 706–708.

[24] L Harris et al. “Emission spectra and mode structure of InAs/GaAs self-organized quantum dot lasers”. In: *Applied physics letters* 73.7 (1998), pp. 969–971.

[25] E Dupont et al. “Efficient GaAs light-emitting diodes by photon recycling”. In: *Applied Physics Letters* 76.1 (2000), pp. 4–6.

[26] Ha Trong Than et al. “Design and Performance of a 600-W C-Band Amplifier Using Spatially Combined GaAs FETs for Satellite Communications”. In: *IEEE Journal Of Solid-State Circuits* 47.10 (2012), pp. 2309–2315.

[27] Jianping Wang et al. “Towards scalable entangled photon sources with self-assembled InAs/GaAs quantum dots”. In: *Physical review letters* 115.6 (2015), p. 067401.

[28] Sunghyun Moon et al. “Highly efficient single-junction GaAs thin-film solar cell on flexible substrate”. In: *Scientific reports* 6.1 (2016), pp. 1–6.

[29] Saraswati Behera et al. “Broadband, wide-angle antireflection in GaAs through surface nano-structuring for solar cell applications”. In: *Scientific reports* 10.1 (2020), pp. 1–10.

[30] AK Zvezdin et al. “Multiferroics: promising materials for microelectronics, spintronics, and sensor technique”. In: *Bulletin of the Russian Academy of Sciences: Physics* 71.11 (2007), pp. 1561–1562.

[31] Zygmunt Surowiak and Dariusz Bochenek. “Multiferroic materials for sensors, transducers and memory devices”. In: (2008).

[32] Swapna S Nair et al. “Lead free heterogeneous multilayers with giant magneto electric coupling for microelectronics/microelectromechanical systems applications”. In: *Journal of Applied Physics* 114.6 (2013), p. 064309.

[33] Tiberiu-Dan Onuta et al. “Energy harvesting properties of all-thin-film multiferroic cantilevers”. In: *Applied Physics Letters* 99.20 (2011), p. 203506.

[34] Tyrel Rupp et al. “Magnetoelectric transducer designs for use as wireless power receivers in wearable and implantable applications”. In: *Materials* 12.3 (2019), p. 512.

[35] Sugato Hajra et al. “Triboelectric nanogenerator using multiferroic materials: An approach for energy harvesting and self-powered magnetic field detection”. In: *Nano Energy* 85 (2021), p. 105964.

[36] Bernard Dennis Cullity and Chad D Graham. *Introduction to magnetic materials*. John Wiley & Sons, 2011.

[37] Abhijit Pramanick et al. "Domains, domain walls and defects in perovskite ferroelectric oxides: A review of present understanding and recent contributions". In: *Critical Reviews in Solid State and Materials Sciences* 37.4 (2012), pp. 243–275.

[38] Melvin M Vopson. "Fundamentals of multiferroic materials and their possible applications". In: *Critical Reviews in Solid State and Materials Sciences* 40.4 (2015), pp. 223–250.

[39] Haribabu Palneedi et al. "Status and perspectives of multiferroic magnetoelectric composite materials and applications". In: *Actuators*. Vol. 5. 1. Multidisciplinary Digital Publishing Institute. 2016, p. 9.

[40] Yen-Lin Huang et al. "Manipulating magnetoelectric energy landscape in multiferroics". In: *Nature communications* 11.1 (2020), pp. 1–8.

[41] Peggy Schoenherr et al. "Local electric-field control of multiferroic spin-spiral domains in TbMnO 3". In: *npj Quantum Materials* 5.1 (2020), pp. 1–7.

[42] Shivangi Tiwari and Satish Vitta. "Magnetoelectric and magnetodielectric coupling and microwave resonator characteristics of Ba 0.5 Sr 0.5 Nb 2 O 6/CoCr 0.4 Fe 1.6 O 4 multiferroic composite". In: *Scientific reports* 8.1 (2018), pp. 1–12.

[43] Yu Tang et al. "Anisotropy of Percolation Threshold of BaTiO 3-Ni 0.5 Zn 0.5 Fe 2 O 4 Composite Films". In: *Scientific reports* 9.1 (2019), pp. 1–7.

[44] JBNJ Wang et al. "Epitaxial BiFeO3 multiferroic thin film heterostructures". In: *science* 299.5613 (2003), pp. 1719–1722.

[45] JM Caicedo et al. "Magnetoelectric coefficient in Bi Fe O 3 compounds". In: *Journal of Applied Physics* 103.7 (2008), 07E306.

[46] Wilma Eerenstein, ND Mathur, and James F Scott. "Multiferroic and magnetoelectric materials". In: *nature* 442.7104 (2006), pp. 759–765.

[47] Tong Zhao et al. "Stress-induced enhancement of second-order nonlinear optical susceptibilities of barium titanate films". In: *Journal of Applied Physics* 87.10 (2000), pp. 7448–7451.

[48] Jiesu Wang et al. “Temperature-dependent phase transition in barium titanate crystals probed by second harmonic generation”. In: *Applied Physics Letters* 112.10 (2018), p. 102904.

[49] Mangamma Geramilla et al. “Nanoscale studies of magnetoelectric coupling in multiferroic BTO–CFO composite”. In: *Applied Physics A* 125.1 (2019), pp. 1–6.

[50] P Durga Prasad and J Hemalatha. “Enhanced magnetic properties of highly crystalline cobalt ferrite fibers and their application as gas sensors”. In: *Journal of magnetism and magnetic materials* 484 (2019), pp. 225–233.

[51] KC Verma, Navdeep Goyal, and RK Kotnala. “Tuning magnetism in 0.25 BaTiO3-0.75 CoFe2O4 hetero-nanostructure to control ferroelectric polarization”. In: *Physica B: Condensed Matter* 554 (2019), pp. 9–16.

[52] FA Yildirim et al. “Spin-cast composite gate insulation for low driving voltages and memory effect in organic field-effect transistors”. In: *Applied physics letters* 90.8 (2007), p. 083501.

[53] AN Morozovska et al. “Pyroelectric response of ferroelectric nanowires: Size effect and electric energy harvesting”. In: *Journal of Applied Physics* 108.4 (2010), p. 042009.

[54] Per Martin Rørvik, Tor Grande, and Mari-Ann Einarsrud. “One-dimensional nanostructures of ferroelectric perovskites”. In: *Advanced Materials* 23.35 (2011), pp. 4007–4034.

[55] Jinghui Gao et al. “Recent progress on BaTiO3-based piezoelectric ceramics for actuator applications”. In: *Actuators*. Vol. 6. 3. Multidisciplinary Digital Publishing Institute. 2017, p. 24.

[56] Matias Acosta et al. “BaTiO3-based piezoelectrics: Fundamentals, current status, and perspectives”. In: *Applied Physics Reviews* 4.4 (2017), p. 041305.

[57] Hisatoshi Funakoshi*, Atsushi Okamoto, and Kunihiro Sato. “Long-term reading experiment on a photorefractive holographic memory with the hologram sustainment technique by optical feedback”. In: *Journal of Modern Optics* 52.11 (2005), pp. 1511–1527.

[58] Nurul Athirah Abd Razak, Noriza Ahmad Zabidi, and Ahmad Nazrul Rosli. “A first principle study of band structure of tetragonal barium titanate”. In: *AIP Conference Proceedings*. Vol. 1875. 1. AIP Publishing LLC. 2017, p. 020017.

[59] M Yousaf et al. “Preparations, optical, structural, conductive and magnetic evaluations of RE’s (Pr, Y, Gd, Ho, Yb) doped spinel nanoferrites”. In: *Ceramics International* 46.4 (2020), pp. 4280–4288.

[60] Min Yang et al. “Ultrasonic-induced enhancement in interfacial exchange coupling of composite ferrites via chemical co-precipitation”. In: *Journal of Alloys and Compounds* 820 (2020), p. 153429.

[61] Hiroyasu Yamahara, Munetoshi Seki, and Hitoshi Tabata. “High temperature spin cluster glass behavior in Co-and Si-substituted garnet ferrite thin films”. In: *Journal of Magnetism and Magnetic Materials* 501 (2020), p. 166437.

[62] Youness Alvandi-Tabrizi and Justin Schwartz. “Micromagnetic analysis of crystallographic texturing and substrate-induced strain effects in NiFe2O4 and CoFe2O4 thin films”. In: *Acta Materialia* 149 (2018), pp. 193–205.

[63] Chao Zhou et al. “The phase diagram and exotic magnetostrictive behaviors in spinel oxide Co (Fe1- xAlx) 2O4 system”. In: *Materials* 12.10 (2019), p. 1685.

[64] Justin D Starr and Jennifer S Andrew. “A route to synthesize multifunctional tri-phasic nanofibers”. In: *Journal of Materials Chemistry C* 1.14 (2013), pp. 2529–2533.

[65] Justin D Starr and Jennifer S Andrew. “Janus-type bi-phasic functional nanofibers”. In: *Chemical Communications* 49.39 (2013), pp. 4151–4153.

[66] Jennifer S Andrew, Justin D Starr, and Maeve AK Budi. “Prospects for nanostructured multiferroic composite materials”. In: *Scripta Materialia* 74 (2014), pp. 38–43.

[67] Seeram Ramakrishna. *An introduction to electrospinning and nanofibers*. World scientific, 2005.

[68] Wolfgang Sigmund et al. “Processing and structure relationships in electrospinning of ceramic fiber systems”. In: *Journal of the American Ceramic Society* 89.2 (2006), pp. 395–407.

[69] eg PA Franken et al. “Generation of optical harmonics”. In: *Physical Review Letters* 7.4 (1961), p. 118.

[70] Chung L Tang, R Boyd, and I McMichael. “Nonlinear optics”. In: *Optics & Photonics News* 7.6 (1996), p. 52.

[71] DN Nikogosyan. “Beta barium borate (BBO)”. In: *Applied Physics A* 52.6 (1991), pp. 359–368.

[72] John G Haub, MJ Johnson, and Brian J Orr. "Spectroscopic and nonlinear-optical applications of a tunable β-barium borate optical parametric oscillator". In: *JOSA B* 10.9 (1993), pp. 1765–1777.

[73] W Joosen et al. "Parametric generation in β-barium borate of intense femtosecond pulses near 800 nm". In: *JOSA B* 8.10 (1991), pp. 2087–2093.

[74] PN Solovev et al. "Second harmonic generation in thin permalloy film". In: *Journal of Physics D: Applied Physics* 54.42 (2021), p. 425002.

[75] Cory Dolbashian et al. "Magnetic properties of aligned multiferroic Janus nanofiber agglomerates measured with the scattered magneto-optical Kerr effect". In: *Journal of Physics D: Applied Physics* 53.19 (2020), p. 195002.

[76] IC Nlebedim and David C Jiles. "Dependence of the magnetostrictive properties of cobalt ferrite on the initial powder particle size distribution". In: *Journal of Applied Physics* 115.17 (2014), 17A928.

[77] JC Maurya, SV Bhoraskar, and VL Mathe. "Effect of manganese substitution on magnetoimpedance and magnetostriction of cobalt ferrites". In: *Physica B: Condensed Matter* 436 (2014), pp. 220–226.

[78] Zong-Yang Shen and Jing-Feng Li. "Enhancement of piezoelectric constant d33 in BaTiO3 ceramics due to nano-domain structure". In: *Journal of the Ceramic Society of Japan* 118.1382 (2010), pp. 940–943.

[79] Xiaohu Gao et al. "In vivo cancer targeting and imaging with semiconductor quantum dots". In: *Nature biotechnology* 22.8 (2004), pp. 969–976.

[80] X Michalet et al. "Quantum dots for live cells, in vivo imaging, and diagnostics". In: *science* 307.5709 (2005), pp. 538–544.

[81] Alexey Evgen'evich Zhukov and AR Kovsh. "Quantum dot diode lasers for optical communication systems". In: *Quantum Electronics* 38.5 (2008), p. 409.

[82] Mee Rahn Kim and Dongling Ma. "Quantum-dot-based solar cells: recent advances, strategies, and challenges". In: *The journal of physical chemistry letters* 6.1 (2015), pp. 85–99.

[83] Katsuhiro Tomioka et al. "GaAs/AlGaAs core multishell nanowire-based light-emitting diodes on Si". In: *Nano letters* 10.5 (2010), pp. 1639–1644.

[84] Olivier Gazzano and Glenn S Solomon. "Toward optical quantum information processing with quantum dots coupled to microstructures". In: *JOSA B* 33.7 (2016), pp. C160–C175.

[85] JS Blakemore. "Semiconducting and other major properties of gallium arsenide". In: *Journal of Applied Physics* 53.10 (1982), R123–R181.

[86] VA Harutyunyan et al. "Interband Absorption and Photoluminescence in Nanospherical InP/InAs/InP Core/Shell/Shell Heterostructure". In: *Journal of Contemporary Physics (Armenian Academy of Sciences)* 54.1 (2019), pp. 33–45.

[87] TJ Ochalski et al. "Photoreflectance studies of InGaAs/GaAs/AlGaAs single quantum well laser structures". In: *Acta Physica Polonica-Series A General Physics* 94.3 (1998), pp. 463–467.

[88] Kitsakorn Locharoenrat. *Optical properties of solids: an introductory textbook*. CRC Press, 2016.

[89] R Ruppin. "Surface polaritons of a left-handed medium". In: *Physics Letters A* 277.1 (2000), pp. 61–64.

[90] Benjamin Reinhard et al. "Experimental and numerical studies of terahertz surface waves on a thin metamaterial film". In: *Optics letters* 35.9 (2010), pp. 1320–1322.

[91] Zhijun Sun et al. "Artificial TE-mode surface waves at metal surfaces mimicking surface plasmons". In: *Optics express* 22.4 (2014), pp. 4714–4722.

[92] Richard A Shelby, David R Smith, and Seldon Schultz. "Experimental verification of a negative index of refraction". In: *science* 292.5514 (2001), pp. 77–79.

[93] Yassin Chowdhury. *Plasmonic waveguides: design and comparative study*. 2011.

[94] Matt Seaton et al. "Localized All-Optical Control of Single Semiconductor Quantum Dots through Plasmon Polariton-Induced Screening". In: *Advanced Optical Materials* 6.15 (2018), p. 1800345.

[95] Mads Lykke Andersen et al. "Strongly modified plasmon–matter interaction with mesoscopic quantum emitters". In: *Nature Physics* 7.3 (2011), pp. 215–218.

[96] M Naveed-Ul-Haq et al. "A new (Ba, Ca)(Ti, Zr) O 3 based multiferroic composite with large magnetoelectric effect". In: *Scientific reports* 6.1 (2016), pp. 1–10.

[97] KP Jayachandran, JM Guedes, and HC Rodrigues. "Solutions for maximum coupling in multiferroic magnetoelectric composites by material design". In: *Scientific reports* 8.1 (2018), pp. 1–9.

[98] Juha Tommila et al. “Size-dependent properties of single InAs quantum dots grown in nanoimprint lithography patterned GaAs pits”. In: *Nanotechnology* 24.23 (2013), p. 235204.

[99] Koichi Okamoto, Saurabh Vyawahare, and Axel Scherer. “Surface-plasmon enhanced bright emission from CdSe quantum-dot nanocrystals”. In: *JOSA B* 23.8 (2006), pp. 1674–1678.

[100] Kenji Tanaka et al. “Multifold enhancement of quantum dot luminescence in plasmonic metamaterials”. In: *Physical review letters* 105.22 (2010), p. 227403.

Appendix A

Fabrication procedure using NanoFrazor

1) Sample preparation/dicing:

The first step in the pre-fabrication process is dicing the sample into smaller pieces ($\sim 4 \times 3$ mm), so it would fit in a chip carrier. To do this, we need two glass microscope slides that are cleaned with acetone. Since acetone tends to leave a residue behind, the slides are rinsed with isopropyl alcohol (IPA) and then blow-dried with compressed nitrogen (N2) gas. Note that in all steps that rinsing and blow-drying are needed, Methanol can be substituted for IPA, and compressed air can be substituted for N2 gas.

The selected area that needs to be cut is marked using a diamond scribing pen. The pen should be sharp and clean in order to minimize the debris the dicing process generates. Afterward, N2 gas is used to remove any large-particle dust in order to avoid scratching the top surface of the sample. Next, the sample is "sandwiched" between the two cleaned slides. The area that needs to be cut should extend beyond the slides. Then, a slight tap is sufficient to break the sample along the marked line created in the first step. When the sample is cut into the desired size, the underside of the sample is carefully marked with the scribing pen. It is important not to make a deep mark, so it does not reach the section of the sample with QDs. Because both sides of our particular sample look alike, this step can be crucial in the following fabrication steps to recognize the top surface. Then, the sample is blow-dried with N2 gas again.

2) Sample surface cleaning:

In order to obtain the best results in the fabrication process, it is critical to start with a clean sample, and free of dust particles and impurities. Here, the surface cleaning is accomplished in three steps. In the first step, the sample is sonicated in acetone for 8 - 12 minutes to clean off dust and macroscopic debris from the top surface. The sonication time can be longer or shorter depending upon the sample condition. Afterward, the sample is rinsed with IPA, followed by blow-drying with N2. Then, the sample is inspected under a microscope to ensure that there is no visible residue or dirt on the top surface. In the second cleaning step, the sample is dipped into a 10 % mixture of hydrogen chloride (HCl) and distilled water for 3 - 5 seconds to remove any residue and oxide from the sample surface. This step enhances the adhesion of the metal films to the surface in the deposition process. Heavy rinse with distilled water is required after this cleaning step, followed by another drying with N2. In the last cleaning step, the sample is placed into an oxygen plasma (Glow Plasma System) chamber to clean off any organic residue. The recommended time and pressure for our particular sample are 45 seconds and 1 Torr, respectively. The cleaned sample is then pre-baked on a hot plate at 110 °C for 5 minutes.

3) Resist coating:

When all cleaning steps are done, the sample is coated with one layer of a lift-off resist and one layer of a thermal resist. These two resists are spread uniformly on the surface of the sample using a spin-coating system which is helpful to reproduce the coating thickness. The relationship between the achieved film thickness and the angular velocity is given as the spin curve and is available online at the manufacturer's website.

Because our sample is too small to fully cover the O-ring of the spin-coating system, it should be first mounted on a bigger substrate. Any proper technique and material can be used in this step. Here, we used poly-methyl-methacrylate (PMMA)

with a molecular weight of 950K or 495K to adhere the sample onto a silicon substrate. First, a thick layer of PMMA is spread over the substrate and spun at a low velocity, such as 1000 rpm. Then, the sample is immediately placed over PMMA before it dries. Baking at 110 °C for 5 minutes is sufficient to ensure adhesion of the PMMA layer. It is important to place the sample at the center of the substrate, so the resists applied in the next step will be spread evenly on the surface. The sample is then cooled to room temperature before proceeding to the next step.

Afterward, the sample is entirely covered with enough PMGI SF3 using a new and clean glass pipette. It is important to apply the resist on the surface before start spinning the sample to achieve a uniform layer. The sample is spun at 6000 rpm for 60 seconds. This gives us a thickness of $\sim$ 65 - 70 nm. A sufficient acceleration rate should also be used to avoid thickening at the edges. Then, the sample is baked at 200 °C for 60 seconds on a hot plate.

If this resist does not adhere well to the sample surface, a monolayer of Hexamethyldisilazane (HMDS) can be applied first to enhance the adhesion of the resist to the sample. HMDS bonds to both the surface and the resist, so the wet etch solution would not remove the PMGI SF3 layer. To do this, HMDS is spun at 6000 rpm for 60 seconds.

Next, the sample is coated with a thermal resist, a 3 w% PPA (Polyphthalaldehyde) solution using a new and clean glass pipette. To make this solution, 90 mg of the PPA powder is dissolved in anisole to have 3000 mg of the PPA solution. Since the PPA solution is stored in a refrigerator, it is important to ensure that it is warmed to room temperature before proceeding. The sample is spun at 5000 rpm for 60 seconds. This gives us a $\sim$ 30 - 35 nm thickness. It is then baked at 110 °C for 2 minutes. Afterward, the sample is inspected under a microscope again to ensure the sample surface is smooth and even.

4) Writing pattern into the thermal resist:

The sample is now ready to be patterned using NanoFrazor. The desired pattern is first designed using either KLayout or GIMP. Figure C.1 shows an example of a pattern layout. Then, the NanoFrazor is used to direct-write the pattern into PPA. This is done by evaporating PPA, which is a thermally sensitive resist, using a CW laser source. For this particular pattern, the laser power and the pixel time are set at 150 mW and 70 μs, respectively. One of the advantages of using NanoFrazor is that there is no need to use a resist developer, and therefore we can proceed to the etching step.

5) Wet chemical etching process:

In order to have the silver structures closer to the QDs, the written patterns are first chemically etched into the underlying PMGI resist. To do this, the sample is immersed in a solution of TMAH (Tetramethylammonium hydroxide) (0.261 mol/l) in water for 70 seconds. To make this solution, 65 ml of AZ 726 MIF developer is diluted with 35 ml of distilled water. This gives us a 2.38 % solution with an etch rate of 1 nm/s. Stirring is not required in this step. The sample is then rinsed with distilled water and blow-dried thoroughly with N2 gas.

In the second step of the etching process, the capping layer of the sample is etched down. To do this, a weak acid solution is made by mixing 5 ml of phosphoric acid (H3PO4) with 20 ml of hydrogen peroxide (H2O2) and 250 ml of distilled water (H3PO4 : H2O2 : H2O = 1 : 4 : 50). To get the best results, a glass rod or a pipette is used to circulate the solution over the sample. Afterward, the sample is rinsed thoroughly with distilled water and blow-dried with N2. The exact etch rate of this solution is examined on a test sample using atomic force microscope (AFM). Here, an etched depth of $\sim$ 110 nm is achieved at an etch rate of $\sim$ 2.7 nm/s. In general, the etch rate can be affected by various factors such as temperature and humidity.

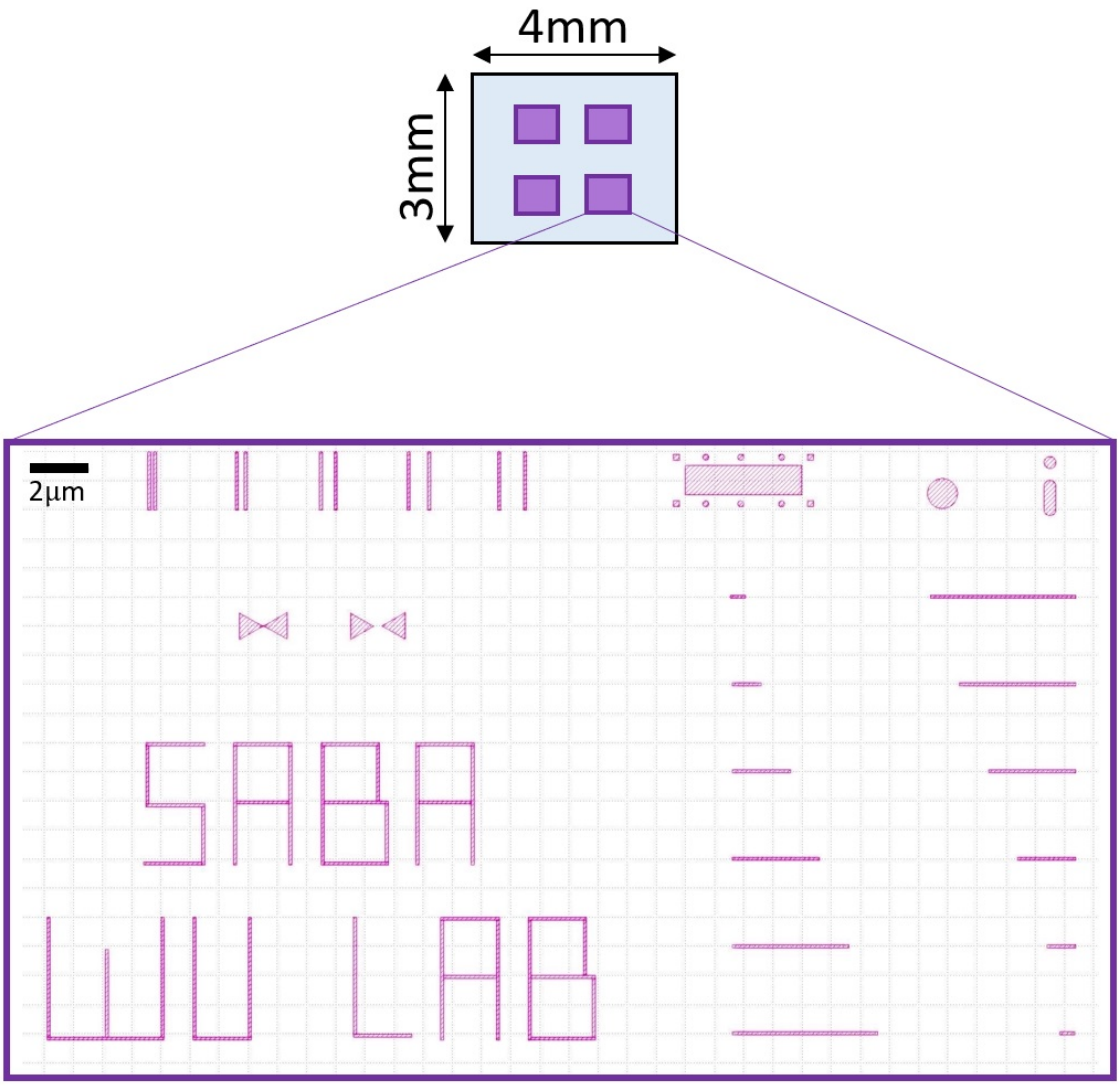

Figure A.1 An example of a pattern layout designed in KLayout to write into a 3 × 4 mm QD sample using NanoFrazor.

In addition, because the solution is stored in a refrigerator, it should be warmed to room temperature before using it. Moreover, using a fresh batch of solution can significantly affect the etch rate and the quality of the etched patterns.

6) Thin film deposition:

After inspecting the etched patterns under a microscope, it is time to complete the plasmonic structures of our device. A thickness of 60 nm of 99.99 % silver is uniformly deposited onto the sample at a rate of 1.5 Å/s using an ultra-high vacuum electron beam evaporator (AJA International, Inc). Using tape to cover the sample edges can make the lift-off process easier in the next step.

Following the deposition step, the sample is immersed in dimethyl sulfoxide (DMSO) in order to dissolve the unexposed resist sections and leave only the Ag slabs in the etched areas. Although the duration of this step is varied depending upon various factors, it is important to ensure that all resists are thoroughly removed. Then, a 5 nm layer of Cr is deposited on the sample surface at a rate of 2 Å/s in order to prevent oxidation of the silver and complete the Schottky diode structure. In addition, this semi-transparent layer allows us to study the sample optically.

7) Sample wire bonding:

In order to be able to apply an external bias across the sample, the top and bottom surfaces are connected to electrodes. This step should be done before affixing the sample to the chip carrier. Here, wire bonding is used to electrically connect the top surface to one of the terminals of the chip carrier. To do this, silver paste dissolved in toluene is used to attach a thin gold wire on the top of the Cr layer. In order to avoid shorting out the diode, it is crucial to make sure that the silver paste does not touch the silver slabs in the etched grooves. Afterward, the ohmic contact is done by melting Indium across the backside of the sample using a heated soldering iron. Next, silver paste is used to attach the sample to the chip carrier. Again, it is important not to use too much silver paste here. The paste should be dried entirely

before proceeding to the next step. Depending upon the sample condition, 15 - 30 minutes would be enough to ensure the adhesion of the silver paste. Afterward, both electrodes are tested using a standard multimeter.

Appendix B

Fabrication procedure using E-beam lithography

1) E-beam resist application:

Two different resists are used here: poly-methyl-methacrylate (PMMA) with a molecular weight of 950K and ZEP 520. Both of these resists are positive. In addition, a spin-coating system is used to coat the sample with the desired resist.

The sample is spun at 6000 rpm for 60 seconds. This gives us a resist thickness of $\sim$ 300 nm. Next, the sample is soft-baked on a hotplate at 170° C for 120 seconds. Then, it is cooled to room temperature. This step is repeated for three layers to achieve $\sim$ 900 nm thickness.

2) EBL (Jeol JSM-840A):

The top surface of the sample is grounded using conductive tape. This procedure is done with 30 keV electrons at a working distance of 8 mm. In order to achieve the maximum resolution, the lowest possible current (3 pA) is used.

3) Resist development:

The exposed sample is placed into the suggested developer, methyl isobutyl ketone (MIBK) : IPA = 1 : 3, for 30 seconds. Stirring with a glass rod is required here. The sample is then rinsed several times with IPA and blow-dried with N2.

4) Wet chemical etching:

Using the wet etching method (H3PO4:H2O2:H2O = 1:4:495), $\sim$ 100 nm of the GaAs capping layer is etched. This step is performed for 200 seconds with an etch

rate of 0.5 nm/s. Stirring with a glass rod is also required here. The sample is then rinsed several times with distilled water and blow-dried with N2.

5) Pattern inspection:

The pattern is inspected under a microscope. Next, AFM is used to determine the dimensions of the etched grooves.

6) Thin film deposition:

Here, 50 nm of gold is deposited uniformly on the sample.

7) Resist lift-off:

The sample is immersed in acetone in order to leave only the silver slabs in the etched areas. Stirring is not required by might help. Sonication can be performed if the resist is not removed properly. If the gold film is removed from the etched areas, a very thin layer of titanium ($\sim$ 2 nm) can be deposited under the gold film. This thin layer of titanium allows better adhesion of the gold film to the sample surface.

Appendix C

Fabrication procedure using photolithography

1) Photoresist application:

A spin-coating system is used to coat the sample with the photoresist S-1811 Sigma-Aldrich. The sample is spun at 6000 rpm for 60 seconds. This gives us a resist thickness of around 900 nm. Next, the sample is soft-baked on a hotplate at 115 °C for 60 seconds. Then, it is cooled to room temperature.

This photoresist is stored in a refrigerator. Therefore, it should be warmed to room temperature before opening.

2) Photoresist exposure:

The desired pattern is aligned properly on the sample surface. A yellow filter is used to focus the light onto the pattern. The sample is exposed to a light source with ultraviolet emission for 15 seconds (light intensity = 10 mW/cm^2). Only the areas that are not covered by the mask undergo a chemical reaction. The exposure time is varied depending upon the pattern size. Post soft-bake is not required using this photoresist.

3) Photoresist development:

The exposed sample is placed into the suggested developer, MF321, for 50 seconds. Stirring with a glass rod is required. The sample is then rinsed several times with distilled water and blow-dried with N2.

4) Hard-bake:

The sample is hard-baked on a hot plate at 125 °C for 5 minutes to harden to photoresist. The sample is then cooled to room temperature.

5) Pattern inspection:

The pattern is inspected under a microscope using a long-pass filter. If the exposed regions are completely clean free of the resist, the process is successfully completed. If not, repeat step 3 and vary the development time.

6) Follow steps 4-7 from Appendix B.